

Engineered upconversion nanoparticles for breast cancer theranostics

*Shijing Wang<sup>1,2#</sup>, Lei Zhang<sup>1#</sup>, Minghao Wang<sup>3#</sup>, Xiumei Yin<sup>2</sup>, Xinyao Dong<sup>2,4</sup>, Xingyu Wu<sup>2</sup>, Weijie Li<sup>2</sup>, Wen Xu<sup>2\*</sup>, Xiaoyun Mao<sup>1\*</sup>*

<sup>1</sup>Department of Breast Surgery, The First Affiliated Hospital of China Medical University, Shenyang, Liaoning Province, 110000, China

<sup>2</sup>Key Laboratory of New Energy and Rare Earth Resource Utilization of State Ethnic Affairs Commission, School of Physics and Materials Engineering, Dalian Minzu University, Dalian, Liaoning Province, 116600, China

<sup>3</sup>Department of Neurosurgery, The First Affiliated Hospital of China Medical University, Shenyang, Liaoning Province, 110000, China

<sup>4</sup>Dalian Maritime University, Dalian, Liaoning Province, 116600, China

<sup>#</sup>*Shijing Wang, Lei Zhang and Minghao Wang* contributed equally to this manuscript.

<sup>\*</sup>Corresponding authors:

*Wen Xu*, E-mail: xuwen@dlmu.edu.cn.

*Xiaoyun Mao*, E-mail: xymao@cmu.edu.cn.

## Abstract

Breast cancer (BC) remains the most prevalent cancer among women and a leading cause of cancer-related mortality worldwide, posing a significant threat to public health. Rare earth (RE)-doped upconversion nanoparticles (UCNPs) have emerged as a promising nanopatform for BC management, owing to their exceptional photophysical properties and design flexibility. Unlike conventional fluorescent probes, engineered UCNPs absorb near-infrared (NIR) light, enabling deep tissue penetration while mitigating tissue damage and spontaneous fluorescence interference. Furthermore, through core-shell structure engineering and functionalization, multiple diagnostic and therapeutic modules can be integrated within a single NP, enabling theranostic applications for BC. This review comprehensively summarizes recent advances in engineered UCNPs for BC theranostics. It begins by introducing the luminescence mechanisms, controllable synthesis methods, and surface modification strategies of UCNPs. Next, it explores the fundamental biological effects of UCNPs, including biodistribution, metabolic pathways, and biotoxicity. Subsequently, we systematically review applications of engineered UCNPs in BC molecular imaging, biomarker detection, phototherapy, smart drug/gene delivery, and immunotherapy. Finally, current challenges and clinical translation prospects of UCNPs are discussed.

**Keywords:** upconversion nanoparticles, breast cancer, theranostics, molecular imaging, biomarker detection, phototherapy, delivery, immunotherapy

**Abbreviations:** BC: breast cancer; RE: rare earth; UCNPs: upconversion nanoparticles; NIR: near-infrared; TNBC: triple-negative breast cancer; ER: estrogen receptor; PR: progesterone receptor; HER2: human epidermal growth factor receptor 2; UCL: upconversion luminescence; SPR: surface plasmon resonance; NPs: nanoparticles; PEG: polyethylene glycol; PAA: polyacrylic acid; PEI: polyethylenimine; FDA: Food and Drug Administration; mSiO<sub>2</sub>: mesoporous silica; EDC: 1-ethyl-3-(3-dimethylaminopropyl)carbodiimide; NHS: N-hydroxysuccinimide;

FA: folic acid; TME: tumor microenvironment; ROS: reactive oxygen species; EPR: enhanced permeability and retention; FR: folate receptor; MRI: magnetic resonance imaging; CT: computed tomography; PET: positron emission tomography; CA: contrast agent; IHC: immunohistochemistry; WB: western blotting; ELISA: enzyme-linked immunosorbent assay; FRET: Förster resonance energy transfer; VEGF: vascular endothelial growth factor; LOD: limit of detection; CA15-3: cancer antigen 15-3; CA125: cancer antigen 125; CEA: carcinoembryonic antigen; PDA: polydopamine; AuNPs: gold nanoparticles; mRNA: messenger RNA; ctDNA: circulating tumor DNA; PDT: photodynamic therapy; PS: photosensitizers; PTT: photothermal therapy; PTA: photothermal agents;  $^1\text{O}_2$ : singlet oxygen; RB: rose bengal; DOX: doxorubicin; siRNA: short interfering RNA; GSH: glutathione; DC: dendritic cell; ICD: immunogenic cell death; CTLA-4: cytotoxic T-lymphocyte-associated protein 4; GMP: good manufacturing practice; SARs: structure-activity relationships.

## 1. Introduction

BC comprises a diverse spectrum of malignancies originating in the mammary glands and remains the most prevalent cancer among women. According to global cancer burden data, over 2.3 million new BC cases were diagnosed worldwide in 2022, causing approximately 670,000 deaths (Figure 1A) [1]. Projections indicate that by 2050, global new BC cases will reach 3.2 million, with 1.1 million deaths, representing increases of 38% and 68%, respectively, from 2022 levels [2]. The estimated lifetime risk of developing BC is 8–12%, while modifiable risk factors remain limited [3,4]. Characterized by high heterogeneity, BC is classified into luminal A, normal-like, luminal B, HER2-enriched, and triple-negative breast cancer (TNBC) subtypes based on hormone receptor expression (estrogen receptor [ER], progesterone receptor [PR]), the proliferation marker Ki-67, and human epidermal growth factor receptor 2 (HER2) status. Each subtype exhibits distinct epidemiological characteristics, treatment responses, and prognostic outcomes (Figure 1B).

Current BC diagnosis relies on physical examination, imaging, and histopathology (Figure 1C). Physical examination includes thorough evaluation of the breast, lymph nodes, and potential distant metastases. However, early-stage BC patients often lack specific symptoms or signs, complicating diagnosis. Imaging modalities such as mammography and ultrasonography play crucial roles in the diagnostic workflow. Mammography clearly visualizes breast masses and calcifications; owing to its affordability and accessibility, it is considered the optimal screening modality when combined with ultrasonography [5]. Nevertheless, mammography involves ionizing radiation exposure, while ultrasonography exhibits high operator dependence. Emerging technologies like AI-assisted analysis and high-throughput molecular staining demonstrate transformative potential, though technical standardization and clinical validation remain significant barriers to widespread adoption [6]. Furthermore, BC treatment has advanced dramatically over the past century, evolving from purely

surgical interventions to comprehensive, coordinated strategies integrating local and systemic therapies (Figure 1D). However, these approaches face limitations including surgical morbidity, non-selective chemotherapy toxicity, radiotherapy-related side effects, and restricted applicability of immunotherapy, endocrine therapy, and targeted agents. Therefore, integrating multidisciplinary approaches to develop flexible, tailored management strategies is essential for BC care.

In recent years, nanomaterials have demonstrated significant potential in biomedicine due to their unique size effects, high specific surface area, and tunable physicochemical properties [7]. Among these, RE-doped UCNPs exhibit exceptional optical characteristics. Unlike conventional luminescent materials that emit longer-wavelength light under shorter-wavelength excitation, UCNPs convert NIR excitation into shorter-wavelength emissions through photon upconversion [8]. This anti-Stokes process, termed upconversion luminescence (UCL), overcomes deep-tissue signal attenuation inherent to short-wavelength light while minimizing interference from endogenous fluorophores and reducing phototoxicity risks [9]. Specifically, light penetration in tissues is fundamentally limited by absorption and scattering, with longer wavelengths enabling greater depth penetration [10,11]. For instance, visible light exhibits shallow penetration in biological tissues, typically reaching only about 1 mm [12]. The optical penetration depth increases from 0.19 mm for 632.8 nm red light to 0.51 mm for 835 nm light in blood, and from 2.59 mm to 3.54 mm in mammary tissue [13]. Moreover, endogenous fluorophores predominantly absorb UV/visible light, reducing the signal-to-noise ratio, while short-wavelength excitation can trigger photochemical reactions that damage biomolecules [14]. Compared with other fluorescent probes, UCNPs show superiority in multiple dimensions (Table 1). Compared with fluorescent proteins, UCNPs do not require complex genetic encoding and have stronger resistance to photobleaching. In contrast to NIR organic dyes, UCNPs have distinct emission spectra and large anti-Stokes shifts, effectively avoiding overlap between excitation and detection signals. In complex physiological environments, the chemical inertness of UCNPs enables them to maintain long-term stability, whereas organic-inorganic hybrid fluorophores are vulnerable to the effects of pH and enzymes. Notably, the abundant ligand-binding sites on the surface of UCNPs provide favorable conditions for integrating multifunctional modules such as targeting molecules and therapeutic payloads (Figure 1E) [15]. The resulting nanocomposites have shown tremendous promise in fields including tumor therapy, small-animal in vivo imaging, and molecular detection.

As a superficial organ, the breast exhibits optical properties characterized by moderate light scattering, highly forward-directed scattering, and low NIR absorption, making it ideally suited for applications of UCNPs [16–19]. Meanwhile, as programmable nanoplatfroms, UCNPs enable precise intervention in different molecularly stratified BC through modular design, which is highly congruent with clinical requirements [20]. Recent advancements in engineered UCNPs have shown remarkable progress across multiple domains of BC management, including subtype-specific biomarker

detection, molecular phenotype-adapted multimodal imaging, personalized phototherapy, smart drug/gene delivery, and immunotherapy. In this context, a systematic review of literature on UCNP-based BC theranostics is particularly necessary. However, most existing reviews focus on oncology at large, which have the drawbacks of broad research scopes and vague disease characteristics. Specifically, most reviews treat all malignant tumors as a single pathological entity, ignoring tumor heterogeneity and especially lacking systematic analysis of BC. While such integrative research helps explore common principles, it hinders the development and clinical translation of nanomedicine platforms tailored for BC. In this review, we first introduce UCNPs, covering their optical properties, advanced synthesis methods, and diverse functionalization strategies. We then discuss the *in vivo* biodistribution, clearance pathways, and potential biosafety issues of UCNPs. Building on this, we provide a comprehensive review of the applications of engineered UCNPs in BC diagnosis and therapy. Finally, we critically evaluate current limitations and propose strategic directions for future research, aiming to bridge the gap between basic science and clinical practice.

## 2. Introduction of UCNPs

RE elements, comprising Sc, Y and the fifteen lanthanides, are renowned as the "vitamin" of modern industry due to their superior physicochemical properties. Doping RE ions into inorganic materials not only modulates the crystal phase, morphology, size, and electronic structure of materials, but also endows the doped materials with rich optical, electrical, magnetic, and catalytic properties. Notably, RE elements exhibit a systematic ionic radius contraction and share similar electronic configurations (Figure 2A) [21]. Except for  $\text{Sc}^{3+}$ ,  $\text{Y}^{3+}$ ,  $\text{La}^{3+}$ , and  $\text{Lu}^{3+}$ , the 4f electrons of other RE ions follow quantum mechanical principles, populating seven degenerate orbitals and generating intricate energy-level systems. These long-lived metastable states undergo fine splittings under spin-orbit coupling and crystal field effects, constituting the energy-level foundation necessary for UCL (Figure 2B) [22]. The concept of UCL was first proposed by Nobel laureate Nicolaas Bloembergen in 1959, who envisioned using the multi-level energy structure of RE ions for NIR light detection [23]. In 1966, Auzel, Ovsyankin, and Feofilov independently observed and interpreted this phenomenon in RE-doped bulk materials, marking the official commencement of research on upconversion luminescent materials [24,25].

In the following decades, upconversion luminescent materials were confined to bulk materials such as glasses and ceramics, suffering from issues including low energy conversion efficiency, high excitation power thresholds, and the difficulty in controlling complex multi-ion cooperative mechanisms [26]. The emergence of nanoscience and various nanomanufacturing technologies in the 1990s inspired researchers to miniaturize upconversion luminescent materials to the nanoscale. One of the earliest attempts was reported in 1999 by Zijlmans et al., who prepared 0.2–0.4  $\mu\text{m}$   $\text{Y}_2\text{O}_2\text{S}:\text{Yb},\text{Er}$  and  $\text{Y}_2\text{O}_2\text{S}:\text{Yb},\text{Tm}$  microparticles via superheating as upconversion luminescent biolabels for immunoassays [27]. Nevertheless, this approach was



constrained to producing particles with minimum sizes of several hundred nanometers, which hindered their broader utilization. It was not until the early 21st century that novel synthetic methodologies, such as co-precipitation and hydrothermal/solvothermal synthesis, emerged for preparing high-quality crystals with sizes below 100 nm, thereby driving significant advancements in this field [28]. These techniques have enabled the reproducible fabrication of monodisperse UCNPs with precisely tunable size, morphology, and crystallinity. Leveraging their unique nanoscale properties and structural tunability, these UCNPs offer not only tailored optical characteristics but also serve as versatile platforms for multifunctional design. Today, UCNPs have become a highly interdisciplinary research field at the intersection of materials science and biomedicine [29,30].

## 2.1. Mechanism

Typically, UCNPs consist of an inorganic matrix, activator, and sensitizer [31]. The matrix (e.g., phosphate, oxide, or fluoride) provides an optically inert framework with low phonon energy, thereby modulating crystal field splitting of RE ions and suppressing non-radiative decay [32]. Activator ions serve as luminescent centers, populating high-energy excited states through energy harvesting and subsequently emitting anti-Stokes radiation. Sensitizer ions, characterized by broad absorption cross-sections, efficiently harvest low-energy photons and transfer energy to activators via dipole-dipole interactions or exchange mechanisms. As illustrated in Figure 2C, the upconversion process initiates with photon absorption by sensitizers, followed by non-radiative energy migration to activators, which are excited to higher energy states for emitting high-energy photons. Specific mechanisms include excited state absorption, energy transfer upconversion, cooperative upconversion, cross-relaxation, photon avalanche, and energy migration upconversion.

### 2.1.1. Excited state absorption

Excited state absorption, proposed by Bloembergen in 1959, involves a single RE ion absorbing photons sequentially, transitioning stepwise from the ground state to higher energy levels via intermediate excited states, and then decaying to the ground state with emission of a higher-energy photon (Figure 2D [i]) [23]. This necessitates RE ions to possess energy levels arranged in a ladder-like fashion with near-even spacing, thus restricting this process to a limited number of ions (e.g.,  $\text{Er}^{3+}$ ,  $\text{Ho}^{3+}$ ,  $\text{Tm}^{3+}$ , and  $\text{Nd}^{3+}$ ). Additionally, efficiency is typically constrained by factors including short excited-state lifetimes, energy level configurations distinct from ground states, and complex multiphoton absorption mechanisms, all of which reduce absorption probabilities [33]. Recently, Dong et al. achieved a breakthrough by employing layered ternary RE sulfides as host matrices. By leveraging the high absorption cross-section of  $\text{Er}^{3+}$  during the  $^4\text{I}_{15/2} \rightarrow ^4\text{I}_{13/2}$  transition and optimizing the prolonged lifetime in the  $^4\text{I}_{9/2}$  state, they achieved enhanced excited state absorption upconversion in  $\text{NaYF}_4\text{:Er}$ , yielding a visible upconversion efficiency of 2.6% [34].

### 2.1.2. Energy transfer upconversion

Energy transfer upconversion is the most common upconversion mechanism in UCNPs, differing from excited state absorption by involving energy transfer between multiple ions (Figure 2D [ii]). This mechanism necessitates a close spatial proximity between sensitizers and activators to enable efficient energy transfer via dipole-dipole interactions, along with precise energy level alignment to minimize non-radiative losses. Additionally, sensitizers should exhibit a larger absorption cross-section than activators to maximize energy harvesting efficiency under low intensity excitation [35].  $\text{Yb}^{3+}$  is frequently employed as a sensitizer owing to its well-matched 980 nm absorption cross-section with commercial diode lasers.  $\text{NaYF}_4:\text{Yb},\text{Er}$  has served as a highly efficient 980 nm-to-visible upconversion phosphor since the 1970s [36].

#### 2.1.3. Cooperative upconversion

Cooperative upconversion involves interactions among at least three ions, categorized into cooperative sensitization and cooperative luminescence (Figure 2D [iii]). In cooperative sensitization, two sensitizer ions jointly transfer energy to a single activator ion, enabling its transition to a higher excited state for upconversion. Cooperative luminescence differs by eliminating intermediate states, instead coupling emission directly to paired ion interactions in which identical RE ions (e.g.,  $\text{Yb}^{3+}$ - $\text{Yb}^{3+}$  pairs) serve as both energy donors and acceptors [37]. The involvement of virtual pair-level transitions in these processes imposes inherent quantum mechanical constraints, leading to significantly lower efficiency than that of excited state absorption and energy transfer upconversion.

#### 2.1.4. Cross-relaxation

Cross-relaxation is an energy transfer process occurring between excited ions, either identical or distinct (Figure 2D [iv]). It is generally regarded as detrimental to upconversion efficiency and constitutes the primary cause of concentration quenching [38]. This process proceeds via two pathways dictated by energy level configurations. Energy migration entails resonant energy transfer between adjacent ions with equivalent energy levels, preserving the system's energy equilibrium. In contrast, cross-energy-level cross-relaxation induces energy redistribution between mismatched electronic states, leading to spectral alterations or non-radiative losses that manifest as self-quenching effects, particularly in heavily doped systems [39]. Nevertheless, cross-relaxation can be strategically harnessed to modulate emission profiles in specific contexts. For example, Chen et al. realized single-band red UCL of  $\text{Ho}^{3+}$  by incorporating  $\text{Ce}^{3+}$  into  $\text{Yb}^{3+}$ - $\text{Ho}^{3+}$ -codoped UCNPs, exploiting cross-relaxation between  $\text{Ce}^{3+}$  and  $\text{Ho}^{3+}$  [40].

#### 2.1.5. Photon avalanche

Photon avalanche, first conceptualized by Chivian et al. in 1979, is a process involving a cycle of excited state absorption and cross-relaxation (Figure 2D [v]) [41]. Initially, ground-state electrons are promoted to higher energy levels through excited state absorption. Subsequently, these excited electrons undergo cross-relaxation with neighboring sensitizer ions, causing activator ions to transition to an intermediate

energy level while sensitizers move to an excited state. This interaction establishes a positive feedback loop via energy back-transfer, resulting in exponential electron population at intermediate levels and intense emission even at low activator concentrations. However, this process demands high excitation power densities, confining its applicability to systems doped with  $\text{Pr}^{3+}$ ,  $\text{Tm}^{3+}$ , or  $\text{Nd}^{3+}$  ions [42,43]. Notably, photon avalanche exhibits exceptionally high optical nonlinearity, wherein luminescence intensity increases exponentially once the excitation intensity surpasses a critical threshold. This property facilitates applications in super-resolution imaging, where the ultrahigh nonlinearity circumvents the traditional diffraction limit, enabling single-molecule or single-ion detection.

#### 2.1.6. Energy migration upconversion

Energy migration upconversion refers to a luminescence mechanism where RE ions are classified into sensitizers, energy-storage mediators, migration ions, and activators based on their roles in the energy transfer cascade. Core-shell engineering spatially segregates RE ions into distinct layers, thereby minimizing non-radiative losses and enabling directional energy transfer. As illustrated in Figure 2D (vi), sensitizer ions absorb pump photons and funnel energy to activator ions via energy-storage and migration ions. Activator ions subsequently emit photons as their excited electrons relax from high-energy states to the ground state. This mechanism utilizes energy-storage and migration ions to enable efficient upconversion in ions lacking suitable intermediate energy levels or exhibiting ultrashort-lived metastable states, such as  $\text{Ce}^{3+}$ ,  $\text{Gd}^{3+}$ ,  $\text{Tb}^{3+}$ ,  $\text{Dy}^{3+}$ ,  $\text{Eu}^{3+}$ ,  $\text{Sm}^{3+}$ , and  $\text{Sm}^{2+}$  [44]. It enables high upconversion efficiency under low-power excitation, thereby promoting the applications of UCNPs.

#### 2.2. Optical tuning

In biomedical applications, achieving high-contrast imaging, multiplexed biosensing, and spatiotemporally controlled therapy requires precisely tunable luminescence intensity and color. However, UCNPs face challenges due to significant non-radiative surface quenching caused by their high surface-to-volume ratio, as well as the limitations of RE elements, such as narrow excitation spectra and fixed emission wavelengths. Initial studies focused on regulating size and dopant concentration to modulate emission intensity, but these approaches couldn't generate new emission peaks or broaden the excitation bandwidth [45–47]. Further advancements have been made by utilizing energy transfer between multiple dopants to enhance tuning, but uncontrolled cross-relaxation processes between different RE ions cause substantial quenching effects [48]. Emerging research now prioritizes structural engineering approaches, particularly core-shell structures, which demonstrate multidimensional regulatory capabilities surpassing conventional single-parameter optimization methods. Unlike morphology regulation or component optimization, these hierarchical nanostructures enable synergistic control over luminescence efficiency, spectral tunability, and functional integration through precise interfacial engineering.

### 2.2.1. Enhancement of emission

Core-shell structures can be categorized into epitaxial and nonepitaxial shell layers based on the growth process. Epitaxial shell layers, which include inert, active, and multiple shells, have a composition and structure similar to the matrix, providing a robust crystal field and preventing surface quenching. In contrast, nonepitaxial shell layers typically consist of materials like  $\text{SiO}_2$ , metal, and organic dyes (Figure 3A) [49]. The active core-inert shell structure involve a UCNP-containing core encapsulated by an inert matrix-material shell. This design isolates the core from the external environment and passivates surface defects, significantly enhancing UCL. Examples of such systems include  $\text{NaYF}_4@\text{NaYF}_4$ ,  $\text{SrF}_2@\text{SrF}_2$ , and  $\text{NaYF}_4@\text{CaF}_2$  [50,51]. Within a specific range, increasing the shell thickness reduces ion cross-relaxation, leading to enhanced luminescence intensity. For instance, coating an inert  $\text{NaYF}_4$  shell on an active  $\text{NaErF}_4$  core resulted in stronger emission as the shell thickness increased from 2 nm to 5.5 nm (Figure 3B) [52]. On the basis of the inert shell, an active shell can be fabricated by introducing sensitizer into the shell layer. The spatial separation between sensitizers in the core and shell mitigates concentration quenching, thereby enhancing the absorption efficiency of excitation light. For example, Fu et al. achieved a 1643-fold enhancement in visible light emission and a 33-fold enhancement in NIR emission by incorporating  $\text{Yb}^{3+}$  as an energy transfer mediator in the shell [53]. Moreover, in comparison with single layer shell structures, multilayer core-shell nanostructures exhibit enhanced flexibility and multifunctionality in terms of their structural and surface properties.

Nonepitaxial shells enhance UCL by reducing concentration quenching, utilizing dye sensitization, and exploiting local surface plasmon resonance (SPR). For example,  $\text{NaErF}_4@\text{SiO}_2$  core-shell structures exhibit significantly enhanced UCL compared to  $\text{NaErF}_4$  cores, despite minimal changes in morphology and structure [54]. Coupling UCNPs with organic dyes improves light-harvesting efficiency due to the low extinction coefficients and narrow absorption bands of RE ions. Building on this approach, energy cascade upconversion via dye sensitization involves organic dyes absorbing excitation light, transferring energy to shell ions, and then to core ions, thereby enhancing UCL (Figure 3C) [55]. Moreover, the resonance phenomenon enhances the local electric field around the metal shell, which to some extent enhances the absorption efficiency of the sensitizer and the radiative decay rate of the activator in UCNPs. However, UCL enhancement occurs only when an appropriate distance is maintained between UCNPs and the metal shell, necessitating an isolation layer with optimal thickness [56].

### 2.2.2. Color modulation of emissions

The UCL emission spectra of UCNPs exhibit remarkably broad emission bands, spanning from the UV to NIR spectral region (Figure 3D). However, the diversity of RE types and multiple energy levels within ions pose challenges for precise color control. The spatial confinement effect of core-shell structures provides a systematic solution to address this challenge. A prime example is the

NaGdF<sub>4</sub>:Yb,Tm@NaGdF<sub>4</sub>:Eu,Tb,Dy,Sm system, which precisely manipulates complex energy transfer pathways among RE dopants through controlled doping concentration adjustments (Figure 3E) [57]. In a subsequent study, Qin et al. engineered a multi-layer core-shell structured UCNPs by incorporating Tm<sup>3+</sup>, Ho<sup>3+</sup>, and Er<sup>3+</sup> ions into the NaYF<sub>4</sub> matrix, enabling single-NP-level tricolor UCL across visible to NIR spectral regions [58]. Recently, Chen et al. developed a sandwich-type core-shell nanostructure with Yb<sup>3+</sup> in the core, Tm<sup>3+</sup> in the intermediate shell, and Tb<sup>3+</sup> in the outer shell, significantly reducing background fluorescence interference from Tm<sup>3+</sup> (Figure 3F) [59]. Furthermore, shell-structured orthogonal upconversion for emission color adjustment has opened new avenues for various applications.

### 3. Synthesis methods of UCNPs

Significant advancements have been made in UCNP synthesis over the past two decades, enabling precise control over structural parameters such as crystallographic phase, size, and morphology. Diverse synthetic methods have been developed, including thermal decomposition, co-precipitation, hydrothermal/solvothermal synthesis, sol-gel processes, microwave-assisted synthesis, microemulsion techniques, and hybrid approaches. Among these, thermal decomposition, co-precipitation, and hydrothermal/solvothermal synthesis are the dominant strategies for fabricating high-quality nanocrystals by precisely regulating crystal growth kinetics. Furthermore, near-atomic-scale material engineering has enabled the design of core-shell architectures, enhancing functional capabilities through optimized interfacial energy transfer modulation.

#### 3.1. Synthesis of core

##### 3.1.1. Thermal decomposition

In thermal decomposition, metal-organic precursors are introduced into solvents under anhydrous and oxygen-free conditions, with decomposition occurring at elevated temperatures [60]. Reaction solvents are typically categorized into non-coordinating and coordinating types. Non-coordinating solvents provide a high-temperature environment for rapid NP nucleation and crystal transformation, while coordinating solvents adsorb onto the surfaces of particles to inhibit growth and agglomeration. In 2005, Yan et al. synthesized highly monodisperse LaF<sub>3</sub> NPs via thermally decomposing trifluoroacetate at 280 °C (Figure 4A) [61]. Subsequently, Chow et al. used oleylamine as both the reaction solvent and surface ligand to synthesize NaYF<sub>4</sub> NPs, enabling the phase transition from cubic to hexagonal structure (Figure 4B) [62]. Subsequent studies synthesized various fluoride crystals by adjusting the precursor concentration ratio, reaction temperature, reaction duration, and solvent type [63–65]. This method has also been applied to the synthesis of lanthanide oxides, oxyfluorides, and oxychlorides (Figure 4C) [66–68]. Thermally decomposed nanocrystals are high-quality, featuring pure crystal phases and uniform morphology. However, this method requires stringent synthesis conditions and incurs relatively high costs. Moreover, metal-organic precursors are prone to oxidation, potentially leading to the generation of toxic by-products.

### 3.1.2. Hydrothermal/solvothermal synthesis

Hydrothermal/solvothermal synthesis is a method to produce high-quality UCNPs at relatively low temperatures using water or organic solvents. Precursors typically include nitrates, chlorides, and oxides of RE ions. For  $\text{LnF}_3$  nanocrystal synthesis, fluoride compounds such as HF,  $\text{NH}_4\text{F}$ , or  $\text{NH}_4\text{HF}_2$  are often used, while NaF or KF is preferred for synthesizing  $\text{MLnF}_4$  nanocrystals. Common organic solvents, such as oleic acid, polyethylenediamine, and ethylenediaminetetraacetic acid, are used [69]. Based on this method, Li et al. utilized the "liquid-solid-solution" strategy to synthesize various high-quality fluoride matrices, such as  $\text{NaYF}_4$ ,  $\text{NaGdF}_4$ , and  $\text{YF}_3$  (Figure 4D-F) [70–73]. This method has also been successfully used to prepare lanthanide-doped oxide UCNPs with size-controllable and morphology-tunable features. Hydrothermal/solvothermal synthesis is an environmentally benign approach, but it is time-consuming and highly reliant on reaction vessels, thereby challenging real-time observation and monitoring of the reaction process.

### 3.1.3. Coprecipitation

Coprecipitation is a process where multiple metal ions precipitate and crystallize simultaneously in the presence of a precipitating agent. Veggel et al. pioneered this method via coprecipitation of trivalent RE ions and  $\text{F}^-$  in an ethanol-water solution at 75 °C [74]. However, the initial nanocrystals produced by this method had low luminescence intensity. To address this, researchers dissolved precursors at low temperatures and used heat treatment to transform amorphous seed crystals into well-crystallized nanocrystals. For example, Guo et al. synthesized  $\text{NaYF}_4$  NPs by mixing ethylene-diamine-tetraacetic acid with RE ions and rapidly adding the mixture to a NaF solution. Subsequent thermal treatment increased fluorescence intensity by 40 times compared to pre-annealing [75]. Currently, via post-heat treatment and surfactant addition, a wide range of NPs, such as  $\text{NaScF}_4$  and  $\text{KYb}_2\text{F}_7$ , can be synthesized (Figure 4G-H) [76,77]. This method is simple to operate, low-cost, and highly reproducible, but it requires calcination (post-annealing) of precipitates, which may induce nanocrystal aggregation and overgrowth.

### 3.2. Synthesis of core-shell

With advances in materials engineering, core-shell UCNPs exhibit greater tunability in morphology, size, composition, and surface properties. To date, various fabrication strategies have been employed to construct core-shell UCNPs. The seed-mediated heat-up method involves preparing core UCNPs first, which then serve as seeds for epitaxial shell growth. This method has successfully synthesized diverse core-shell nanostructures such as  $\text{EuF}_3@\text{GdF}_3$ ,  $\text{NaYbF}_4@\text{CaF}_2$ ,  $\text{NaGdF}_4@\text{NaGdF}_4$ ,  $\text{NaYF}_4@\text{NaYF}_4$ , and  $\text{LiLuF}_4@\text{LiLuF}_4$ , though it may lead to non-uniform shell thickness (Figure 4I) [78–82]. The successive layer-by-layer method is used for fabricating uniform multilayered structures with precise shell thickness control (Figure 4J) [83], as demonstrated by Li et al. who adjusted shell precursor concentrations to achieve shell thicknesses from 0.36 to 8 nm [84]. Diverse

morphologies can also be achieved through ion migration, as shown by Jin et al. who controlled the ratio of oleate anions to cations to form 3D morphologies such as dumbbells, flowers, and bamboo-like structures (Figure 4K-M) [65]. Ostwald ripening, which involves the dissolution of small particles and growth of larger ones, also leads to core-shell formation. Cation exchange, pioneered by Veggel et al. in 2009, involves exchanging RE ions on the UCNPs' surface with cations in the reaction solution to form a distinct shell, though it is unsuitable for multilayer structures [85]. Nonepitaxial growth refers to the deposition of shell materials (e.g., noble metals or SiO<sub>2</sub>) on UCNPs without crystallographic alignment with the core, resulting in an amorphous or polycrystalline shell structure (Figure 4N-P) [86–90]. This structural characteristic not only preserves the intrinsic optical properties of UCNPs but also offers a versatile platform for subsequent surface modifications.

#### **4. Surface Engineering**

The mainstream synthesis methods of UCNPs often use hydrophobic surface ligands, making them soluble in non-polar organic solvents but insoluble in aqueous media, thus restricting their biomedical applications. Surface modification is crucial for enabling UCNPs to disperse in physiological solutions, achievable through techniques such as ligand exchange, stripping surface ligand, silanization, layer-by-layer assembly, and amphiphilic polymer coating (Figure 5A). In these processes, hydrophobic UCNPs are synthesized and modified with hydrophilic functional groups, reducing aggregation in biological environments by altering composition and charge. Additionally, the functional groups provide reactive sites for conjugating with biomolecules, enabling advanced functionalities like active targeting and drug/gene delivery.

##### **4.1. Surface modification of UCNPs**

###### **4.1.1. Ligand exchange**

Ligand exchange improves the water dispersibility of UCNPs by replacing original hydrophobic ligands with functional hydrophilic ones. This process relies on the differing coordination capacities of organic ligands on the material surface, where stronger ligands displace weaker ones. Direct ligand replacement on the particle surface minimizes size changes in UCNPs. For effective exchange in oleic acid-coated UCNPs, multidentate or excess monodentate ligands are required, whereas oleylamine-coated UCNPs allow easier exchange due to weaker ligand interactions [91]. Common ligands include small molecules (e.g., citric acid, mercaptopropionic acid, phosphoethanolamine) and polymers (e.g., polyethylene glycol [PEG], polyacrylic acid [PAA], polyethylenimine [PEI]). For in vivo applications, bisphosphonate/tetraphosphonate-modified PEG is particularly advantageous, as its hydrophilicity, biocompatibility, and high binding affinity avoid biomolecule interference (e.g., DNA, proteins) [92].

###### **4.1.2. Stripping surface ligand**

Stripping surface ligand is a straightforward yet effective strategy for modifying

hydrophobic UCNPs. Under ultrasonic conditions, oleate ligands on UCNPs can be removed using  $\text{NOBF}_4$  or  $\text{HCl}$ .  $\text{NOBF}_4$  substitutes oleate ligands with inorganic  $\text{BF}_4^-$  anions, enabling UCNPs to disperse in solvents such as acetonitrile, DMSO, and DMF, but not in water [93]. Although  $\text{HCl}$  treatment protonates oleate, causing ligand detachment and leaving UCNPs with bare, positively charged surfaces, it may disrupt the crystal lattice and weaken luminescence [94]. The colloidal stability achieved via these two methods is easily disrupted, as the electrostatic balance of the system is sensitive to concentration changes or other ions. Therefore, further modification with hydrophilic molecules or electronegative functional groups (e.g., carboxyl, sulfonic acid, phosphonic acid) is often required, which enhances UCNP stability and luminescence intensity through coordination with RE ions.

#### 4.1.3. Silica coating

Silica exhibits several advantageous properties, including exceptional optical transparency, outstanding chemical stability, and excellent biocompatibility. These attributes have rendered it a Food and Drug Administration (FDA)-approved material for biomedical applications, positioning it as an ideal candidate for the surface modification of UCNPs [95]. As previously discussed, depositing  $\text{SiO}_2$  on UCNPs via nonepitaxial growth not only allows precise modulation of emission but also provides abundant functionalizable groups for further modification. The primary silica coating methods are sol-gel nanochemistry in reverse micelles for hydrophobic UCNPs and the modified Stöber method for hydrophilic UCNPs. For example, Veggel et al. used the modified Stöber method to synthesize  $\text{SiO}_2$ -coated UCNPs and subsequently aminated the silica surface for biological labeling [96]. A particularly advantageous variant of  $\text{SiO}_2$  is mesoporous silica ( $\text{mSiO}_2$ ), which features a high specific surface area and substantial pore volume. These properties enable efficient adsorption and afford high loading capacities for therapeutic agents [97]. Notably, silanization may increase particle size and polydispersity, and structural verification of ultrathin silica shells remains technically challenging.

#### 4.1.4. Other methods

Layer-by-layer assembly and amphiphilic polymer coating are additional surface modification methods for UCNPs. This strategy uses electrostatic interactions to sequentially adsorb oppositely charged ligands, enabling the preparation of coated colloids with diverse shapes, sizes, and compositions [98]. Amphiphilic polymer coating encapsulates hydrophobic UCNPs with molecules containing hydrophobic alkyl chains and hydrophilic groups, enhancing aqueous dispersion [99]. Various amphiphilic polymers have been employed for surface modification, including poly(maleic anhydride-alt-1-octadecene)-bis(hexamethylene)triamine, D- $\alpha$ -tocopheryl polyethylene glycol succinate, block copolymers like poly(ethylene glycol)-block-poly(caprolactone) and poly(ethylene glycol)-block-poly(lactic-co-glycolic acid), as well as non-immunogenic phospholipid membranes [100–102]. It is crucial to note that maintaining the colloidal stability of UCNPs in high-ionic-strength biological environments remains challenging,



necessitating comprehensive surface modification strategies.

#### 4.2. Bioconjugation

Historically, UCNP surface engineering focused primarily on enhancing aqueous dispersion and stability. For theranostic applications, however, bioconjugation with biomolecules is essential. This process is categorized into non-covalent and covalent bioconjugation based on interaction thermodynamics and conjugate stability. Non-covalent approaches, such as electrostatic adsorption,  $\pi$ - $\pi$  stacking, bioaffinity interactions, or physical entrapment, enable rapid functionalization. Yet relying on weak intermolecular forces (e.g., van der Waals, hydrogen bonding, ionic pairing), they risk dissociation in dynamic biological environments where pH fluctuations, competitive protein adsorption, or shear stress can destabilize complexes, causing premature payload release and off-target effects.

Covalent bioconjugation is a key functionalization strategy ensuring durable, site-specific bioactivity. This approach uses engineered surface groups to form strong covalent bonds with biomolecular functional groups, enabling ordered orientation and robust stability (Figure 5B). Specifically, during the hydrophilic phase transfer of UCNPs, introducing reactive groups (e.g., carboxyl, amino, maleimide) creates a versatile platform for biomolecular conjugation. Carboxyl-based conjugation systems typically employ 1-ethyl-3-(3-dimethylaminopropyl)carbodiimide (EDC)/N-hydroxysuccinimide (NHS) activation chemistry. When ligands like PAA or azelaic acid are anchored to UCNPs, their exposed carboxyl groups are activated by EDC/NHS to generate reactive ester intermediates. These intermediates efficiently couple with primary amine-containing biomolecules such as antibodies and amino-PEG derivatives, forming stable amide bonds [103,104]. Amine-functionalized UCNPs prepared with ligands such as PEI or aminoundecanoic acid exhibit dual functionality. The amino groups enable carbodiimide-mediated condensation with carboxylated biomolecules such as folic acid (FA) and aptamer, while the positive surface charge facilitates electrostatic binding to negatively charged nucleic acid [105,106]. Maleimide groups, as thiol-specific reactive sites, can be introduced via direct conjugation with maleimide-terminated polymers or secondary modification of amine-functionalized UCNPs with NHS-maleimide derivatives. These groups undergo rapid Michael addition with thiol-containing biomolecules such as cysteine residues or thiolated peptides, forming stable thioether bonds. This strategy is particularly advantageous for site-specific antibody conjugation and protein modifications that preserve structural integrity. Recent advances have integrated novel coupling methods to enhance UCNPs functionalization. For example, copper-free strain-promoted azide-alkyne cycloaddition overcomes the cytotoxicity limitations of traditional click chemistry. Azide-modified UCNPs rapidly conjugate dibenzocyclooctyne-tagged small molecules under physiological conditions, establishing biocompatible fluorescence imaging platforms [107].

#### 5. Biological Effects of UCNPs

Compared with bulk materials, nanomaterials exhibit a higher specific surface area and enhanced surface reactivity due to their nanoscale dimensions. These microscopic structural disparities give rise to distinct *in vivo* biological responses [108]. Specifically, nanomaterials demonstrate more complex pathways for entering the circulatory system, spatiotemporal tissue accumulation patterns, cellular uptake mechanisms, metabolic clearance kinetics, and biotoxicity profiles compared with conventional materials. The issue of biological effects becomes particularly pronounced in inorganic nanoplateforms such as UCNPs. These particles often accumulate and are poorly degradable *in vivo*, raising concerns about long-term risks. Such risks are not only associated with the materials themselves but also involve nano-biological interactions, including protein corona formation, immune recognition, and biotransformation processes, which remain largely uncharacterized. Therefore, a deep understanding of the biological effects of UCNPs is essential for promoting their safe and efficient translation into practical applications.

### 5.1. Biodistribution

The biodistribution of UCNPs involves a dynamic sequence of events beginning with translocation from administration sites into systemic circulation, followed by tissue accumulation and eventual cellular internalization. This process is influenced by both the administration route and the physicochemical properties of UCNPs. The former critically determines initial deposition and overcomes biological barriers during systemic dissemination, while the latter precisely regulates NP-cell interface interactions, determining endocytic pathway selection, lysosomal escape efficiency, and subcellular localization. Current analytical methods such as inductively coupled plasma optical emission spectroscopy and *in vivo* luminescence imaging have enabled preliminary biodistribution mapping.

#### 5.1.1. Tissue accumulation

Intravenous administration of UCNPs is the primary method for systemic delivery, allowing direct entry into the bloodstream (Figure 6A). NPs smaller than 500 nm are more suitable for intravenous injection due to their superior circulatory stability and tumor-targeting efficiency [109]. Once in the systemic circulation, UCNPs rapidly adsorb plasma proteins to form a dynamic protein corona, which masks surface ligands and redefines NP-receptor binding patterns [110–112]. The protein corona consists of opsonins and dysopsonins, affecting NP clearance. Opsonins activate pattern recognition receptors on phagocytes, triggering rapid clearance via the mononuclear phagocytic system, while dysopsonins may delay this process (Figure 6B-C) [113,114]. Strategies such as size optimization, charge modulation, and functional coatings can reduce immunogenicity and prolong blood residence time [115–117]. For example, ethylenediamine tetramethylenephosphonic acid-modified UCNPs remain in circulation for 60 minutes postinjection, doubling the retention time of citrate-coated counterparts [118]. However, repeated administration of polymer-coated NPs may induce adaptive immune responses, accelerating subsequent clearance [119]. The tissue accumulation of intravenously administered NPs exhibits

distinct organ-specific distribution patterns, which are governed by vascular physiological characteristics and biological filtration mechanisms. The heart and lungs, with high blood perfusion rates, exhibit rapid UCNPs accumulation [120]. The blood-brain barrier restricts most NPs from entering neural parenchyma, and muscle tissue penetration is limited by endothelial fenestration size [121,122]. The liver and spleen, with discontinuous sinusoidal capillary networks, demonstrate superior NP retention. Quantitative analysis revealed that approximately 87% of UCNPs accumulated in the liver following tail vein injection, highlighting off-target accumulation risks and potential hepatosplenic toxicity at high doses [123].

Intra-arterial delivery is a promising alternative to intravenous delivery for improving tumor therapy outcomes. Following intra-arterial administration, UCNPs enter systemic circulation rapidly, permeate capillary beds, and penetrate targets, increasing their likelihood of reaching the tumor site before hepatic or splenic retention. Preclinical studies in breast and hepatocellular carcinoma models demonstrate 3- to 5-fold increases in tumor accumulation with intra-arterial delivery compared to intravenous routes, coupled with reduced hepatic sequestration [124,125]. Unlike intravenous or intra-arterial delivery, subcutaneous administration enables NPs to diffuse through connective tissue and intercellular spaces between capillary or lymphatic endothelial cells, entering systemic circulation via membrane pores. This route enables UCNPs to reach local lymph nodes before entering systemic circulation, prolongs absorption, and reduces the need for repeated administration. Particles sized 10–100 nm and negatively charged are optimal due to weak interactions with blood/lymphatic components and reduced interstitial transport hindrance [126–128]. Beyond previously discussed delivery routes, novel approaches such as intraperitoneal injection, oral ingestion, inhalation, or targeted mucosal delivery demonstrate unique potential in ongoing investigations.

#### 5.1.2. Cellular internalization

The initial interaction between NPs and target cells, which involves cellular uptake, is of critical importance for achieving the desired effect. A few NPs can enter cells through simple diffusion or translocation, driven by their concentration and lipophilicity. However, most NPs are internalized via receptor-mediated endocytosis, an energy-dependent process which can be categorized into phagocytosis and pinocytosis (for smaller particles) (Figure 6D) [129]. This process initiates with ligand-receptor binding that induces membrane curvature and vesicle encapsulation. Post-internalization, vesicles undergo uncoating and fuse with early endosomes. These compartments employ adenosine triphosphate-driven proton pumps to acidify their lumen, facilitating maturation into late endosomes [130]. The late endosome fuses with lysosomes containing specific digestive enzymes, and the interaction between the nanocarrier and the digestive enzymes leads to the degradation of the loaded drugs or nucleic acids. Therefore, the ability of nanocarriers to escape lysosomal degradation is crucial for the delivery of their cargoes. The escape strategies primarily destabilize endosomal membranes by enhancing interactions

between the membrane and endosomal solvents. These include using endosomolytic enhancers for direct lysis, pore-forming agents to create transmembrane channels, high pH-buffering agents that mediate the proton sponge effect via protonation-induced swelling, photosensitizers for photochemical disruption, and fusogenic agents to promote membrane fusion by disturbing lipid arrangements [131]. Subsequently, the released NPs reach subcellular targets such as the cytoplasm, mitochondria, and nucleus through passive diffusion, membrane potential gradients, targeted signaling, or cytoskeletal transport. Notably, as mitochondrial dysfunction represents a key mechanism of nanomaterial toxicity, many mitochondria-targeting nanoplatforms have been developed to exert antitumor therapeutic effects.

The cellular dynamics of UCNPs adhere to universal principles and are primarily governed by their specific physicochemical parameters. Hydrodynamic diameter dictates endocytic route selection: smaller UCNPs prefer clathrin-mediated pathways, while larger aggregates may activate phagocytic mechanisms [132,133]. Surface charge emerges as a pivotal determinant of uptake efficiency, where positively charged UCNPs exhibit enhanced membrane affinity through electrostatic interactions with the anionic glycocalyx, facilitating rapid receptor clustering and accelerated vesicle formation compared to their neutral or negatively charged counterparts [134–136]. In addition, Li et al. reported that positively or neutrally charged UCNPs were internalized by most cell lines, whereas negatively charged UCNPs were primarily internalized by cancer cell [137]. The size- and charge-dependent cellular uptake can be further modulated by surface ligands. For example, PEG functionalization sterically hinders nonspecific interactions, whereas targeted ligands promote receptor-mediated trafficking, thereby enhancing the precision of cellular entry. Furthermore, concentration-dependent uptake kinetics demonstrate a linear correlation between UCNPs dosage and intracellular accumulation within biocompatible ranges, though supraoptimal concentrations risk lysosomal overload and subsequent organelle stress. Post-internalization fate studies emphasize the key role of lysosome escape efficiency, with UCNPs engineered with pH-responsive polymer coatings, hydroxychloroquine, or cell penetrating peptides enhancing cytosolic delivery by destabilizing the lysosome membrane [138–140].

## 5.2. Excretion

Pharmaceutical agents must meet strict clearance criteria, especially diagnostic agents, which require complete elimination within defined timeframes. This is because systemic clearance kinetics directly affect drug exposure duration, a key factor in determining toxicological risks. Similar to conventional pharmaceuticals, preclinical studies show that UCNPs are primarily cleared via hepatobiliary and renal pathways. Their excretion routes are primarily determined by hydrodynamic diameter due to the size-selective filtration mechanisms inherent in hepatic and renal tissues. Consequently, contemporary engineering strategies emphasize the development of biodegradable UCNPs, which facilitate size reduction from their original dimensions to clearance-compatible fragments.

### 5.2.1. Renal excretion

Renal excretion is the optimal route for NPs clearance, as it minimizes retention and cytotoxicity by avoiding intracellular catabolism. The fundamental structural and functional unit of the kidney is the renal unit, which is primarily composed of glomeruli and tubules. As illustrated in Figure 7A, the kidney filtration threshold for hard NPs is approximately 6 nm or smaller, taking into account the cumulative effect of the multilayer structures of the glomeruli [141–143]. Experimental evidence indicates that rigid NPs exceeding 100 nm are largely excluded from urinary excretion due to their inability to penetrate the endothelial fenestrae. NPs in the 6–100 nm range may traverse the endothelial layer but are subsequently retained by the glomerular basement membrane, while those between 1–6 nm demonstrate progressive filtration efficiency inversely proportional to size. Utilizing gamma counter detection, PEG-modified,  $^{153}\text{Sm}$ -labeled UCNPs (<10 nm), administered intravenously, were observed to accumulate in the bladder at a concentration of  $5.28 \pm 0.2\%$  ID  $\text{g}^{-1}$  from 0.5 to 6 hours post-injection [144]. In another study, Cao et al. found that within 48 hours, approximately  $6.32 \pm 0.51\%$  of the injected UCNPs were excreted in the urine [145]. Notably, NPs smaller than 1 nm may exhibit delayed clearance due to transient interactions with the glomerular glycocalyx. Soft NPs exhibit enhanced filtration capacity owing to structural deformability, elevating the renal filtration threshold to approximately 10 nm [146]. Moreover, aside from being filtered through the glomerulus, a small number of NPs are secreted and reabsorbed by the renal tubules [147].

### 5.2.2. Hepatobiliary excretion

In addition to renal excretion, the hepatobiliary system constitutes an alternative pathway for the elimination of NPs, albeit with a comparatively slower rate. The liver is supplied with blood by the hepatic artery and portal vein, which then circulate the blood internally before releasing it into the systemic circulation via the hepatic vein (Figure 7B). Metabolic waste and secreted substances from liver cells are transformed into bile, which is subsequently stored in the gallbladder and ultimately eliminated via the digestive tract. Key metabolic activities and substance exchanges occur within the hepatic sinusoids, a critical region where hepatocytes, Kupffer cells, and liver sinusoidal endothelial cells collaborate closely to maintain liver function [148]. During hepatic filtration, liver sinusoidal endothelial cells form the principal size-selective barrier through their characteristic 100–150 nm fenestrations. NPs larger than 100 nm typically cannot traverse these fenestrae to reach hepatocytes for hepatobiliary clearance, leading to prolonged retention by Kupffer cells and impaired fecal excretion [149]. Conversely, NPs with a size ranging between 6 and 100 nm are able to pass through the fenestrae of sinusoidal endothelial cells, interact with liver cells, and be excreted into the feces [148]. Many studies have demonstrated that UCNPs exceeding kidney filtration thresholds predominantly accumulate in hepatic and splenic tissues post-intravenous administration, followed by gradual hepatobiliary excretion. For instance, tracking of 11.5 nm PAA-coated UCNPs revealed delayed

intestinal signals emerging at 7 days post-injection, peaking at 90 days, and diminishing to near-background levels by day 115 [120]. Longitudinal metabolic investigations further identified extended biliary excretion cycles lasting up to 214 days for certain NPs, with excretion efficiency markedly lower than that of renal clearance pathways [150].

### 5.2.3. Biodegradable UCNPs

Considering that the elimination of NPs is highly size-dependent, biodegradable UCNPs have attracted increasing research attention. For example, Hong et al. fabricated biodegradable red-emitting  $K_3ZrF_7:Yb,Er$  NPs using an enhanced high-temperature coprecipitation approach. These NPs can be fully converted into approximately 5 nm residues within 10 hours when exposed to water, with a pH-dependent degradation rate that is faster in strong acids or alkalis and slower in weakly acidic biological solutions. In vivo experiments revealed that subcutaneously injected UCNPs were biodegraded within 120 minutes in both normal and 4T1 tumor-bearing mice, with a slower degradation rate in the tumor microenvironment (TME) than in normal physiological conditions, providing a time window for imaging. Additionally, these NPs showed low in vitro toxicity to human embryonic lung fibroblasts and no significant in vivo toxicity to muscles and major organs, with degradation products quickly excreted from rats [151]. Analogously, Lv et al. synthesized degradable peptide-modified UCNPs via a double emulsion method, which degrade into NPs smaller than 6 nm under weakly acidic conditions [152]. Furthermore, engineered surface shell modifications have emerged as a novel approach to regulate UCNPs degradation dynamics. For instance, Lin et al. constructed TME-responsive silica shells through Mn-O bond integration, where this stimuli-degradable architecture enables not only precision drug release but also enhances intratumoral penetration via progressive size diminution, substantially improving the spatial delivery efficiency of chemotherapeutic agents [153].

### 5.3. Biototoxicity

As early as 2003, Service conducted a comprehensive analysis of the biotoxicity of nanomaterials and their potential environmental impact in the journal *Science* [154]. This topic has subsequently attracted significant attention and in-depth discussion within the academic community. However, a 2018 study by Oliveira et al. revealed that only 18% of 1,811 publications focusing on biomedical applications of UCNPs addressed toxicity concerns, thereby underscoring a gap in risk assessment research [155]. Available studies indicate that the biotoxicity of UCNPs is governed by their physicochemical properties and exposure conditions. Most UCNPs exhibit acceptable biosafety profiles within specified concentration ranges but may induce dose-dependent organ-specific toxicity under high-dose or prolonged exposure conditions. Given the complexity of nanomaterials, related assessments should be conducted on a case-by-case basis.

#### 5.3.1. Multilevel biotoxicity manifestations of UCNPs

The biotoxicity of UCNPs can be systematically evaluated through a hierarchical research framework spanning multiple biological complexity levels. At the cellular level, UCNPs exhibit dose- and time-dependent cytotoxicity, primarily mediated by mitochondrial dysfunction and oxidative stress. Standardized cytotoxicity assays, including the methyl thiazolyl tetrazolium, 3-(4,5-dimethylthiazol-2-yl)-5-(3-carboxymethoxyphenyl)-2-(4-sulfophenyl)-2H-tetrazolium inner salt, and CCK-8 assays, demonstrate that engineered UCNPs maintain high cellular viability under acute exposure conditions. Metabolic impairment becomes statistically significant only beyond critical dose thresholds, as summarized in Table 2. *Caenorhabditis elegans* exhibit remarkable tolerance to UCNPs, showing no significant physiological or reproductive impairments following direct ingestion [156–158]. In contrast, zebrafish embryos exposed to high concentrations of uncoated UCNPs develop teratogenic effects, including delayed hatching, axial malformations, and gut dysbiosis, highlighting developmental stage-specific vulnerabilities [159–161]. In rodent studies, UCNPs administered via various administration routes have demonstrated acceptable safety profiles across diverse sizes, charge, and surface modifications (Table 3). Extended observation periods, ranging from minutes to months, and multiple dose levels reveal no significant toxic effects in behavioral parameters, body weight fluctuations, tissue morphology, or blood biochemical indices [162–166]. Transmission electron microscopy analysis of PEGylated UCNPs in mouse feces reveals no alterations in morphology, size, or distribution, suggesting that these NPs do not undergo significant *in vivo* transformation [167]. However, high-dose administration may induce target-organ toxicity, manifesting as hepatic steatosis, pulmonary inflammation, and renal tubular necrosis [168]. Regarding RE derivatives, chloride and nitrate salts exhibit reduced acute toxicity but pose risks of pneumonia and acute inflammatory responses with prolonged exposure [169,170]. Lanthanide chlorides enhance vascular permeability and influence blood components and enzymatic activities, though they have minimal impact on spermatogenesis. Notably, offspring of animals exposed to lanthanide citrates during lactation or pregnancy exhibit reduced body weight and excretory dysfunction, albeit without observable teratogenic effects [171].

### 5.3.2. Mechanism and influencing factors of biotoxicity

The biotoxicity of UCNPs arises from their interactions with cellular components, triggering pathological cascades through distinct molecular pathways. A principal cytotoxic mechanism involves reactive oxygen species (ROS) generation mediated by surface redox activity and lanthanide ion leaching [172,173]. Acute ROS mediate oxidative damage via DNA strand breaks, lipid peroxidation, and protein denaturation, while chronic overproduction triggers apoptosis/autophagy. Lysosomal dysfunction constitutes another pivotal toxicity pathway. For instance, UCNPs suppress autophagic lysosome reformation through dual disruption of phosphatidylinositol signaling and clathrin-mediated membrane recruitment, causing cellular dysfunction and inflammatory activation [174]. Furthermore, lysosomes provide critical microenvironmental conditions triggering degradation-dependent nanotoxicity. Under

lysosomal acidity, progressive UCNPs dissociation releases lanthanide ions that form needle-like crystalline precipitates with phosphates. These rigid nanostructures mechanically pierce lysosomal membranes and adjacent organelles, initiating cascading cellular damage. It should be noted that appropriate coatings, such as block copolymers, phosphonates with multiple phosphonic groups, silica, and phosphate, can mitigate the risks of chemical dissolution [155]. Furthermore, Gd<sup>3+</sup>-doping systems, commonly used for imaging contrast, are associated with phosphate-associated nephrogenic systemic fibrosis through renal ion retention [175].

The biotoxicity of UCNPs is primarily determined by three interconnected physicochemical factors: size dynamics, surface charge regulation, and ligand-mediated interfacial interactions. Size significantly influences cellular uptake efficiency and elimination kinetics. UCNPs with diameters above 55 nm exhibit minimal interference with cell proliferation but may induce prolonged inflammatory responses due to extended tissue retention [176]. Conversely, smaller UCNPs demonstrate enhanced cellular penetration and pronounced suppression of tumor cells [177]. Clearance studies reveal that 35 nm UCNPs are eliminated faster than 55 nm counterparts, despite higher cellular internalization rates [172]. Surface charge plays a critical role in nano-biological interactions. Positively charged UCNPs exhibit superior cellular internalization via clathrin-mediated endocytosis, driven by electrostatic attraction to anionic cell membranes [157]. However, such charge-driven uptake often correlates with membrane destabilization, as evidenced by the greater membrane disruption caused by cationic PEI-coated UCNPs compared to anionic variants [178]. Ligand chemistry significantly impacts biocompatibility by modulating surface charge, hydrodynamic stability, and targeting specificity. For instance, PEG-based coatings may induce sub-lethal cellular stress, which manifests as nuclear morphological alterations and nucleolar protein dysregulation, while PEI or polymaleic anhydride-olefin modifications can trigger calcium signaling disruption and cell death [179,180]. Chitosan reduces lipid emulsification and enhances platelet adhesion, while silica interacts with cells to potentially contribute to autoimmune diseases such as rheumatoid arthritis, lupus, or chronic renal conditions [181–183]. Additionally, ligand degradation byproducts, such as acidic PEG derivatives, may lead to acidosis and hypercalcemia [184].

## **6. Tumor targeting**

The accumulation of therapeutic agents in tumors represents a key to achieving theranostic objectives. However, the intrinsic physicochemical properties of pharmaceutical agents and biological barriers often significantly restrict their biodistribution [185]. Non-specific drug deposition in normal tissues may lead to severe side effects. In this context, nanocarrier-based targeting strategies have emerged as promising approaches to significantly improve tumor-specific drug accumulation, enhance pharmaceutical stability, and facilitate cellular uptake, thereby providing safer and more effective options. Based on different mechanisms, targeting strategies can be broadly categorized into passive targeting and active targeting.



### 6.1. Passive targeting

The tumor-targeting ability of nanomedicine has traditionally been ascribed to the enhanced permeability and retention (EPR) effect. First described by Yasuhiro Matsumura and Hiroshi Maeda in 1986, the EPR effect refers to the phenomenon whereby drugs accumulate in tumors solely through the utilization of tumor pathophysiological characteristics [186]. Specifically, in contrast to normal tissues, tumors exhibit more abundant blood vessels with distinct structural characteristics, which result from rapid cell proliferation and heightened demands for oxygen and nutrients. As shown in Figure 8, these abnormal blood vessels feature a discontinuous endothelial lining, which generates relatively large pores (0.1–3  $\mu\text{m}$ ) compared to those in normal vasculature [187]. Additionally, the lack of lymphatic vessels within tumors disrupts the normal drainage of lymphatic fluid. Consequently, liposomes, NPs, and macromolecular drugs smaller than the pore diameter can penetrate the vessel wall, infiltrate the tissue, and accumulate in tumors. The above process is termed passive targeting because it does not rely on active recognition motifs for targeting.

Although the EPR effect is a universal pathophysiological phenomenon observed in rodent, rabbit, canine, and human solid tumors, only a few anticancer drugs using passive targeting have been approved clinically in 30 years [188,189]. Notably, Stefan Wilhelm et al.'s 2016 meta-analysis revealed that NPs accumulation in the tumor constitutes only 0.7% of the injected dose [190]. In fact, tumor cells are embedded within a complex TME, which is composed of cancer-associated fibroblasts, immune cells, endothelial cells, extracellular matrix and other components. These components are highly variable, and each of them poses a potential barrier to the targeting [185]. For example, rapid tumor cell proliferation, hyperpermeable vasculature, and impaired lymphatic drainage collectively elevate interstitial pressure, creating hydrodynamic resistance that limits NPs penetration into high-pressure regions. Compounding this barrier, the fibrous extracellular matrix architecture physically obstructs particle diffusion while its abnormal proliferation compresses blood and lymphatic vessels. This compression establishes a self-reinforcing cycle of increasing interstitial hypertension that progressively restricts NPs transport across tumor [191,192]. Notably, physical and pharmacological strategies have emerged to improve passive tumor targeting. Physical approaches, such as hyperthermia, ultrasound, and microbubbles, can enhance the accumulation of nanomedicines in tumors [193]. Pharmacological approaches include increasing blood pressure via angiotensin, promoting vascular permeability using tumor necrosis factor and NO/CO-generating agents, and inhibiting cancer-associated fibroblasts with drugs like losartan [194–198]. Physical priming allows local control of treatment parameters but is only suitable for locally confined diseases. Pharmacological priming is more applicable to systemic diseases, yet has suboptimal control over spatial and temporal treatment parameters.

### 6.2. Active targeting

Active tumor targeting represents an approach that leverages specific molecular

recognition mechanisms to precisely deliver theranostic agents. The core principle involves leveraging overexpressed biomarkers on tumor cells or in the TME for localized nanomedicine enrichment via ligand-receptor interactions (Figure 8) [199]. This strategy dates back to 1980, when Lee D. Leserman et al. covalently conjugated liposomes with functional proteins (monoclonal antibodies and *Staphylococcus aureus* protein A) for specific cell binding [200]. Subsequent studies further expanded the repertoire of ligand-receptor pairs and diversified the nanocarriers. The surface chemistry programmability of UCNPs provides a versatile platform for active targeting through ligand bioconjugation, which can be implemented via non-covalent adsorption or covalent binding mechanisms.

The heterogeneity of BC necessitates tailored targeting strategies aligned with distinct receptors in luminal, HER2-positive, and TNBC subtypes. For HER2-enriched BC, full-length antibodies (e.g., trastuzumab) or peptides functionalize UCNPs, leveraging high-affinity binding to facilitate tumor accumulation [201,202]. However, conjugating macromolecular antibodies to comparably-sized NPs compromises pharmacokinetics and colloidal stability [203]. Alternative strategies using smaller antibody fragments, like single-chain variable fragments, offer improved pharmacokinetics and tumor penetration while retaining high affinity [204–206]. Similarly, designed ankyrin repeat proteins provide comparable affinity with greater compactness and cost-effectiveness for HER2-targeted UCNPs. For instance, UCNPs doped with radioactive  $^{90}\text{Y}$  and conjugated to the HER2-targeting toxin DARPIn-PE40 have demonstrated approximately 2200-fold enhanced synergistic cytotoxicity in HER2-positive BC cells [207]. In luminal subtypes with elevated neuropeptide  $\text{Y}_1$  receptor expression, Yu et al. developed UCNPs functionalized with  $\text{Y}_1$ -specific ligands for selective accumulation [168]. For target-lacking TNBC, small-molecule ligands exploit dysregulated metabolic pathways or membrane transporter activation to achieve targeted delivery. For instance, folate receptor (FR) overexpression in certain TNBC cases enables FA-conjugated UCNPs to efficiently accumulate in tumor cells through receptor-mediated endocytosis [208]. Moreover, peptide-functionalized nanoprobe enable active TNBC targeting through specific binding to oncogene product receptors [152]. In addition to the traditional single-level targeting approach, hierarchical targeting systems based on different ligands can enhance tumor specificity and therapeutic efficacy by binding to cell surface receptors and organelles [209]. Furthermore, considering the dynamic nature of the TME, static ligand design often fails to maintain sustained binding ability, prompting researchers to shift from single ligand optimization to systematic engineering of ligand-carrier-microenvironment interactions [210].

## 7. UCNPs for BC molecular imaging

Early diagnosis is critical for improving the prognosis of BC patients. Clinical data show that patients diagnosed early achieve five-year survival rates exceeding 99%, compared to less than 30% for advanced-stage disease [211]. This stark disparity underscores the urgent need to overcome diagnostic technology bottlenecks.

Conventional imaging primarily detects anatomical discrepancies but remains limited in identifying submillimeter early-stage lesions due to restricted spatial resolution. Furthermore, these techniques require acquisition times from minutes to hours and cannot provide real-time feedback on dynamic disease progression. In contrast, molecular imaging synergizes structural visualization with real-time mapping of molecular and cellular processes, offering high sensitivity, rapid response kinetics, and superior spatiotemporal resolution [212]. Among the emerging tools in this field, UCNPs have emerged as promising agents due to their unique optical properties and nanoscale dimensions. The following will respectively elaborate on the development of molecular imaging based on UCNPs in BC diagnosis (Table 4).

### 7.1. Fluorescence imaging

Fluorescence imaging is an optical imaging technique that detects fluorescence emitted by objects under illumination with light of specific wavelengths. Engineered UCNPs utilizing NIR excitation sources exhibit exceptional potential in fluorescence imaging due to their strong tissue penetration, minimal autofluorescence interference from biological tissues, and negligible phototoxicity.

In 2008, Chatterjee et al. first achieved in vivo animal imaging using PEI-coated NaYF<sub>4</sub>:Yb,Er NPs, demonstrating the superiority of UCNPs over quantum dots in deep-tissue imaging [213]. Subsequent engineering advancements, including optimized surface modifications and targeted ligand conjugation strategies, have further enhanced their utility for precise BC imaging applications. For instance, HER2 represents a pivotal biomarker and therapeutic target associated with tumor aggressiveness and poor prognosis, with overexpression observed in 10% to 30% of BC [214,215]. Grebenik et al. developed a HER2-specific imaging probe by conjugating UCNPs with mini-antibodies, achieving tenfold greater signal intensity in SK-BR-3 cells than control groups. This system demonstrated tumor visualization at 1.6 mm depth in simulated tissues with a 4.5 signal-to-noise ratio, while theoretical models predicted detection capabilities extending to 4 mm depths [206]. In two additional studies, Panikar et al. and García et al. respectively employed confocal microscopy to visualize anti-HER2 ligand-conjugated NaYF<sub>4</sub>:Yb,Er NPs, demonstrating specific intracellular red fluorescence in SK-BR-3 cells under 980 nm excitation [202,216].

The FR, a cell membrane receptor for FA, is often overexpressed in ovarian, lung, breast, and hematopoietic myeloid cancers. Because the FR is either absent from normal tissues or localized to the apical surfaces of polarized epithelia (where it is inaccessible to circulating drugs), FA-linked drugs do not normally accumulate in healthy tissues [217]. However, due to its full accessibility on tumor cells, the FR has been widely exploited as a target, particularly in TNBC [218]. For example, FA-modified UCNPs can specifically target and bind to overexpressed FR on BC cell surfaces, enabling efficient internalization and exhibiting strong fluorescent signals in MCF7, MDA-MB-231, and MDA-MB-468 cells [219–222]. As another critical target,

integrins play a role as indicators of metastasis. Their diagnostic significance is particularly pronounced in BC bone metastasis detection, where osteoclast-specific overexpression of  $\alpha v \beta 3$  integrin within osteolytic lesions provides unique pathological signatures. Building upon this mechanism, investigators developed arginine-glycine-aspartic acid peptide-conjugated UCNPs as advanced nanotheranostic probes. These engineered NPs demonstrated rapid tumor targeting within 1 hour post-administration, maintaining a robust tumor-to-background ratio of 24 throughout the 24-hour monitoring period. Notably, their tissue penetration depth reached an unprecedented 600  $\mu\text{m}$ , representing a threefold improvement over conventional visible-light imaging agents [223].

Furthermore, addressing the critical limitation of tissue penetration depth in current intraoperative near-infrared-I (NIR-I, 700–900 nm) fluorescence imaging for BC, Zhang et al. advanced the field by engineering integrin-targeted NPs optimized for near-infrared-IIb (NIR-IIb, 1500–1700 nm) emission (Figure 9). This nanoplatform demonstrated remarkable tissue penetration in the NIR-IIb region, with its signal-to-background ratio at 5 mm depth fourfold higher than that of the clinical reagent indocyanine green. Additionally, NIR-IIb imaging showed significantly enhanced signal-to-background ratio in lymph node visualization, enabling high-resolution angiography of brain and hindlimb vessels with narrower vascular profiles and superior contrast. In transgenic MMTV-PyVT mice, the nanoprobe discriminated malignant from normal tissues with an area under the receiver operating characteristic curve of 0.89, achieving 93.8% sensitivity and 79.4% specificity. Notably, across multiple tumor models, the platform precisely targeted tumors, identified microtumors as small as 2 mm, and guided complete resection. In an intramuscular tumor-invasion model, NIR-IIb imaging-guided surgery eliminated tumor recurrence at 14 days, whereas 4/5 mice in the white-light group exhibited recurrence. This technology presents a novel solution to enhance surgical precision and reduce positive margin rates in BC resection [224].

## 7.2. Dual-modal/multimodal imaging

Single-modal imaging technologies typically capture only single-type information within biological systems. To address this limitation and acquire comprehensive data, dual-modal/multimodal imaging techniques have been developed. Introducing multifunctional moieties into the lattice or surface of UCNPs extends their application beyond fluorescence imaging, encompassing modalities such as magnetic resonance imaging (MRI), computed tomography (CT), and positron emission tomography (PET). This integration leverages complementary detection principles to synergistically enhance imaging contrast while reducing the dosages of contrast agent (CA).

MRI is one of the most sensitive modalities for BC detection, particularly for identifying occult lesions and preoperative evaluation of breast-conserving surgery. However, the commonly used MRI CA gadolinium diethylenetriamine pentaacetate

suffers from rapid clearance and low relaxivity, requiring high doses that increase biological burden [225]. Paramagnetic RE ions  $Gd^{3+}$  and  $Eu^{2+}$  are commonly used as T1 CA, while  $Dy^{3+}$  and  $Ho^{3+}$ , due to their large magnetic moments, are typically employed as T2 CA. For example, Wei et al. developed  $NaGdF_4:Nd@NaLuF_4$  NPs for dual-modal imaging of TNBC (Figure 10A). Under 808 nm laser excitation, the probe exhibited strong fluorescence emissions at 1060 nm and 1340 nm, with a tumor-to-background ratio of 8.2 at 1340 nm. It enabled rapid hepatobiliary clearance with a 15.8 h half-life in the liver, avoiding long-term retention in the reticuloendothelial system. In vivo experiments showed the fluorescence signal peaked at 4 h post-injection, and 4T1 tumor MRI signals were enhanced by 1.46-fold at 240 min, enabling precise BC detection and boundary delineation [226]. However, RE incorporation into MRI may compromise magnetic field exchange efficiency, limiting image enhancement [227]. This has spurred interest in transition metal ion-based nanomaterials, which exhibit paramagnetic, superparamagnetic, or ferromagnetic properties coupled with favorable biocompatibility. Additionally, the integration of magnetic materials with UCNPs yields dual-modal imaging composites, significantly enhancing T<sub>2</sub>-weighted imaging performance [228–231].

Recently, multimodal imaging combining UCL/MRI/CT or UCL/MRI/PET has gained traction, integrating advantages to improve spatial resolution, sensitivity, and diagnostic efficiency. CT plays a pivotal role in evaluating lymph node status and metastases in BC via high-resolution anatomical imaging based on tissue-specific X-ray attenuation [232]. While iodinated CA remain clinical standards for safety and cost, their limited radiodensity has spurred the development of high-atomic-number element-based UCNPs. [233]. For example, Yb demonstrates superior X-ray attenuation capabilities with an absorption coefficient of  $3.88\text{cm}^2\cdot\text{g}^{-1}$  at 100 keV, significantly surpassing Gd ( $3.11\text{cm}^2\cdot\text{g}^{-1}$ ) and doubling the radiodensity of iodine-based agents ( $1.94\text{cm}^2\cdot\text{g}^{-1}$ ). As a sensitizer,  $Yb^{3+}$  enhances the emission of UCNPs via its large NIR absorption cross-section. In 2018, Yu et al. synthesized Y<sub>1</sub> receptor ligand-modified  $LiLuF_4:Yb,Er@nLiGdF_4@mSiO_2$  nanocomposites for trimodal BC imaging (Figure 10B). The  $LiLuF_4:Yb,Er$  core generated UCL under 980 nm laser excitation, while  $Gd^{3+}$  ions in the shell enabled MRI with a longitudinal relaxivity of  $10.24\text{Mm}^{-1}\cdot\text{s}^{-1}$ . The high atomic numbers of RE ions ( $Lu^{3+}$ ,  $Yb^{3+}$ ,  $Gd^{3+}$ ) enabled CT imaging, with CT values linearly correlating with nanocomposite concentrations. Animal studies demonstrated that Y<sub>1</sub> receptor ligand modification facilitated targeting of Y<sub>1</sub> receptor-overexpressing BC, with gradually enhanced UCL and MRI signals in tumor sites post intravenous injection. The accumulation of nanocomposites in MCF-7 tumors was twice that of the unmodified group [168].

PET, a molecular nuclear medicine modality, assesses distant organ metastases in BC but suffers from suboptimal spatial resolution due to limitations in conventional scintillation detectors. Moreover, existing radionuclide labeling strategies also face challenges like harsh conditions, multi-step protocols, and low yields [234]. Leveraging the strong adsorption properties of RE ions toward radionuclides, the

conjugation of radionuclides onto the surface of UCNP offers a promising approach. In 2020, Li et al. developed FA-modified, red blood cell membrane-coated UCNP with a pretargeting strategy for TNBC MRI/UCL/PET imaging (Figure 10C). They prepared red blood cell membrane vesicles, fused them with UCNP, and modified the complex with 1,2-distearoyl-sn-glycero-3-phosphoethanolamine-N-[FA(PEG)-2000]. In 4T1 tumor-bearing mice, these NPs achieved efficient tumor accumulation through FA-mediated targeting and red blood cell membrane-enabled immune evasion, showing peak UCL signals at 36 h post-injection that persisted for 48 h. The Gd<sup>3+</sup>-containing core significantly enhanced tumor MRI contrast versus controls. For PET imaging, mice received pre-injections of 1,2-distearoyl-sn-glycero-3-phosphoethanolamine-N-[azido(PEG)-2000]-modified NPs followed by <sup>18</sup>F-labeled Al<sup>18</sup>F-NETA-L-DBCO for in vivo click chemistry. The FA-modified group exhibited peak tumor radiotracer uptake at 0.5 h with minimal radiation exposure in non-targeted organs [208]. Similarly, Fang et al. fabricated tumor cell membrane-decorated Gd<sup>3+</sup>-doped upconversion nanoprobe, which successfully differentiated MDA-MB-231 and MCF-7 tumor models in vivo through UCL/MRI/PET imaging [235].

### 7.3. Lymph node visualization

Metastasis stands as the predominant cause of therapeutic failure and mortality in BC. As lymph nodes typically represent the first site of metastasis, accurate assessment of their status and treatment of metastatic lymph nodes are of utmost importance. Current guidelines recommend dual-tracer approaches combining radionuclides with blue dyes for lymph node identification. However, this approach confronts substantial limitations, including restricted availability of radioisotopes, stringent regulatory requirements for radiopharmaceutical disposal, inherent instability of short-lived isotopes, and risks of allergic reactions or persistent cutaneous pigmentation associated with dye-based tracers [236].

In recent years, engineered UCNP have emerged as a breakthrough solution for precise localisation of lymph nodes and identification of metastasis. As illustrated in Figure 11A, following subcutaneous administration, engineered UCNP exhibit superior lymphatic system penetration and selective accumulation in draining lymph nodes, coupled with real-time imaging capabilities [237]. On this basis, Qiu et al. developed a probe for detecting lymph node metastasis in BC, which employed anti-HER2 antibody-modified NaGdF<sub>4</sub>:Yb,Tm,Ca@NaLuF<sub>4</sub> NPs (Figure 11B). The results showed that the characteristic emission of the nanoprobe at 804 nm achieved a penetration depth of 7.7 mm through mouse skin tissues, significantly greater than the emissions at 655 nm and 541 nm from commonly used Er-doped UCNP, which endowed higher sensitivity for diagnosis. Cell binding assays demonstrated that the covalently attached anti-HER2 antibodies conferred excellent binding specificity to HER2-positive cancer cells in vitro, thereby enabling the in vivo detection of BC lymph node metastasis. Pharmacokinetic studies revealed that antibody conjugation

prolonged the blood half-life of UCNPs, reduced liver and spleen uptake, and accelerated biliary excretion [238]. In another study, Zhu et al. developed an NIR-IIb fluorescent probe to enhance imaging depth. Following subcutaneous injection, the probe drained to sentinel lymph nodes via the lymphatic system and entered BC cells through C-X-C motif chemokine receptor 4-mediated endocytosis. Under 808 nm laser excitation, the probe emitted NIR fluorescence at 1,556 nm, with a penetration depth of 7 mm. It showed significantly stronger fluorescence signals in metastatic sentinel lymph nodes. In mouse and human BC xenograft models, this probe achieved a sensitivity of over 92% and a specificity of 96% in detecting sentinel lymph node metastasis [239].

Besides, Zhang et al. designed UCNPs capable of chelating radionuclides, which were applied not only for lymph node imaging but also for targeted radionuclide therapy of BC lymph node metastasis (Figure 11C). Animal experiments demonstrated that this therapeutic approach significantly reduced the incidence of lymph node metastasis and the volume of metastatic foci. Notably, it showed no significant abnormalities in hematological, hepatic, and renal functions in mice, thus providing a safe and effective novel strategy for the diagnosis and treatment of BC lymphatic metastasis [201]. Meanwhile, Fang et al. developed a cell membrane-anchored ratiometric UCNPs for monitoring matrix metalloproteinase secretion and imaging metastatic lymph nodes (Figure 11D). The nanoprobe was constructed with UCNPs modified with Cyanine 3, a monitoring matrix metalloproteinase substrate peptide, and an anti-epidermal growth factor receptor antibody. In vivo imaging of metastatic lymph nodes in MDA-MB-231 tumor-bearing mice revealed pronounced fluorescence signals in metastatic lymph nodes, validating the specificity and reliability of the nanoprobe [240]. Additionally, Li et al. developed a liposome-coated UCNPs that enabled precise intraoperative localization of sentinel lymph nodes with an exceptional signal-to-background ratio. Notably, over 90% of the NPs were eliminated via the hepatobiliary pathway within 72 hours post-injection, effectively mitigating potential long-term toxicity [241].

## **8. UCNPs for detection BC biomarkers**

The development and progression of BC involve a multilevel cascade of abnormalities across molecular, cellular, and histological levels. Unlike overt morphological alterations in advanced stages, early-stage lesions frequently exhibit abnormalities at the biomolecular level. Implementing strategies to detect these tumor biomarkers can improve the early diagnosis rate and enhance the accuracy of subsequent treatment by leveraging detailed molecular-level information. Conventional techniques such as immunohistochemistry (IHC), western blotting (WB), and enzyme-linked immunosorbent assay (ELISA) have limitations in sensitivity, operational complexity, and cost-effectiveness. UCNP-based detection technology has emerged as a promising tool for BC biomarker analysis, leveraging its NIR excitation interference resistance and capacity for multiplexed narrow-band emission. This framework mainly includes two strategic paradigms [242,243]. One is

homogeneous assays that rely on energy transfer mechanisms such as Förster resonance energy transfer (FRET), realizing rapid "mix-and-read" detection through the modulation of donor-acceptor distance. The other is heterogeneous assays that use high-specificity solid-phase recognition interfaces, including microarray platforms and lateral flow chromatography. This section focuses on UCNP-based detection systems for BC biomarkers, classified according to the type of biomarker being targeted (Table 5).

### 8.1. Protein

ER, PR, and HER2 serve as critical biomarkers for molecular subtyping and therapeutic decision-making in BC [244]. In 2020, Farka et al. engineered UCNP-based nanoconjugates for HER2 quantification. When applied to HER2-positive BT-474 cells, these conjugates achieved a 50-fold enhancement in the signal-to-background ratio compared to conventional fluorescent labeling. Additionally, UCNP labeling demonstrated compatibility with H&E staining, neither interfering with signal acquisition nor compromising diagnostic accuracy [245]. Similarly, Gorris et al. developed streptavidin-PEG-UCNP conjugates modified with alkyne-PEG-neridronate, which enabled specific binding to HER2 via biotinylated anti-HER2 antibodies. The optimized conjugates exhibited an unprecedented signal-to-background ratio of 300 or more in IHC, thereby allowing high-contrast imaging of HER2 overexpression on BC cell membranes without optical background interference [246].

Notably, the identification of potential diagnostic markers from a plethora of oncoproteins necessitates technologies for quantitative analysis of multiple biomarkers. For in situ multiplexed molecular mapping, accurate profiling can only be achieved by using single-band emission nanoprobe to eliminate crosstalk between labeling signals. In response to this need, Zhou et al. developed nanoprobe capable of emitting blue, green, and red single-band light, which were used to enable simultaneous in situ molecular imaging and quantitative detection of ER, PR, and HER2 in BC cells and tissues (Figure 12A). Multispectral confocal microscopy revealed precise subcellular localization of the probes, with ER and PR distinctly labeled in the nucleus and HER2 on the membrane of both MCF-7 and MDA-MB-231 cells. Quantitative analysis revealed ER/PR/HER2 expression levels of 76%/79%/65% in MCF-7 cells versus 5%/11%/4% in MDA-MB-231 cells, aligning with WB. In clinical BC tissues, nanoprobe quantification strongly correlated with IHC for high-abundance biomarkers. Notably, the combined nanoprobe-spectroscopic analysis improved the accuracy of detecting low-expression targets compared with IHC alone, demonstrating potential for resolving ambiguous biomarker expression cases [247].

As a key driver of BC progression, tumor-secreted vascular endothelial growth factor (VEGF) not only stimulates angiogenesis but also directly promotes tumor expansion, rendering its detection of critical clinical significance. As nucleic acid molecules,



aptamers offer distinct advantages over traditional antibodies, including high chemical stability, easy modifiability, strong specificity, small molecular weight, and non-immunogenicity, and enable the functionalization of UCNPs via a simple one-step exchange strategy. In 2016, Lan et al. synthesized NaYF<sub>4</sub>:Yb,Er NPs, replacing the surface oleic acid with aptamer DNA to construct a microplate-based detection system. The capture probe immobilized VEGF, which then bound to the UCNP-labeled auxiliary probe. This method exhibited a linear relationship between UCL intensity at 541 nm and VEGF concentration in the range of 50–2000 pM, with a limit of detection (LOD) of 6 pM. In spiked serum samples, the recovery of 500 pM VEGF ranged from 98% to 113%, with relative standard deviations of 2.9%–3.6%. The high specificity of aptamers for VEGF effectively eliminated interference from serum albumin in complex serum matrices [248]. In contrast to the microplate-based detection system, the sensitive aptasensor based on FRET employs a homogeneous assay strategy that eliminates the need for separation steps, offering improved operational simplicity and sensitivity. For instance, Yuan et al. developed a highly sensitive FRET-based aptasensor for VEGF<sub>165</sub> detection, using PAA-modified UCNPs as energy donors and MoS<sub>2</sub> nanosheets as acceptors. FRET triggered by aptamer-MoS<sub>2</sub> physical adsorption quenched UCNP fluorescence by 95%. Upon VEGF<sub>165</sub> addition, aptamer binding induced conformational changes, weakening van der Waals forces with MoS<sub>2</sub> to separate donor-acceptor pairs, inhibiting FRET and restoring fluorescence. The linear fluorescence recovery range for VEGF<sub>165</sub> was 0.1–16 ng/mL with a 0.1 ng/mL detection limit [249].

## 8.2. Glycoprotein

Serum tumor markers serve as indispensable indicators for cancer screening, monitoring recurrence, and guiding therapeutic strategies. Cancer antigen 15-3 (CA15-3), a transmembrane glycoprotein from the MUC-1 family detected by monoclonal antibodies DF3 and 115D8, is widely expressed in breast, lung, ovarian, and pancreatic malignancies. Since the 1980s, serum CA153 levels have been used as a diagnostic and assessment indicator for BC [250–252]. In 2022, Liang et al. developed a homogeneous biosensor for the detection of CA15-3 in human serum based on the FRET strategy (Figure 12B). The biosensor uses NIR-excitable UCNPs as the energy donor and the commercial organic dye as the energy acceptor, which are linked by a molecular beacon containing the CA153 aptamer sequence. The upconversion fluorescence of UCNPs can be effectively quenched by dye. In the presence of CA15-3, the hairpin structure of molecular beacon is opened, leading to the separation of UCNPs and dye and the inhibition of FRET, so the fluorescence is recovered. In HEPES buffer, the fluorescence has a linear relationship with the logarithm of CA15-3 concentration in the range of 0.01–150 U/mL, with an LOD of 4.5 mU/mL. The probe has good selectivity and can be successfully applied to the detection of CA15-3 in human serum, providing a useful tool for the early diagnosis of BC [253].

Similarly, Cancer antigen 125 (CA125), another key biomarker derived from the

MUC1 gene, plays a central role in regulating multicellular survival pathways within BC cells [254]. In response, researchers developed an upconversion fluorescence biosensor for CA125 detection by constructing a "sandwich" structure using surface-modified UCNPs and silver NPs conjugated with CA125 antibodies and antigens, achieving fluorescence quenching with a linear detection range of 5–100 ng/mL [255]. Meanwhile, Zhang et al. utilized carbon dots as energy acceptors, combined with aptamer-modified UCNPs through  $\pi$ - $\pi$  stacking interactions to quench UCL. In the presence of CA125, the UCL was restored, enabling an LOD as low as  $9.0 \times 10^{-3} \text{ U} \cdot \text{mL}^{-1}$  and demonstrating excellent performance in human serum [256]. Recently, Ekman et al. developed a spectrally separated dual-label UCL lateral flow assay to simultaneously detect cancer-specific STn-glycosylated forms of CA125 and CA15-3. Using  $\text{Er}^{3+}$ -doped (540 nm emission) and  $\text{Tm}^{3+}$ -doped (450 nm emission) UCNPs conjugated with anti-CA125/CA15-3 antibodies, the assay employed a single test line immobilized with anti-STn antibody to capture target glycoproteins. The dual-label lateral flow assay discriminated ascites samples from cancer patients and liver cirrhosis controls, with LOD for CA125-STn at 1.8 U/ml in buffer and 3.6 U/ml in ascites, and a linear range of 1-2500 U/ml [257].

Carcinoembryonic antigen (CEA), the first tumor antigen studied as a glycoprotein molecule associated with cell adhesion, exhibits elevated serum levels that may indicate the presence of malignant tumors in endodermal tissues, including the breast [258]. Given its clinical significance, extensive research has focused on improving detection sensitivity and specificity, leading to the design of a series of innovative detection systems based on UCNPs. Among these, the most widely studied paradigm utilizes UCNPs as energy donors in combination with nanomaterials as energy acceptors, enabling quantitative detection of CEA through fluorescence signal quenching or recovery [259–261]. For instance, Yu et al. proposed a modification-free fluorescent biosensor based on polydopamine (PDA)-coated UCNPs for the detection of CEA. The biosensor consisted of UCNPs@PDA and CEA aptamer-functionalized gold nanoparticles (AuNPs). Due to the  $\pi$ - $\pi$  stacking and hydrogen bonding interactions, the CEA aptamer on AuNPs was adsorbed onto the surface of UCNPs@PDA, triggering the FRET from UCNPs@PDA to AuNPs-CEA aptamer and leading to the quenching of fluorescence. In the presence of CEA, the AuNPs-CEA aptamer detached from UCNPs@PDA because of the stronger affinity between CEA and its aptamer, blocking the FRET process and thus recovering the fluorescence, which enabled the quantitative analysis of CEA concentration [262].

Additionally, addressing the limitations of traditional optical intensity-based detection, the composite signal conversion paradigm based on UCNPs has emerged. For instance, to enhance detection sensitivity, Qiu et al. developed a photoelectrochemical aptasensing platform using core-shell  $\text{NaYF}_4:\text{Yb},\text{Tm}@\text{TiO}_2$  upconversion microrods, leveraging NIR to UV light conversion to activate  $\text{TiO}_2$ -mediated photocurrent generation. The platform integrated target-triggered rolling circle amplification, where CEA binding initiated this process to generate guanine-rich strands digested by

exonucleases, releasing free guanines that enhanced photocurrent. This design exhibited a linear range of 10 pg/mL to 40 ng/mL for CEA, with an LOD of 3.6 pg/mL, high selectivity against interferents, and reproducible responses under repeated NIR illumination. Validation in human serum samples showed strong agreement with commercial ELISA, confirming its clinical utility [263]. To address the clinical need for wide dynamic range detection, Shao et al. constructed a trimodal sensing platform using three-layer dumbbell-like UCNPs combined with G-quadruplex DNAzyme. By tuning  $\text{Nd}^{3+}$  doping, the platform integrated UCL, photothermal, and colorimetric signals. The UCL mode achieved a linear range of 0.005–50 ng/mL, the photothermal mode covered 50–2000 ng/mL, and the colorimetric mode spanned 10–1000 ng/mL, providing a comprehensive detection range of 0.005–2000 ng/mL [264]. In another study, Xu et al. developed an aptamer-based biosensor using encoded UCNPs for digital detection. The system formed a "magnetic bead-aptamer-UCNPs" sandwich structure, where CEA binding dissociated complementary DNA-UCNPs from magnetic beads due to stronger aptamer-CEA affinity. The released UCNPs were counted via fluorescence microscopy, establishing a linear relationship with CEA concentration. This label-free counting strategy avoided energy transfer dependencies and background interference, offering a novel path for ultrasensitive detection in complex matrices [265].

### 8.3. Nucleic acids

Nucleic acids, serving as the carriers of genetic information storage and transmission, exhibit dysregulation closely linked to the progression of cancer. The detection of nucleic acids using UCNPs stands out for its unique integration of nanoscale assembly strategies and signal transduction mechanisms, enabling unprecedented in situ quantification. For instance, thymidine kinase 1, a key enzyme in DNA synthesis and cellular proliferation, has been investigated as a prognostic marker and early indicator of treatment response in HER2-negative early and metastatic BC. Gao and colleagues developed spiny nanorod-UCNP satellite assemblies for ultrasensitive detection of thymidine kinase 1 messenger RNA (mRNA) in living cells. The design relied on target recognition to dissociate UCNPs from the matrix, thereby restoring UCL. This strategy achieved an LOD of 0.67 fmol/10  $\mu\text{g}$  RNA and successfully quantified mRNA levels in MCF-7 and HeLa cells, demonstrating its utility for intracellular nucleic acid analysis [266]. Furthermore, to integrate detection and therapy, a theranostic nanobeacon was constructed, combining a thymidine kinase 1 mRNA-specific molecular beacon with UCNPs and loading the chemotherapeutic drug. The nanobeacon enabled ratiometric UCL detection of thymidine kinase 1 mRNA with an LOD of 1.1 nM, while target binding triggered drug release for chemotherapy [267].

Moreover, Li et al. constructed DNA-driven chiroplasmonic nanopyramids by self-assembling AuNPs and UCNPs, creating a dual-mode sensing platform that combined plasmonic circular dichroism and UCL for microRNA-21 detection in MCF-7 cells. The nanopyramids displayed a circular dichroism signal at 521 nm and

UCL in the 500-600 nm range, with circular dichroism intensity decreasing and UCL increasing upon microRNA-21 binding, achieving an LOD of 0.03 fmol/10  $\mu$ g RNA due to plasmonic enhancement of DNA chirality, which enabled precise quantification of microRNA-21 in MCF-7 cells and distinguished them from normal uterine fibroblast cells based on expression levels [268]. In another study, Zhang et al. advanced this paradigm with lock-like DNA-programmed UCNPs-AuNPs assemblies, where a hairpin DNA hybridized with a bolt DNA to form lock-like DNA, tethering AuNPs to UCNPs and quenching UCL via FRET (Figure 12C). When microRNA-21 was present, fuel hairpin DNA triggered cyclic disassembly. This allowed a single microRNA-21 molecule to repeatedly unlock multiple lock-like DNA units and dissociate AuNPs from UCNPs, restoring UCL with nonenzymatic signal amplification. This strategy achieved an ultra-low LOD of  $0.74 \times 10^{-15}$  M for microRNA-21, approximately 1000 times more sensitive than non-amplified probes, and clearly distinguished MCF-7 cells from normal L-02 cells by imaging intracellular microRNA-21 levels, leveraging target cycling to generate high signal gain suitable for detecting low-abundance microRNAs in BC cell [269].

Meanwhile, circulating tumor DNA (ctDNA) has emerged as a critical biomarker for BC management, owing to its short half-life and ability to reflect disease status in real time [270]. However, ctDNA detection faces challenges such as ultra-low abundance, fragment brevity, and rapid degradation, while conventional sequencing methods often fail due to background noise masking tumor-derived signals. Wang et al. designed a satellite assembly nanoprobe combining UCNPs and gold nanocages, adjusting the excitation and emission wavelengths of UCNPs to the NIR region via doping with Yb and Tm ions. By constructing an FRET system through complementary DNA pairing between UCNPs and gold nanocages with corresponding wavelength absorption, and using toehold-mediated strand displacement reaction for signal transduction, this approach achieved sensitive detection of KRAS gene point mutations with an LOD of 6.30 pM [271]. Gong et al. further developed an NIR light-responsive ctDNA capture-release platform. By using UCNPs to convert NIR light into UV light, the platform triggered the trans-cis isomerization of azo units, enabling the reversible release of ctDNA-probe complexes. This allowed the detection chip to be reused, providing new ideas for quantitative analysis of ctDNA and personalized diagnosis of cancer [272].

## 9. UCNPs for BC phototherapy

Phototherapy boasts a history of thousands of years, with ancient records in India, China, and Egypt document the use of sunlight for treating skin diseases [273]. The invention of the laser in 1960 revolutionized phototherapy, enabling applications in ophthalmic surgery and tumor ablation [274]. While laser-based phototherapy exhibits less systemic toxicity than traditional chemotherapy due to its localized action, it still harbors critical limitations. Endogenous chromophores in non-malignant tissues cause off-target effects, compromising selectivity for malignant cells. Additionally, the requirement for high power density in laser therapy raises safety concerns and

logistical challenges. In response, photodynamic therapy (PDT) using exogenous photosensitizers (PS) and photothermal therapy (PTT) employing photothermal agents (PTA) have emerged to provide more targeted and effective therapeutic options [275]. However, current PDT and PTT face significant drawbacks. For instance, most PS are constrained by their absorption primarily in the UV/visible spectra, leading to strong tissue absorption/scattering and shallow penetration. Some PTA suffer from insufficient biocompatibility and low photothermal conversion efficiency. Furthermore, the lack of imaging guidance and real-time efficacy monitoring during treatment often causes unintended damage to normal tissues [276]. Against this backdrop, composite systems integrating UCNPs with PS or PTA have emerged as promising solutions. These systems not only overcome the limitation of treatment depth by leveraging NIR light-induced short-wavelength emission from UCNPs but also enhance photothermal conversion efficiency. More importantly, the excellent imaging capabilities of UCNPs enable real-time therapeutic guidance, significantly improving treatment precision and safety. Herein, we deliver an in-depth exploration of UCNP-based phototherapy for BC (Table 6).

### 9.1. Photodynamic therapy

PDT has been a clinically proven method for over 40 years in the treatment of superficial skin lesions, esophagus, lung and bladder tumors [277,278]. It is based on three essential elements: oxygen, PS, and specific radiation. As illustrated in Figure 13, the resulting photodynamic response diverges into two distinct mechanisms. Type I reactions entail direct hydrogen or electron transfer, leading to the generation of free radicals that induce oxidative stress and ultimately result in cell death. Type II, more prevalent in PDT, entails energy transfer to oxygen to form highly reactive singlet oxygen ( $^1\text{O}_2$ ), which damages nearby biomolecules and leads to cell death [279]. As the key component of PDT, PS have optical properties that directly affect treatment efficacy. Conventional PS, including first-generation porphyrins, second-generation chlorophyll derivatives, and third-generation phthalocyanines, mainly absorb light in the 400–700 nm range. However, biological tissues exhibit strong scattering and absorption in this spectral band, which severely restricts the efficacy of PDT.

Novel UCNP-based PDT systems use engineered UCNPs as converters, efficiently absorbing high-penetration NIR light with minimal damage, and emitting UV/visible light to activate PS, thus enhancing PDT efficacy. For example, Khaydukov et al. developed UCNPs converting 975 nm light to UV-blue light for riboflavin activation in BC treatment. With 2% UV-blue and 9.5% total conversion efficiency, these UCNPs showed significant cytotoxicity in SK-BR-3 cells under 975 nm light in vitro. In immunodeficient mice, injecting UCNP-riboflavin mixtures around tumors, then NIR irradiation, inhibited tumor growth by 90% in 50 days. This approach extended the treatment depth to 4–6 mm, tenfold deeper than conventional UV-blue light [280]. Besides, Yong Zhang and colleagues developed a silk-fibroin-coated implant by incorporating submicrometer UCNPs into polydimethylsiloxane for remote orthotopic PDT. In vitro, this implant induced approximately 48% ROS in MCF7 cells and 37%

in MDA-MB-231 cells, representing a fivefold increase over conventional implants. It also promoted significant apoptosis. In orthotopic breast cancer mouse models, the implant reduced tumor burden by 60% compared to controls. The system achieved 1.0 cm tissue penetration depth under NIR excitation, and its clinical prototype integrated both cosmetic and therapeutic functions, demonstrating potential for deep tumor therapy [281]. In another study, bio-nanohybrids of KillerRed covalently conjugated to UCNPs were efficiently internalized by MDA-MB-231 cells and distributed in the cytoplasm. Under 980 nm NIR excitation, UCNPs converted NIR light to green light, effectively activating KillerRed to generate ROS. This achieved approximately 70% PDT efficiency through 1 cm-thick tissue, whereas the efficiency of conventional KillerRed dropped to only 7% under the same condition [282].

Building on targeted approaches, Ramírez-García et al. designed an immunoconjugated upconversion nanocomplex specifically for HER2-positive BC imaging and PDT. They synthesized NaYF<sub>4</sub>:Yb,Er UCNPs via thermal decomposition, modified them with cysteamine, covalently linked zinc phthalocyanine (ZnPc), and conjugated the HER2-targeting antibody trastuzumab. This complex efficiently converted 975 nm light into 659 nm red emission from the UCNPs, subsequently triggering ZnPc to generate <sup>1</sup>O<sub>2</sub> with a high energy transfer efficiency of 84.3%. Confocal microscopy confirmed selective binding to HER2-positive SKBR-3 cells with minimal attachment to HER2-negative MCF-7 cells. Under NIR irradiation for just 5 minutes, the nanocomplex at 200 µg/mL reduced SKBR-3 cell viability to 21%, compared to 93.5% viability without light [216]. Zhang et al. proposed in 2017 a strategy integrating UCNPs with graphene quantum dots for mitochondria-specific PDT. Under NIR excitation, the UCNPs emitted UV-visible light that activated the graphene quantum dots to produce <sup>1</sup>O<sub>2</sub>. Modification with tetramethylrhodamine isothiocyanate endowed the platform with mitochondrial targeting capability, enabling in-situ <sup>1</sup>O<sub>2</sub> generation within mitochondria. This process significantly decreased mitochondrial membrane potential, activated caspase 3, and triggered tumor cell apoptosis. In vitro experiments showed significantly higher cytotoxicity against 4T1 cells under light irradiation compared to non-targeted controls, while maintaining biocompatibility in the dark. In vivo studies demonstrated a 75.3% tumor inhibition rate in 4T1 tumor-bearing mice, outperforming the non-targeted system [283]. Similarly, Liu et al. designed a Nd<sup>3+</sup>-sensitized upconversion composite for NIR light-triggered, mitochondria-targeted PDT. The composite was composed of UCNPs and porphyrinic metal-organic frameworks, which were further surface-functionalized with triphenylphosphine (a mitochondria-targeting ligand), enabling the generation of <sup>1</sup>O<sub>2</sub> activated by 808 nm light [284]. Additionally, strategies responsive to the TME have been developed, such as pH-sensitive targeting systems that enhance tumor accumulation and PDT efficacy by exploiting the acidic TME [285].

Leveraging the inherent imaging capabilities of UCNPs, Jin et al. developed an NIR-regulated theranostic nanoplatform in 2019 (Figure 14). They encapsulated UCNPs and an aggregation-induced emission luminogen within an amphiphilic

polymer and conjugated cyclic arginine-glycine-aspartic acid peptide for targeting. Excitation at 980 nm yielded a  $^1\text{O}_2$  quantum yield of 36.4%, with light penetration up to 6 mm of tissue. The nanocomposite retained 75% of its initial fluorescence intensity after 10 days, outperforming commercial probes. Following intravenous injection, it showed time-dependent tumor accumulation, peaking at 8 hours. In vitro, it specifically targeted  $\alpha\text{v}\beta 3$  integrin-overexpressing MDA-MB-231 cells, reducing viability to 28.3% under NIR-mediated PDT. In vivo, it achieved a 75% tumor growth inhibition rate in MDA-MB-231 tumor-bearing mice [286]. Similarly, Lv's team created degradable peptide-modified NPs for NIR-II imaging and UCL-guided PDT of TNBC. Synthesized via double emulsion, the composite integrated ultra-small UCNPs, polymers, and embedded ZnPc. Under 980 nm excitation, the core-shell structure exhibited enhanced 650 nm red emission with 38.3% energy transfer efficiency and superior NIR-II imaging. In vitro, it induced effective PDT and degraded into sub-6 nm particles. In vivo, the peptide modified composite selectively targeted MDA-MB-231 tumors, significantly inhibiting growth while maintaining biocompatibility and low toxicity [152]. In conclusion, UCNPs appear to be a promising carrier for targeted PDT of BC.

## 9.2. Photothermal therapy

PTT employs PTA to convert light energy into heat, inducing irreversible thermal ablation of tumor cells through localized hyperthermia [287]. Its biological effects exhibit distinct temperature-dependent characteristics. At 41 °C, cells initiate a heat-shock response involving altered gene expression and heat-shock protein production to counteract initial damage. At 42 °C, tissues suffer irreversible injury. When exposed to 42–46 °C for 10 min, necrosis occurs, releasing intracellular damage-associated molecular patterns that may trigger inflammation. In the 46–52 °C range, cells rapidly undergo apoptosis (programmed cell death), a process preserving membrane integrity while externalizing "eat-me" signals like phosphatidylserine to facilitate phagocytic clearance, typically without significant inflammation [288,289]. Temperatures exceeding 60 °C cause instantaneous protein denaturation and membrane disruption, leading to immediate coagulative necrosis. PTT is categorized as traditional PTT ( $\geq 45$  °C) or increasingly utilized mild PTT ( $< 45$  °C), with the latter often serving as a regulatory mechanism rather than directly targeting tumor destruction [290]. However, the temperature regulation dilemma of PTT and the performance limitations of existing PTA have prompted researchers to focus on functional nanomaterials with unique optical properties. Recently, UCNPs have been integrated with conjugated polymers, organic dyes, plasmonic metals, carbon, and inorganic materials for PTT. This approach enhances PTA stability, biocompatibility, and absorption wavelength while enabling synergistic multimodal imaging integration with optimized energy conversion efficiency.

Gold-based nanomaterials including nanoshells, nanorods, nanostars, nanocages, and  $\text{Au}_{25}$  clusters induce SPR, making them widely used as PTA in PTT. Notably, smaller AuNPs exhibit reduced photothermal conversion efficiency under NIR irradiation due

to mismatch between their SPR absorption peaks (500–560 nm for NPs several nanometers in size) and NIR light [276]. In this regard, Gold-decorated UCNPs address this challenge. When excited by 980 nm NIR light, the NaYF<sub>4</sub>:Yb,Er@NaYF<sub>4</sub>@SiO<sub>2</sub> NPs generated green light through upconversion, a process that coupled with the SPR of AuNPs to enable photothermal conversion and thereby endowed the system with efficient photothermal killing effects against BE(2)-C neuroblastoma cells [291]. Moreover, to assess AuNPs versus gold nanorods (AuNRs) in absorbing energy from NaYF<sub>4</sub>:Yb,Er, Chen et al. synthesized UCNPs@SiO<sub>2</sub>@Au nanocomposites. They systematically investigated energy transfer mechanisms and efficiency from UCNPs to gold nanomaterials by characterizing variations in UCL intensity and photoluminescence lifetime. Results demonstrated UCNPs@SiO<sub>2</sub>@AuNRs exhibit nearly 26-fold higher heat generation efficiency than UCNPs@SiO<sub>2</sub>@AuNPs, attributed to enhanced SPR-UCL interaction in the nanorod-based system [292]. In a separate study, Jiang et al. engineered several classic inorganic-organic PTT nanocomposites by integrating UCNPs with copper sulfide, manganese dioxide, carbon, dopamine, and polypyrrole. Findings revealed PTT efficacy primarily stems from NIR light absorption, with UCL light conversion providing a secondary contribution [293].

To achieve precise spatial and temperature control in PTT, integrating imaging-guided technologies with photothermal nanoplateforms has become a research hotspot. For instance, Cheng et al. developed gold-coated UCNPs-iron oxide NP nanocomposites for dual-modal imaging via UCL and MRI-guided magnetically targeted PTT (Figure 15). In vivo imaging showed magnetic targeting yielded a 7-fold UCL signal increase in tumors versus non-targeted approaches. MRI confirmed an 8-fold rise in magnetic NP tumor accumulation. With magnetic targeting and NIR irradiation, all treated mice achieved complete tumor elimination without recurrence within 40 days and survived beyond 40 days, while controls averaged 14–18 days lifespan. Histology indicated nanocomposite accumulation in some organs caused no significant toxicity [294]. Moreover, researchers also leverage UCL temperature sensitivity for nanoscale thermal monitoring. Ramírez-García et al. constructed UCNPs-AuNPs composites where 975 nm excitation converts light to visible wavelengths. Green light excites the SPR of AuNPs, generating photothermal effects. Five-minute irradiation increased temperature from 37 °C to 42.2 °C, reducing MCF-7 viability by over 60%. Green emission band ratios enable 25–50 °C temperature monitoring, while 659 nm red emission facilitates cell imaging and tracking, providing a multifunctional nanoplateform for imaging-guided temperature-controlled photothermal therapy of BC [295]. Similarly, considering that prolonged treatment at 42–45 °C may damage normal tissues, Zhu et al. constructed a core-shell structured upconversion nanocomposite using a carbon shell as the PTA, enabling effective photothermal ablation of tumors in vivo while providing temperature feedback to reduce damage to normal tissues caused by overheating [296].

The combining of non-invasive PTT and PDT can achieve synergistic therapeutic



performance with attenuated light power. In 2014, Chen et al. achieved a milestone by loading UCNPs with rose bengal (RB) and IR825, creating the first UCNP-based PTT-PDT system. Under 980-nm excitation, RB absorbed UCNP-emitted green light to generate cytotoxic  $^1\text{O}_2$  for PDT, while IR825 provided strong photothermal conversion under 808 nm irradiation for PTT. In vitro, combined therapy demonstrated superior cancer cell killing versus monotherapies, reducing viability to near zero. In 4T1 tumor-bearing mice, combined PDT-PTT yielded only 15% relative tumor volume compared to individual therapies [297]. In Yang et al.'s study, a multifunctional core-satellite nanostructure was developed for combined PTT and PDT targeting microRNA-21 in MCF-7 cells. It employed the microRNA-21-triggered toehold-mediated strand displacement reaction to dissociate UCNP@Au. This dissociation enabled UCL restoration for in situ imaging of microRNA-21 and augmented  $^1\text{O}_2$  production for PDT, while the released AuNPs aggregated, resulting in a potent PTT effect. Under 808 nm laser irradiation, the combined PTT-PDT therapy significantly inhibited MCF-7 cells, reducing the survival rate below 40% [298]. Another study by Chu et al. reported UCNPs@AgBiS<sub>2</sub> NPs where concentration resonance between Nd<sup>3+</sup> ions and AgBiS<sub>2</sub> enhanced photothermal efficiency from 14.7% to 45%. Nd<sup>3+</sup>-doped UCNPs generated strong emissions exciting the AgBiS<sub>2</sub> shell for ROS production. These NPs showed cancer-specific cytotoxicity against 4T1 cells under 808 nm irradiation. In tumor-bearing mice, NPs elevated tumor temperature to 56.3 °C, causing sustained growth inhibition with significant tissue damage and no systemic toxicity [299].

## 10. Smart drug/gene delivery

Therapeutic agents aim to reach tumor sites via specific administration routes to trigger pharmacological responses. However, conventional formulations release immediately post-administration, with minimal amounts reaching lesions. Intrinsic physicochemical drug properties further limit efficacy. Commercial BC therapeutic drugs are broadly classified by water solubility into hydrophilic and hydrophobic categories (Table 7). Hydrophobic drugs, most common in BC, cannot cross aqueous phases, restricting intracellular target access. Hydrophilic agents face challenges including poor cellular uptake due to membrane penetration difficulty, rapid enzymatic degradation reducing bioavailability, and limited circulation times. These limitations often cause suboptimal therapeutic outcomes and systemic toxicity. For example, doxorubicin (DOX) associates with significant hematopoietic, gastrointestinal, and cardiac toxicities. Paclitaxel frequently causes neutropenia and peripheral neuropathy. Similarly, docetaxel, cisplatin, tamoxifen, and trastuzumab link to side effects like fatigue, weight loss, peripheral neuropathy, and nausea [300,301]. Nucleic acid drugs show remarkable potential for treating genetic disorders, tumors, and viral infections, positioning as the third major therapeutic class after small molecules and antibodies. However, their large molecular weight and negative charge impede biological membrane passage. Moreover, RNA is highly susceptible to ribonuclease degradation and often becomes trapped in endosomal vesicles post-internalization, failing to exert functional activity [302].

Drug delivery systems address these physicochemical challenges. Engineered UCNP are attractive candidates due to distinctive sizes, tunable surface functionalities, and regulated drug discharge. Encapsulating UCNP with polymers, proteins, or mSiO<sub>2</sub> provides drug/gene reservoirs while enhancing colloidal stability [303,304]. Drug loading typically involves mixing UCNP with agents in pH-specific solutions for certain durations. This method effectively encapsulates charged groups; positively charged coatings enhance gene loading efficiency. However, inert, uncharged, or hydrophobic groups often yield low encapsulation efficiencies [305]. Other approaches like chemical conjugation, in-situ synthesis, and supramolecular assembly aim to increase drug loading, improve stability, and achieve targeted delivery [306,307]. Recent understanding of TME and progress in materials engineering have enabled smart UCNP-based drug delivery systems. Unlike traditional methods, these platforms utilize responsive materials reacting to endogenous signals or exogenous stimuli. Activation triggers programmed structural reconstruction through chemical bond cleavage, phase transition, or pore opening, disrupting carrier-drug equilibrium for precise tumor-site release. Advances employing UCNP for smart release systems are summarized in Table 8, with representative applications reviewed below.

#### 10.1. Photo stimuli

Light-controlled delivery offers non-invasive characteristics and superior spatiotemporal precision. UCNP-assisted systems provide deeper tissue penetration via NIR excitation, minimized photodamage, no DNA/RNA harm, excellent biocompatibility, and robust photochemical degradation resistance. Efficient NIR-triggered systems require three elements: strong UCNP upconversion emission, effective photoresponsive material integration, and optimal NIR excitation parameters. Under NIR irradiation, photoresponsive components absorb UCNP-emitted visible/UV photons, initiating photochemical reactions that modify delivery system composition/conformation for controlled release.

As a representative example, Zhao et al. designed a yolk-shell NaYF<sub>4</sub>:Yb,Tm@NaLuF<sub>4</sub> nanocage with mSiO<sub>2</sub> shell, loaded with hydrophobized amino-coumarin-caged chlorambucil (Figure 16A). Under 980 nm NIR light, the system released over 50% chlorambucil within 6 hours and 68% after 15 hours in vitro, with 88% photolysis efficiency. In vivo studies on S180 tumor-bearing mice showed significant tumor growth inhibition and prolonged survival after intratumoral injection and NIR irradiation. This is the first NIR-regulated drug release system demonstrated in living animals, overcoming the low tissue penetration of traditional phototriggered devices [308]. Subsequently, Dcona and Matthew conjugated DOX to LiYF<sub>4</sub>:Tm,Yb NP surfaces via a photocleavable linker. Under 980 nm laser irradiation, NP emissions at 353/368 nm cleaved the nitroveratryl-glutamate linker to release DOX [309]. In 2018, Han et al. used  $\beta$ -cyclodextrin as a gatekeeper to cap 2-diazo-1,2-naphthoquinones via hydrophobic interaction. Upon UV light illumination from UCNP, the hydrophobic diazo-1,2-naphthoquinones were

converted to hydrophilic 3-indenecarboxylic acid. Consequently,  $\beta$ -cyclodextrin dissociated from the UCNPs@mSiO<sub>2</sub> surface due to repulsion between the hydrophobic cavities and hydrophilic guest, enabling the release of DOX from the unblocked pores [310]. Another system used FA-conjugated photo-responsive copolymers encapsulating mSiO<sub>2</sub>-coated UCNPs for tumor-targeted DOX delivery. Under a 980 nm laser, the emitted UV light modified copolymer structure to trigger rapid release in FR-overexpressing cells. [311].

Beyond small-molecule drugs, UCNPs-mediated NIR light-controlled systems have also demonstrated unique advantages in the field of gas signaling molecule controlled release. For example, endogenous messengers like NO regulate tumor vasculature and induce apoptosis, but their short half-life and diffusivity prevent spatiotemporal control. Coupling photosensitive gas donors with UCNPs enables deep-tissue NIR-triggered release, avoiding UV-associated damage. In 2015, Zhao's team integrated 980 nm-excited UCNPs with roussin's black salt, achieving controlled NO release where higher laser power triggered burst release activating apoptosis. Notably, low-dose NO reversed chemoresistance [312]. Subsequent work used 808 nm-excited UCNPs conjugated with roussin's black salt for NO delivery combined with DOX, suppressing tumor stem cell proliferation and metastasis (Figure 16B). Blue/UV light from these UCNPs promoted NO release, inducing apoptosis and reversing resistance via P-glycoprotein downregulation. The system inhibited MCF-7 mammosphere formation and CD44<sup>+</sup>/CD24<sup>-</sup> subpopulations in vitro while reducing tumorigenic potential of tumor stem cells in vivo [313].

Concurrently, UCNPs-mediated NIR light-controlled delivery systems have also demonstrated remarkable application potential in the field of nucleic acid therapeutics. Short interfering RNA (siRNA), a type of double-stranded non-coding RNA molecule, has emerged as a highly promising therapeutic agent, owing to its gene-regulatory capabilities. Specially, these molecules can silence specific genes, offering an innovative strategy to target previously undruggable signaling pathways in cancer treatment. However, the poor inherent stability of siRNA severely restricts its direct in vivo application, rendering it difficult to function as a standalone therapeutic agent. To expand therapeutic modalities, Zhang's team engineered mSiO<sub>2</sub>-UCNPs hybrids for NIR-controlled gene delivery, where UV-mediated cleavage of 4,5-dimethoxy-2-nitroacetophenone caging groups enabled precise release of functional plasmid DNA/siRNA [314]. Yang et al. developed different upconversion nanoplatforms that siRNA was covalently and stably linked on the upconversion nanocrystals surface by cationic photocaged linkers. Following cellular internalization and 980 nm laser irradiation, the emitted UV light effectively triggered siRNA release, which was further confirmed by gene silencing assays [315]. In another study, Xiang et al. developed an NIR-activatable DNA nanodevice integrating UCNPs with entropy-driven catalysis for mRNA imaging and antisense oligonucleotide release (Figure 16C). This platform demonstrated precise Bcl-2 antisense oligonucleotides delivery through UV-triggered DNA walker activation, inducing tumor apoptosis via

anti-apoptotic protein downregulation without transfection reagents, as validated in both in vitro and in vivo models [316].

## 10.2. pH stimuli

Under normal physiological conditions, the pH value in the extracellular matrix and blood is nearly 7.4. However, due to the rapid proliferation of tumor cells and the generation of irregular blood vessels, the tumor site lacks nutrients and oxygen. This causes the accumulation of lactic acid produced by glycolysis of tumor cells in the tumor interstitium, reducing the pH value of the extracellular environment of tumor cells to 6.5–7.2, while the pH value of endosomes and lysosomes within tumor cells further decreases to 4.0–6.0 [317,318]. This micro-acidic environment is prevalent in various tumors and plays a vital role in the generation and development of tumors, especially in drug resistance [319].

In view of this, pH-responsive UCNPs delivery systems are designed to remain stable under normal physiological conditions. Once reaching the tumor site, they are triggered by the slightly acidic environment to undergo processes such as protonation, expansion, surface charge reversal, or chemical bond cleavage, thereby achieving the goal of drug release. For example, Qiao et al. developed a UCNPs system targeting osteocytes that integrated zoledronic acid with pH-responsive plumbagin release for BC bone metastasis theranosis (Figure 17). The results showed that the NPs significantly reduced the expression of RANKL and sclerostin in MLOY-4 osteocytic cells and inhibited osteoclastogenesis induced by MLOY-4 cells. Additionally, the NPs markedly suppressed the proliferation, migration, and invasion of 4T1 and MDA-MB-231 cells, while promoting their apoptosis. Furthermore, the NPs enabled early detection of bone metastasis lesions via UCL and MRI. After 2 weeks of treatment, the bone volume/tissue volume ratio in the NPs group increased by 59.9% compared to the control group, and this ratio remained significantly higher after 4 weeks of treatment, demonstrating sustained therapeutic efficacy [320]. In 2017, Chowdhuri et al. developed FA-encapsulated nanoscale metal-organic frameworks on the surface of UCNPs, forming a core-shell drug delivery system. This system exhibited negligible toxicity toward TNBC cells and normal NIH3T3 cells, enabling efficient encapsulation of DOX. Notably, approximately 30% and 40% of DOX were released at pH 7.4 within 12 and 24 hours, respectively, whereas 65% and 72% of DOX were released at pH 5.5 over the same time periods, ensuring preferential drug delivery to cancer cells and minimizing damage to normal cells. The DOX-loaded NPs efficiently internalized into MDA-MB-468 cells via FR-mediated endocytosis, exhibiting enhanced cytotoxicity toward cancer cells compared to normal cells [222].

In addition to precise control over drug release, the unique optical properties of UCNPs enable real-time monitoring of the drug release process. For instance, Hu et al. developed a pH-responsive drug delivery nanosystem by functionalizing metal-phenolic networks onto mSiO<sub>2</sub>-coated UCNPs. Tannic acid and Cu<sup>2+</sup> coordination complexes were used to block DOX in the mesopores of UCNPs.

Loading DOX induced FRET from UCNPs to DOX, leading to quenching of luminescence for monitoring drug release. Results showed that the cumulative release of DOX reached 51.1% at pH 5.0 and only 3.2% at pH 7.4. When networks degraded in acidic environments to trigger DOX release, FRET was eliminated and luminescence was restored, enabling real-time monitoring of pH-triggered drug release in cells. This study provides an effective strategy for designing smart drug delivery systems with both pH-controlled release and release monitoring functions [321]. In another study, Wang et al. focused on the synergistic innovation of multiple responsive mechanisms, developing an NIR and pH dual-responsive drug delivery nanocomposite composed of UCNPs and a transformable poly(4,5-dimethoxy-2-nitrobenzyl methacrylate) shell layer. The nanocomposite exhibited a DOX loading efficiency of 7.23%, and the cumulative DOX release reached 59.5% within 300 minutes under the synergistic effect of pH 4.5 and 980 nm NIR light. The drug release kinetics were described by the Baker-Lonsdale model, confirming the dual-stimuli responsive release behavior and its potential for tumor-targeted therapy [322]. Similarly, the nanoplatfrom designed by Chen et al. leveraged dual-responsive properties and UCL to enable on-demand drug release and dynamic monitoring of the therapeutic process [323].

### 10.3. Other stimuli

Beyond light and pH stimuli, smart drug delivery systems based on UCNPs can leverage various other signaling cues to achieve precise control over drug release. Glutathione (GSH), a tripeptide composed of glutamate, cysteine, and glycine, serves as the primary reducing ligand in biochemical processes [324]. The concentration of GSH in the cytoplasm of tumor cells is higher than its extracellular concentration (ranging from 2 to 10 mmol/L compared to 2–20  $\mu\text{mol/L}$ ). Moreover, the GSH concentration in tumor tissues is at least four times higher than that in normal tissues [325]. This distinctive feature has spurred the development of diverse GSH-responsive UCNP-based delivery systems, primarily utilizing disulfide bond cleavage and thiol exchange reactions [326,327]. In the TME, GSH can also promote the biodegradation of Mn ions doped silica nanoshells, enabling GSH-responsive drug delivery. For instance, Xu et al. synthesized a Mn-doped mSiO<sub>2</sub> nanoshell as a drug carrier, which rapidly degrades in the reductive and mildly acidic TME. This degradation process occurs via the sequential cleavage of Mn-O and Si-O bonds, allowing for efficient delivery of DOX to the tumor site. Notably, the Mn<sup>2+</sup> released from the biodegradation process can enhance T<sub>1</sub>-weighted MRI contrast, providing diagnostic functionalities [328]. Another key characteristic of tumors is their elevated temperature, a consequence of enhanced aerobic glycolysis and rapid cell proliferation. Therefore, temperature-sensitive polymers have been widely applied to regulate the release of antitumor drugs via their structural alterations in response to the temperature fluctuations within tumor tissues [329,330]. Additionally, enzymes with specific high expression in tumor tissues can also serve as endogenous signals to trigger drug release [331].

## 11. Immunotherapy

Targeted immune system therapeutic strategies, including chimeric antigen receptor T-cell therapy, immune checkpoint blockade therapy, neoantigen vaccines, and small-molecule modulators, have emerged as highly effective approaches for treating various cancers [332,333]. However, their clinical efficacy remains generally limited, benefiting only a minority of patients. Issues such as extensive adverse reactions, lack of reliable biomarkers, tumor recurrence, drug resistance, and metastasis also restrict broader clinical application. UCNP-based immunotherapeutic strategies offer significant advantages, enabling precise targeting, local drug release, combination with other therapies to enhance efficacy, and inherent imaging capabilities. Table 9 summarizes UCNPs combined with immunotherapy.

Dendritic cells (DCs) are central to initiating and regulating innate and adaptive immunity within the TME. They exhibit remarkable competence in antigen uptake, processing, and presentation. DCs differentiate into mature form upon antigen exposure and migrate to lymph nodes to activate T cells. This process is critical for DC vaccine efficacy [334]. Conventional imaging methodologies cannot enable real-time visualization of DC migration dynamics. In 2015, Xiang et al. developed antigen-loaded UCNPs for DC stimulation, tracking, and vaccination (Figure 18A). They showed that dual-polymer-coated UCNPs efficiently delivered antigens into DCs through endocytosis, induced DC maturation and cytokine release, and enabled highly sensitive *in vivo* UCL imaging to track DC migration to draining lymph nodes, achieving a detection limit as low as 50 cells in mice. Notably, the UCNPs-pulsed DC vaccine elicited robust antigen-specific immune responses, including enhanced T cell proliferation, interferon- $\gamma$  secretion, and cytotoxic T lymphocyte mediated cytotoxicity against tumor cells. These findings highlight the potential of UCNP-based DC vaccines for effective cancer immunotherapy [335].

Immunogenic cell death (ICD), which can be induced by various antitumor therapies, prompts the release of danger associated molecular patterns and tumor-associated antigens. This process facilitates the maturation of DCs and infiltration of cytotoxic T lymphocytes, thereby reversing the tumor immunosuppressive microenvironment and enhancing sensitivity to immunotherapy [336]. Notably, UCNP-based drug delivery systems are being explored for inducing ICD through chemotherapy, PDT, and PTT, enabling multifunctional therapeutic integration. For example, Lin's team prepared mSiO<sub>2</sub>-coated UCNPs with large pores, loaded with PS MC540 and tumor antigens. Under 980 nm light irradiation, the nanocomposites mediated PDT via UCL, generating ROS to induce tumor cell death. Simultaneously, released antigens activated DCs, triggering robust Th1/Th2 immune responses. This was evidenced by increased cytokine secretion and elevated frequencies of CD4<sup>+</sup>, CD8<sup>+</sup> and effector-memory T cells. In tumor-bearing mice, the nanovaccines showed synergistic therapeutic effects, more potently inhibiting tumor growth and prolonging survival than single PDT or immunotherapy [337]. Jin et al. developed a nanocarrier system where UCNPs were coated with sialic acid-modified micelles and loaded with DOX

and PS RB. This system enabled synergistic chemo-photodynamic therapy that induced ICD, evidenced by increased cell surface calreticulin exposure, extracellular ATP release, and high mobility group protein B1 secretion. In 4T1 tumor-bearing mice, the nanocarrier combined with NIR light promoted intratumoral infiltration of CD8<sup>+</sup>/CD4<sup>+</sup> T cells, elevated anti-tumor cytokine levels, and inhibited tumor growth and lung metastasis [338]. Another study reported that biodegradable K<sub>3</sub>ZrF<sub>7</sub>:Yb,Er NPs dissolved in cancer cells to release substantial K<sup>+</sup> and [ZrF<sub>7</sub>]<sup>3-</sup>, triggering a surge in intracellular osmolarity and homeostasis imbalance. This further induced increased ROS, caspase-1 activation, gasdermin D cleavage, and interleukin-1 $\beta$  maturation. In vivo experiments confirmed these UCNPs enhanced DC maturation and effector memory T cell frequency, significantly inhibiting TNBC growth and pulmonary metastasis [339].

To enhance the immune response of immunotherapy, UCNPs are frequently integrated with immune adjuvants or immune checkpoint inhibitors [340–344]. For instance, Wang et al. designed a nanoplatfrom by self-assembling PEG and indocyanine green onto UCNPs followed by loading RB, applying it to NIR-triggered photothermal, photodynamic, and immunotherapy for metastatic TNBC (Figure 18B). The nanoplatfrom effectively destroyed primary tumors and inhibited untreated distant tumors. When combined with anti-cytotoxic T-lymphocyte-associated protein 4 (CTLA-4) antibody, it enabled approximately 84% of treated tumor-bearing mice to achieve long-term survival and 34% to develop tumor-specific immunity, offering a promising approach for metastatic cancer treatment [345]. Similarly, Liu et al. developed UCNPs-PEG nanocomposites for co-delivering PS and the immune adjuvant imiquimod (R837). Under NIR irradiation, the effective photodynamic destruction of tumors generated tumor-associated antigens. These antigens promoted strong antitumor immune responses in the presence of the R837-containing NPs acting as adjuvant. Furthermore, combining nanocomposite-mediated PDT with CTLA-4 checkpoint blockade exhibited remarkable efficacy. This strategy not only eradicated NIR-exposed tumors but also induced strong systemic antitumor immunity, inhibiting growth of distant tumors [346]. In another study, Lin et al. designed a TME-activated UCNP-based enzymatic cascade nanocatalyst. This system enabled synergistic starvation/chemodynamic/immunotherapy by amplifying ROS generation, reversed the immunosuppressive TME, and allowed real-time therapeutic monitoring via UCL [347].

## **12. Clinical translation of UCNPs**

The theranostic platforms based on UCNPs offer a promising approach in BC management. By integrating diagnostic imaging and therapeutic functions, these platforms address the limitations of conventional methods. Their ability to enable deep tissue penetration, combined with the strategic integration of MRI, PET, and CT-compatible components, facilitates multimodal imaging. Meanwhile, these nanoplatfroms demonstrate robust drug/gene delivery capabilities, supporting chemotherapeutic, gene, photodynamic, photothermal, and immunotherapeutic

strategies. Stimuli-responsive release mechanisms further enhance spatiotemporal payload delivery precision, maximizing therapeutic efficacy while minimizing off-target toxicity. Crucially, modular functional design on a single NP enables personalized theranostic systems. However, no UCNP-based products are yet approved for clinical use, with most studies confined to in vitro cell studies or animal models. This clinical translation lag stems from insufficient integration of UCNP basic research with translational applications, alongside common nanomedicine translation challenges. This section reviews UCNP clinical translation aspects, discusses challenges and solutions, and outlines future directions.

### 12.1 Design and fabrication of UCNPs

The biomedical application of UCNP exemplifies a compelling interdisciplinary field. Over the past two decades, a critical disparity has emerged: while most nanomaterial researchers hold academic backgrounds in chemistry or physics, they often lack specialized expertise in pharmacy and medicine. This knowledge gap contributes to a growing disconnect between research objectives and material design. Specifically, UCNP have been extensively studied for uses such as molecular detection, in vivo imaging, drug delivery, and cancer therapy. Yet, researchers have disproportionately focused on developing novel NP designs. This focus often overlooks crucial questions about how and when nanoplatforms interact with tumors and the underlying reasons for preclinical trial failures. This trend is evident in the thousands of publications detailing UCNP synthesis, modification, and evaluations in vitro or animal models. Most prioritize material development and preliminary efficacy validation, placing limited emphasis on comprehensive safety, quality control, and thorough efficacy assessment. For example, a survey by the European Upconversion Network (COST Action CM1403) found that only 18% of 1,811 biomedical UCNP studies included toxicity or safety evaluations [155]. Systematic preclinical pharmacokinetic/pharmacodynamic analysis and molecular mechanism exploration were even rarer. Consequently, this interdisciplinary imbalance leaves numerous "candidate materials" without the critical data needed for clinical translation. To prevent this disconnection between design intent and practical utility, future UCNP design must integrate interdisciplinary collaboration and prioritize genuine clinical needs from the outset.

UCNP and their functionalized derivatives show significant potential for diagnostic and therapeutic applications. However, knowledge gaps exist about their complex biological interactions, demanding an application-tailored design approach. As regulatory agencies evaluate nanomedicines individually, reflecting the absence of universal design standards, validation should align closely with specific application requirements. For diagnostic UCNP, achieving rapid in vivo clearance is crucial to minimize biological burden. This often leads researchers to employ degradable materials or reduce particle size for efficient renal or hepatic excretion. While smaller nanocrystal sizes facilitate clearance, they typically compromise quantum efficiency. Conversely, therapeutic UCNP frequently require prolonged tumor retention,



addressed through surface modifications extending circulation time and enhancing active targeting. For cancer imaging and therapy, intravenous administration of UCNPs under 500 nm is generally preferred, optimizing targeting while preventing vascular obstruction and reducing clearance via the mononuclear phagocyte system. Some studies indicate arterial administration can bypass hepatic filtration, increasing tumor accumulation. For lymph node tracing, subcutaneous injection of negatively charged particles in the 10–100 nm range proves optimal. Particles with this size and charge exhibit weak interactions with blood and lymph components while facing reduced interstitial transport barriers. Moreover, while a positive zeta potential facilitates gene loading, excessively high positive charge density can result in increased cytotoxicity. In summary, UCNP design is fundamentally application-specific, with no single paradigm suiting all purposes. Each application necessitates rigorous, case-by-case validation of its customized parameters. Although this context-dependency complicates standardization, it highlights the scientific rigor essential for successful clinical translation.

Scaling nanodrug production from lab batches to industrial manufacturing presents a major challenge in nanomedicine development, requiring good manufacturing practice (GMP)-compliant synthesis to ensure safety and efficacy. Engineered UCNPs face poor reproducibility and significant scale-up hurdles due to their complex compositions and multi-step syntheses. These difficulties are further compounded by the absence of standardized GMP frameworks for inorganic NPs. Addressing these issues requires two essential strategies. First, developing more efficient fabrication processes involves optimizing synthesis parameters like temperature and pressure control validated for GMP environments alongside automated production systems. This enhances process control ensuring each manufacturing step meets GMP-compliant protocols. Second, establishing unified quality standards necessitates standardized testing protocols including GMP-aligned in-process analytics and post-synthesis characterization. This ensures product consistency by integrating critical quality attributes into the manufacturing pipeline.

## 12.2 Targeting for metastases

Patients with BC typically die from metastases rather than primary tumors. However, most existing studies utilize subcutaneously implanted primary tumors. These models grow in isolation with less than 20–30% of the tumor surface contacting non-cutaneous host tissues, inadequately representing real metastatic disease where lesions spread to distant sites like lymph nodes, brain, bone, and lung. Therefore, recapitulating BC's natural behavior using syngeneic mouse models or genetically engineered models is essential for research targeting metastatic foci. For example, the 4T1 model in BALB/c mice, when properly induced through spontaneous metastasis from orthotopic or subcutaneous inoculation sites not via tail vein injection, establishes reliable metastatic models that authentically recapitulate natural dissemination and colonization processes within murine systems. Notably, current UCNP-based lymph node targeting primarily relies on lymphatic drainage and

BC-related targets. However, recent research demonstrates that leveraging receptors on antigen-presenting cells or addressins on high endothelial venules represents powerful targeting approaches for lymph nodes [348]. Advanced BC brain metastasis often causes severe outcomes. The blood-brain barrier, composed of brain microvascular endothelial cells, restricts most systemically administered therapeutics from entering brain parenchyma, hindering effective brain tumor treatment. For instance, trastuzumab, a HER2-targeted antibody, shows limited efficacy against BC brain metastases due to poor blood-brain barrier permeability. Owing to their nanoscale size and structural modifiability, UCNPs emerge as promising candidates for crossing the blood-brain barrier and enabling targeted brain tumor therapy [349].

### 12.3 Diagnosis for BC

UCNPs offer distinct advantages for BC molecular imaging, lymph node tracing, and tumor marker detection, including large anti-Stokes shifts, photobleaching resistance, and low background fluorescence, yet face significant challenges. To achieve high quantum yield, Yb<sup>3+</sup>-sensitized UCNPs excited by 980 nm light are widely used. However, this approach encounters two primary obstacles. Primarily, biological tissues strongly absorb 980 nm light through water and melanin, attenuating excitation intensity during penetration and reducing efficiency. Secondly, continuous 980 nm irradiation causes tissue overheating, potentially damaging healthy cells. Alternative Nd<sup>3+</sup>-sensitized UCNPs excitable at 808 nm present promising solutions to these limitations [350]. Additionally, UCNPs exhibit low nonlinearity with orders of 4-5, challenging super-resolution microscopy below 100 nm. Enhancing strategies include utilizing photon avalanche mechanisms, optimizing ion doping, refining core-shell structures, and engineering energy migration pathways [351].

Despite multimodal imaging capabilities, UCNP platforms face persistent technical hurdles. Physical interferences between imaging modes, particularly energy transfer conflicts between luminescent cores and surface conjugates, compromise signal fidelity and resolution. Addressing this requires smart nanoplatform engineering with computational model-guided energy optimization and interfacial isolation. Furthermore, disparities in signal intensity and resolution across modalities hinder accurate image registration and fusion, limiting diagnostic value. Clinically, multimodal imaging suits patient stratification but requires dedicated equipment per modality. Mechanically integrating spatiotemporally disparate results often fails to achieve complementary information while adding noise. Additionally, the prolonged blood circulation of UCNPs necessitates delayed scanning protocols, typically conducted several days post-injection. This temporal lag not only complicates patient logistics but also reduces clinical feasibility by increasing the risk of inter-scan variability and prolonging diagnostic workflows.

Current UCNP-based biosensors primarily target circulating tumor biomarkers, with less emphasis on tissue specimens. Due to the transient and fluctuating nature of circulating biomarkers in non-malignant conditions, diagnostic outcomes relying on

them are often ambiguous. In contrast, tissue biopsy combined with IHC for molecular subtyping remains the gold standard in BC diagnosis. Studies show nanoprobe-spectral analysis improves detection accuracy for low-expression targets compared to IHC alone, addressing biomarker ambiguity. Significantly, as HER2-low BC gains focus for targeted therapy, the semi-quantitative nature of IHC leads to poor consistency in HER2 evaluation. Quantitative fluorescence intensity measurement via UCNP probes offers a solution. Additionally, clinical tissue sections are typically several micrometers thick. Excessively thick sections obscure cellular structures, while overly thin sections increase workload and missed diagnosis risk [352]. Leveraging NIR lasers with deep tissue penetration for excitation, UCNPs could potentially enable compatibility with thicker sections.

#### 12.4 Treatment for BC

UCNP-based phototherapy holds notable potential for BC treatment but faces critical limitations. NIR light penetration depth is limited to several millimeters. For instance, in human breast tissue, 835 nm NIR light penetrates about 3.54 mm, in adipose tissue about 2.79 mm, and in cancer tissue about 4.23 mm [13]. Consequently, low-power NIR light cannot effectively reach deep-seated tumors, reducing therapeutic efficacy. Additionally, UCNPs suffer from inherently low upconversion efficiency. They generate insufficient excitation energy under low laser power, while high-power lasers risk photodamage to biological tissues. Specifically, prominent NIR-to-visible upconversion efficiencies for UCNPs are around 5% for irradiances below 100 W/cm<sup>2</sup> [353]. Most UCNP-based phototherapy applications require relatively high laser powers (1–4 W/cm<sup>2</sup>), far exceeding the American National Standards Institute safe thresholds of 330–350 mW/cm<sup>2</sup> at 808/980 nm and 420 mW/cm<sup>2</sup> at 1064 nm [276]. Higher laser power is thus unsuitable for clinical use due to severe photodamage risks. To tackle these challenges, strategies aim to boost upconversion efficiency within safe laser limits and enhance light penetration. For example, dye-sensitized organic-inorganic hybrid systems show upconversion quantum yields up to 9.8% even in sub-optimized configurations [354]. Another approach leverages the second near-infrared window (NIR-II, 1000–1700 nm), offering deeper penetration and higher permissible exposures. Precision core-shell structure design also promises improved efficiency. Moreover, as mentioned earlier, combining phototherapy with other treatments such as chemotherapy, immunotherapy, and radiotherapy can synergistically enhance efficacy. Furthermore, existing UCNP-based PTT overlooks peritumoral heat accumulation, risking damage to normal tissues. Exploring strategies for real-time thermal feedback and mild PTT is therefore necessary to ensure safety [355].

Current drug delivery platforms primarily focus on single chemotherapy agents. Co-delivering multiple anti-BC therapeutics could enhance efficacy and combat resistance. Additionally, using UCNPs to visualize drug release can improve precision. For instance, one study used NaYF<sub>4</sub>:Yb,Tm NPs as optical probes to monitor DOX release, correlating luminescence attenuation with drug dissociation [356]. Moreover,

upconversion superballs loaded with the PS ZnPc and superoxide dismutase 1 siRNA via mSiO<sub>2</sub> coating enabled spatiotemporally controlled release of therapeutics and genes under 808/980 nm light irradiation, setting a paradigm for co-delivery of multiple therapeutics and real-time visualization [357]. Recently, intraductal drug delivery strategies for BC, which involve administering drugs through mammary ducts, have garnered significant attention. This approach enables minimally invasive drug distribution via the ductal tree. Nanosystem-based delivery can maximize its advantages by prolonging tissue retention, enhancing targeting, improving cytotoxicity, and reducing dosing frequency [358]. In the foreseeable future, leveraging their superior optical properties, UCNP-based intraductal strategies could overcome challenges like duct identification and catheterization, enabling precise local therapy. Despite the rising trend in gene therapy, UCNP-based gene therapy research remains limited. Structural optimization based on payload-specific design is crucial. For instance, cationic polymer coatings protect nucleic acids during transport, biomimetic surface modifications enable stable conjugation of proteins and antibodies, and mesoporous structures enhance encapsulation of hydrophobic compounds [359]. Spatiotemporal control of release kinetics is vital, especially for gene editing tools requiring cytosolic delivery. Ideally, such systems promptly release cargo upon entering the cytosol, minimizing delays and ensuring high-efficiency editing. Moreover, optimizing delivery vehicle design to enhance biocompatibility and reduce off-target effects is also crucial for safe gene editing application.

## 12.5 Systematic assessment

The systematic evaluation of engineered UCNPs requires a full-process assessment of quality, safety, and efficacy, which necessitates integrating multi-dimensional characterization technologies and interdisciplinary research frameworks. Traditional quality evaluation methods for UCNPs, including dynamic light scattering, transmission electron microscopy, X-ray diffraction, and fluorescence spectroscopy, primarily characterize physicochemical parameters post-synthesis and pre-application. However, given the complex nano-bio interactions, in vivo quality assessment of UCNPs is critical. Tracking structural evolution trajectories across diverse physiological and pathological stages to establish spatio-temporal correlations between structural parameters and biological effects can reveal nanomaterial dynamics in vivo. For example, fluorescence spectral analysis enables real-time monitoring of luminescence stability and spectral shifts, clarifying how anti-Stokes emission properties are influenced by protein corona formation or microenvironmental pH fluctuations.

Structure-activity relationships (SARs), which define the inherent correlation between molecular structures and biological outcomes (e.g., efficacy and toxicity), form the theoretical foundation for drug design, optimization, and mechanism elucidation. Establishing clear SARs for UCNPs remains challenging due to their multi-scale complexity, synergistic multi-factor influences, and interference from dynamic in vivo environments. This complicates biological effect prediction, quality control,

mechanistic analysis, and material optimization. Specifically, the structures of UCNPs encompass not only molecular-level chemical compositions but also nanoscale physical properties (e.g., size, morphology, and surface charge). The biological effects of UCNPs arise from the combined action of multiple structural factors, making it difficult to disentangle the influence of a single component. Notably, once UCNPs enter the body, they undergo dynamic interactions with blood proteins, cell membranes, and tissue microenvironments. Their "actual structure" (e.g., the composition of the surface protein corona) may differ significantly from the as-designed structure, further blurring the correlation between the original structure and biological effects.

While most studies claim acceptable toxicity for engineered UCNPs, many lack dedicated toxicity evaluations and comprehensive characterization of key parameters, including spatio-temporal biodistribution, long-term accumulation kinetics, and transgenerational effects. Similar to other inorganic nanomaterials, most UCNPs are non-biodegradable, with only partially sized and charged NPs excreted via hepatorenal pathways [281]. Prolonged retention in the mononuclear phagocyte system may pose risks. Future efforts should prioritize developing biodegradable UCNPs and balancing functional durability with controllable *in vivo* clearance through surface modification and biomimetic strategies. Notably, quantitative nanomaterial risk assessment remains infeasible due to absent standardized, validated methods for defining human or environmental exposure limits.

Current safety and efficacy evaluations rely predominantly on cell lines and rodent models, which suffer from translational limitations due to species-specific differences in metabolism, immunity, and barrier structures. Shifting to non-human primate models can mitigate such discrepancies. Additionally, integrating patient-derived xenografts and biomimetic *in vitro* 3D tumor models (e.g., tumor organoids) maximizes recapitulation of human BC heterogeneity and *in vivo* microenvironments [360]. To demonstrate superior clinical efficacy or safety, large-scale, long-term clinical trials are essential. Identifying endpoints that meaningfully reflect patient benefits, such as improved long-term remission, delayed disease progression, or reduction of side effects, is critical for ensuring new nanomedicine products show sufficient clinical potential in pivotal trials. Tightening inclusion criteria to reduce patient variability in study protocols can downsize trial scales, though this introduces challenges like slower enrollment and narrower patient representation. One solution is using biomarkers to predict treatment responses, which diminishes variability impacts while failing to address enrollment delays.

## 12.6 Regulatory requirements of nanomaterials

The rapid advancement of nanotechnology in pharmaceuticals, cosmetics, and other sectors has outpaced the update of regulatory frameworks. The unique properties of nanomaterials render traditional regulatory standards for bulk materials inapplicable to them. For instance, gold nanoclusters exhibit catalytic activity, whereas bulk gold is

inert. Additionally, controversies exist regarding the size-dependent toxicity of ZnO NPs toward crustaceans. These disparities make assessment systems based on bulk materials unable to accurately predict the biological effects of nanomaterials, thereby giving rise to challenges such as the inapplicability of safety and efficacy data and the fragmentation of global classification standards.

In response to these challenges, major countries and regions have adopted distinct regulatory strategies. For example, the European Medicines Agency applies general pharmaceutical legislation to nanomedicines and references the European Commission's 2011 recommendations on nanomaterials. However, these recommendations lack legal binding force and have not been uniformly implemented across the European Union [361]. The FDA employs a "case-by-case approval" model, issuing the Drug Products, Including Biological Products, That Contain Nanomaterials Guidance for Industry in 2017 and the Liposome Drug Products Chemistry, Manufacturing, and Controls Human Pharmacokinetics and Bioavailability and Labelling Documentation Guidance for Industry in 2018. These guidelines emphasize the evaluation of physicochemical properties and pharmacokinetics of nanomedicines [362]. The Medicines and Healthcare products Regulatory Authority of the United Kingdom currently lacks specific legislation for nanotechnology products, relying instead on laws of the European Union and domestic health and safety regulations.

Furthermore, international organizations are actively promoting regulatory coordination. The International Organization for Standardization has issued standards defining core terms in nanotechnology. The Organization for Economic Co-operation and Development has advanced the international harmonization of safety testing methods for nanomaterials. The International Council for Harmonization of Technical Requirements for Pharmaceuticals for Human Use has facilitated the exchange of regulatory science in nanomedicines through the International Pharmaceutical Regulators Programme. Adjustments to nanomaterial regulation must balance innovation and safety, gradually constructing a regulatory framework adapted to the characteristics of nanotechnology through international standard-setting, regional regulatory coordination, and interdisciplinary research. Future efforts should further strengthen global collaboration to address the complex challenges posed by nanomaterials in medicine, the environment, and other domains.

### 12.7 Clinical translation roadmap

Similar to other nanomedicines, the clinical translation of UCNPs should always be regarded as the ultimate development goal. Traditionally, the development and translation of cancer nanomedicines have adopted a bottom-up approach, starting from the design, manufacturing, and controls of nanoplateforms. However, in terms of feasibility, efficiency, and industrialization, a top-down approach is considered a wiser and more valuable strategy. This approach begins with an assessment of commercial potential, followed by an evaluation of clinical feasibility, and finally progresses to

drug design, production, and quality control (Figure 19) [363].

Specifically, the first hurdle in developing any nanomedicine is evaluating its commercial viability, which hinges on the potential to improve patient outcomes and the size of the target patient population. Compared to benchmark products, UCNPs formulations must offer advantages such as reduced dosing frequency, more convenient administration routes, improved therapeutic efficacy, reduced toxicity, or augmented patient benefits. The more pronounced these advantages, the easier it is to justify price premiums once the product enters the market. This requires an end-user perspective to identify products and trajectories with genuine clinical and commercial potential.

Concurrently, preclinical efficacy experiments must be meticulously planned, employing appropriate models to simulate human cancer progression for accurate evaluation of the antitumor activity of UCNPs. Toxicology studies should proceed in parallel, comprehensively investigating short-term acute toxicity, long-term chronic toxicity, and potential toxic effects on major organs. During experimental design, proactively focusing on critical issues likely to emerge in clinical development is essential, such as the predictability and controllability of UCNPs in their distribution, metabolism, and excretion, as well as uncertainties regarding immune response risks or unexpected tissue damage. In-depth research and data accumulation enable early identification and resolution of these issues, paving the way for subsequent clinical trials and ensuring high success rates and safety when UCNPs enter human testing.

In the drug design phase, considerations must extend beyond therapeutic efficacy to include formulation stability and manufacturability. The selection of nanomaterials and drug loading strategies requires iterative optimization to ensure stability during storage and transportation, as well as precise in vivo release. Strict standard operating procedures must be established during production to ensure each batch of UCNPs is manufactured according to predefined design criteria, guaranteeing quality consistency. Quality control systems should cover the entire process from raw material procurement to finished product testing, employing advanced analytical techniques and equipment to strictly monitor critical quality attributes, ensuring that product safety and efficacy meet clinical requirements.

In summary, top-down analysis identifies the most critical issues in the clinical translation process from the outset, triggering proactive thinking and planning to overcome potential challenges at early stages. This approach aligns with the interdisciplinary strategies emphasized by the European Upconversion Network (COST Action CM1403), focusing on key aspects such as nanotoxicity research, surface functionalization, and instrumentation development to ensure safety while maximizing clinical value in cancer theranostics [155].

### **13. Conclusion**

Engineered UCNPs have garnered significant attention in the field of BC diagnosis and therapy due to their unique optical properties, excellent biocompatibility, and flexible design. These NPs not only serve as highly efficient imaging probes but also enable highly selective and smart therapeutic strategies. Current preclinical studies, including both in vitro cellular experiments and tumor animal models, have demonstrated the outstanding theranostic efficacy of these materials. However, the translational process from laboratory research to clinical application faces numerous challenges at the scientific, technical and regulatory levels. In the future, efforts should focus on optimizing the synthesis, functionalization, and clinical translation of UCNPs. Meanwhile, promoting collaborative and multidisciplinary approaches will help break through the limits of possibility, paving the way for UCNPs to play a core role in the theranostics of BC.

### **Declaration of competing interest**

The authors declare that they have no known competing financial interests or personal relationships that could have appeared to influence the work reported in this paper.

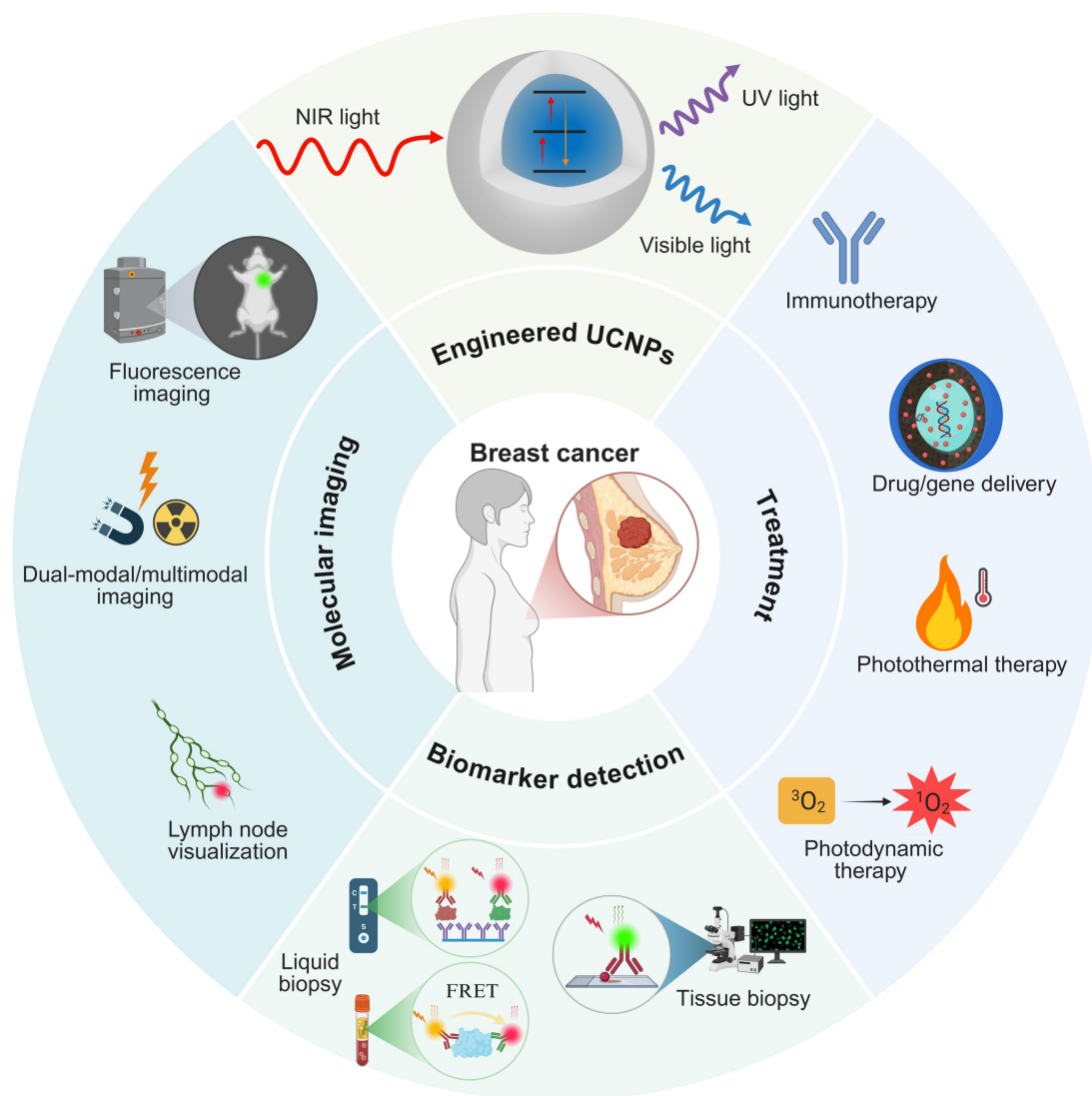
### **Acknowledgements**

This work is supported by National Natural Science Foundation of China (Grant Nos. 12374413, 62175025, U2441222), the Young Top Talents of Liaoning Province Xingliao Talent Plan (XLYC2203170), Science and Technique Foundation of Liaoning Province (2024JH3/50100028), Wu Jieping Medical Foundation (320.6750.2020-20-15), and the Outstanding Young Scientific and Technological Talents of Dalian (Grant No. 2021RJ07).

### **Data availability**

No data was used for the research described in the article.





**Graphical abstract**

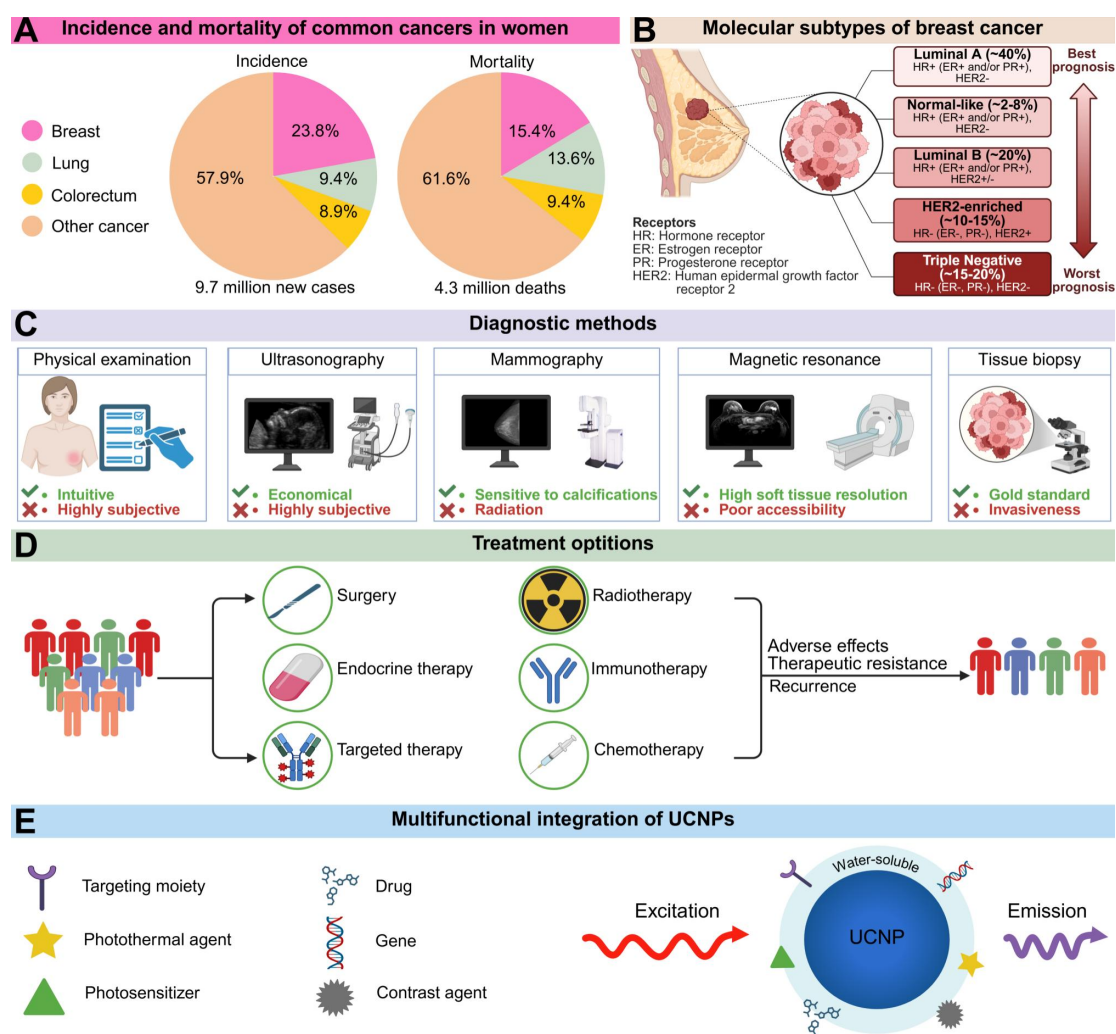


Figure 1. (A) Pie charts show the distribution of cases and deaths among the three top cancers affecting females in 2022. The size of each segment precisely reflects the proportion of the total number of cases or deaths. (B) Molecular subtypes of BC. Clinical status of strategies for BC diagnosis (C) and treatment (D). (E) Different types of UCNP-based designs for strategies in the diagnosis and treatment of cancer. Created with BioRender.com.

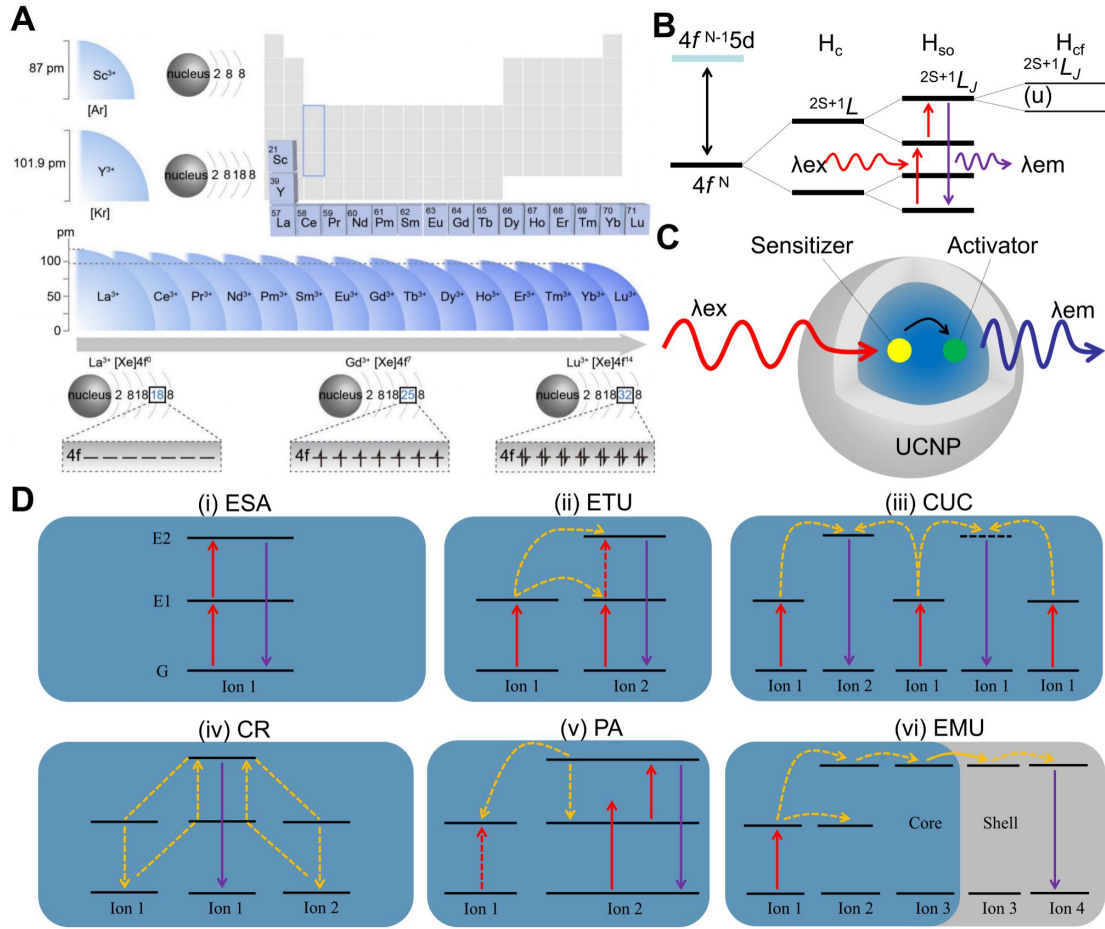


Figure 2. (A) Ionic radius and valence configuration of RE. From  $\text{La}^{3+}$  to  $\text{Lu}^{3+}$ , the number of electrons on the 4f orbitals increases with increasing atomic number. The electron configurations of  $\text{La}^{3+}$ ,  $\text{Gd}^{3+}$ , and  $\text{Lu}^{3+}$  show empty, half-filled, and completely filled 4f orbitals, respectively. Adapted with permission from [21], copyright 2022, American Chemical Society. (B) Simplified energy level diagrams of lanthanide ions for a basic upconversion process. The  $4f^N$  configuration of lanthanide ions splits into multiple energy sublevels due to the effects of the coulombic ( $H_c$ ), spin-orbit ( $H_{so}$ ) and crystal-field ( $H_{cf}$ ) interactions. The energy levels are denoted as  $2S+1L_J$ , where  $S$ ,  $L$ , and  $J$  stand for total spin, orbital, and total angular momentum quantum numbers. (C) Schematic illustrations for UCNPs and the typical energy transfer process. (D) Schematic diagrams of six upconversion processes. Created with BioRender.com.

$\lambda_{ex}$ : excitation spectrum;  $\lambda_{em}$ : emission spectrum; ESA: excited state absorption; ETU: energy transfer upconversion; CUC: cooperative upconversion; CR: cross-relaxation; PA: photon avalanche; EMU: energy migration upconversion.

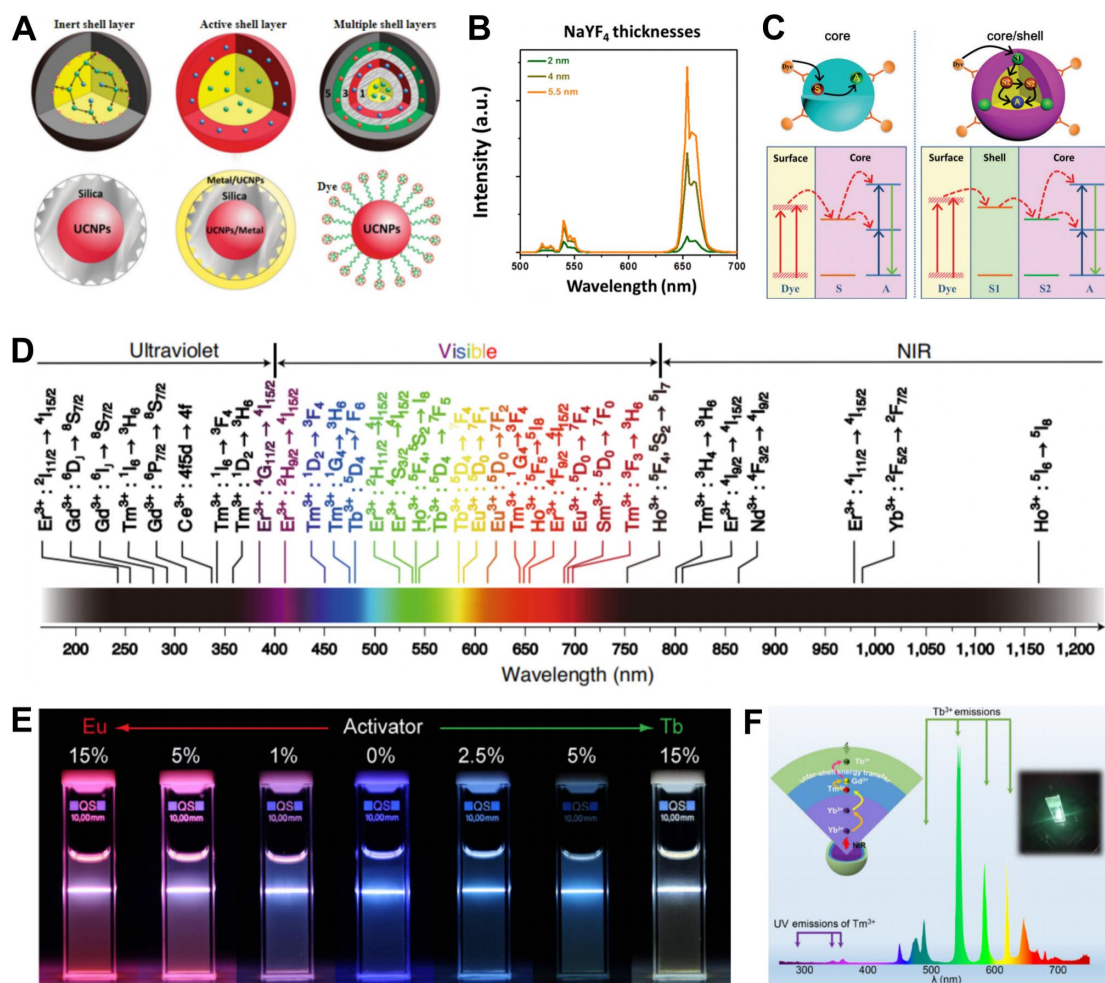


Figure 3. (A) Schematic diagram of the core-shell structures. Adapted with permission from [49], copyright 2015, Royal Society of Chemistry. (B) The shell-thicknesses dependent upconversion emission spectra of NaErF<sub>4</sub>@NaYF<sub>4</sub> NPs. Reproduced with permission [52], copyright 2021, under a Creative Commons CC BY license. (C) Schematic illustrations of dye sensitized upconversion in the core (S, sensitizer; A, activator) (left) and the core-shell structure (right). Adapted with permission from [55], copyright 2021, American Chemical Society. (D) A summary of the upconversion transitions of RE ion, covering a broad range of wavelengths from the UV to the NIR. Created with BioRender.com. (E) UCL of core-shell NPs with different Eu<sup>3+</sup>/Tb<sup>3+</sup> doping concentrations under 980 nm excitation. Adapted with permission from [57], copyright 2011, Springer Nature Limited. (F) Schematic illustration of the sandwich core-shell nanostructure. Adapted with permission from [59], copyright 2021, Chinese Chemical Society.



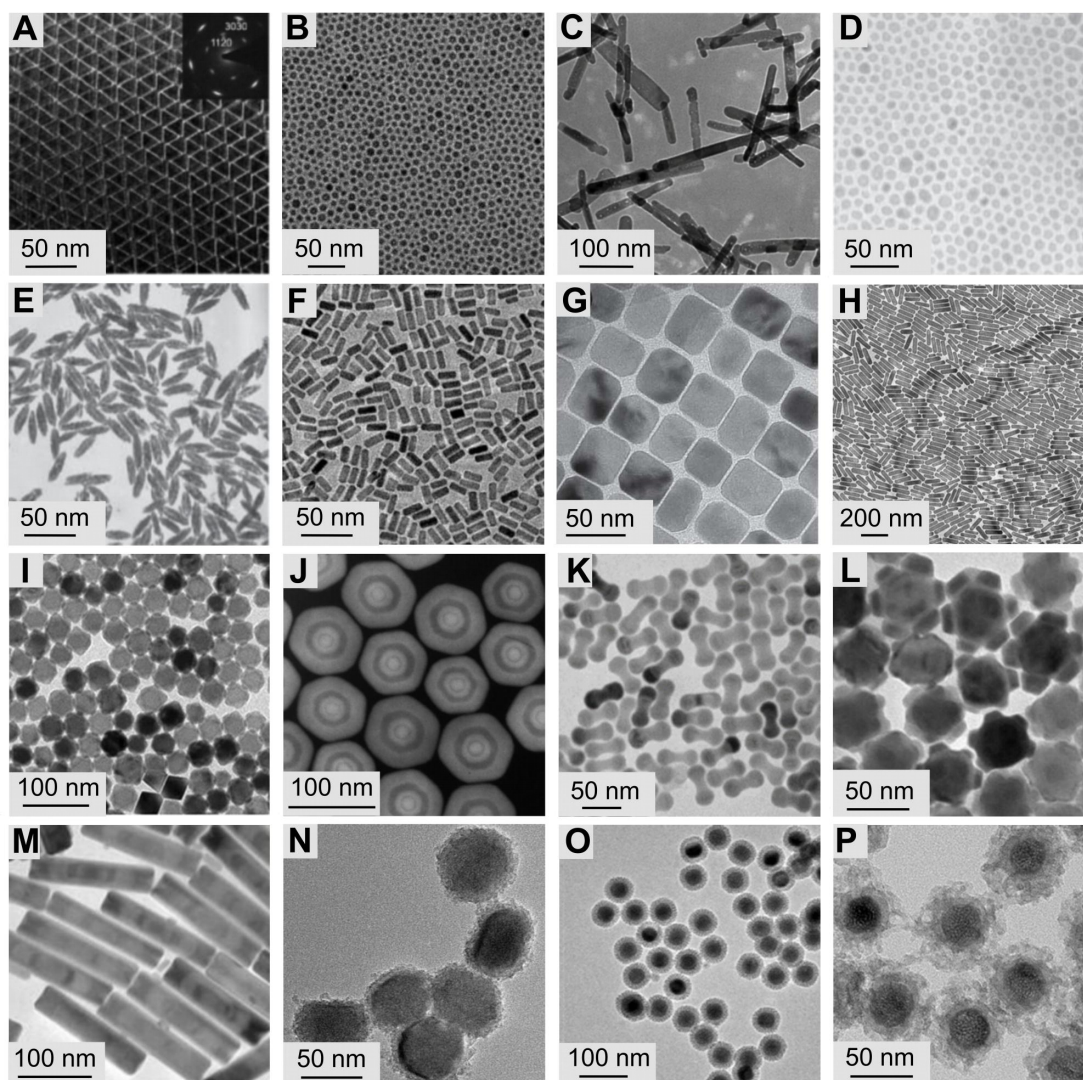


Figure 4. Typical transmission electron microscope images of UCNPs. (A)  $\text{LaF}_3$  (Adapted with permission from [61], copyright 2005, American Chemical Society), (B)  $\text{NaYF}_4$  (Adapted with permission from [62], copyright 2006, WILEY-VCH Verlag GmbH & Co. KGaA, Weinheim) and (C)  $\text{Gd}_2\text{O}_3$  (Adapted with permission from [66], copyright 2012, Elsevier Ltd. All rights reserved) NPs synthesized by thermal decomposition. (D)  $\text{NaYF}_4$  (Adapted with permission from [73], copyright 2005, Springer Nature Limited), (E)  $\text{YF}_3$  (Adapted with permission from [73], copyright 2005, Springer Nature Limited), and (F)  $\text{NaGdF}_4$  (Adapted with permission from [72], copyright 2016, American Chemical Society) nanocrystals synthesized by hydrothermal/solvothermal strategy. (G)  $\text{NaScF}_4$  (Adapted with permission from [76], copyright 2013, Royal Society of Chemistry) and (H)  $\text{KYb}_2\text{F}_7$  (Adapted with permission from [77], copyright 2013, Springer Nature Limited) nanocrystals synthesized by coprecipitation. (I)  $\text{LiLuF}_4@\text{LiLuF}_4$  (Adapted with permission from [81], copyright 2014, WILEY-VCH Verlag GmbH & Co. KGaA, Weinheim) NPs synthesized by seed-mediated heat-up. (J)  $\text{GdF}_4@\text{NaYF}_4@\text{NaGdF}_4@\text{NaYF}_4@\text{NaGdF}_4$  (Adapted with permission from [83], copyright 2016, WILEY-VCH Verlag GmbH & Co. KGaA, Weinheim) nanocrystals

synthesized by successive layer-by-layer method. (K)  $\text{NaGdF}_4@\text{NaYF}_4$  nano-dumbbells, (L)  $\text{NaYF}_4@\text{NaGdF}_4@\text{NaNdF}_4$  flower-shaped nanocrystals, (M)  $\text{NaYF}_4@\text{NaGdF}_4$  bamboo-like nanorods (Adapted with permission from [65], copyright 2016, under a Creative Commons CC BY license). (N)  $\text{NaYF}_4@\text{TiO}_2$  (Adapted with permission from [89], copyright 2020, Elsevier Ltd. All rights reserved), (O)  $\text{NaYF}_4@\text{NaYF}_4@\text{SiO}_2$  (Adapted with permission from [87], copyright 2020, The Society of Powder Technology Japan. Published by Elsevier B.V. and The Society of Powder Technology Japan. All rights reserved), and (P)  $\text{NaYF}_4@m\text{SiO}_2$  (Adapted with permission from [86], copyright 2022, American Chemical Society) NPs synthesized by nonepitaxial growth.

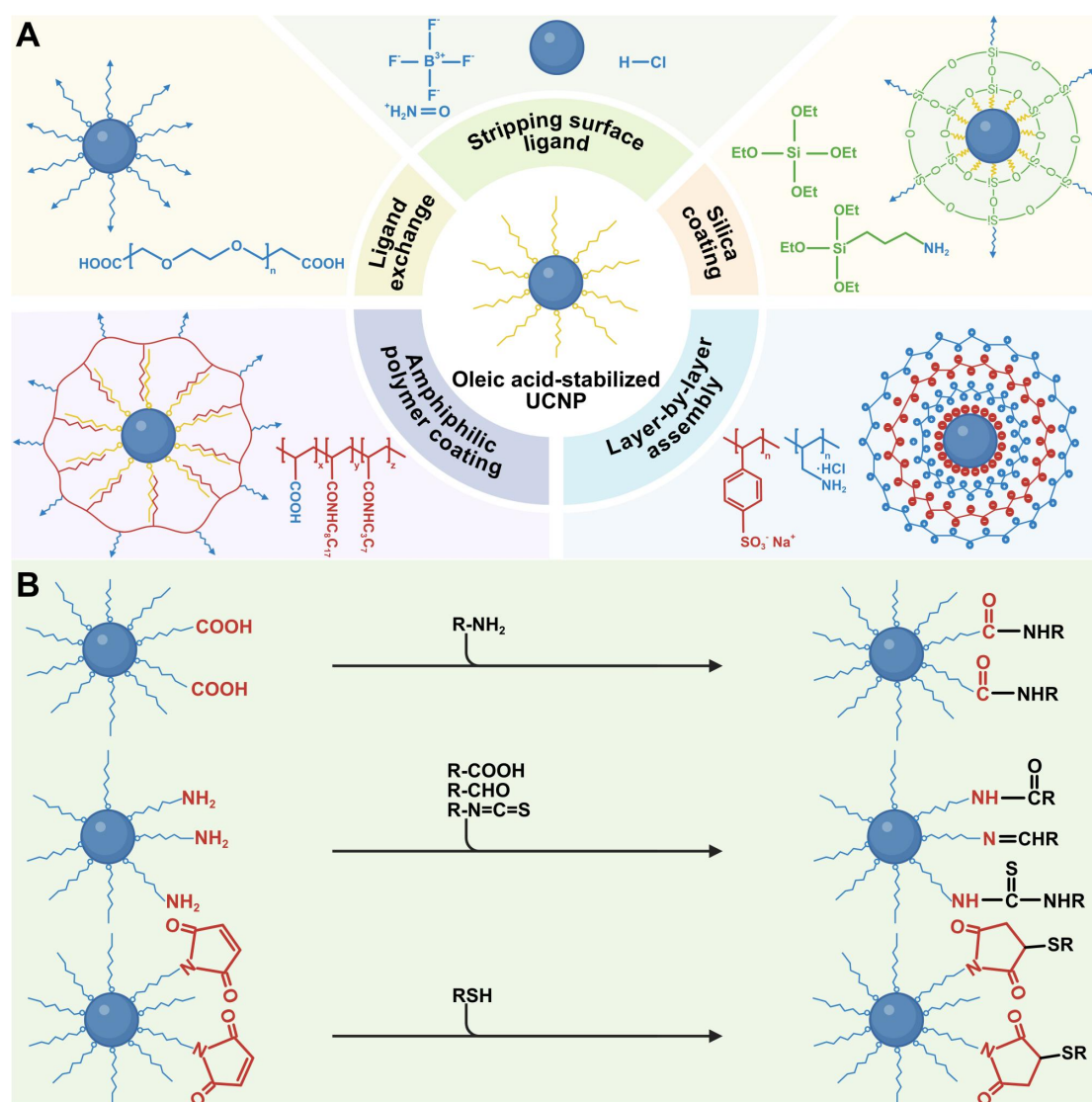


Figure 5. (A) Typical surface modification strategies applicable to UCNPs. (B) Scheme of covalent conjugation of UCNPs with biomolecules. Created with BioRender.com.

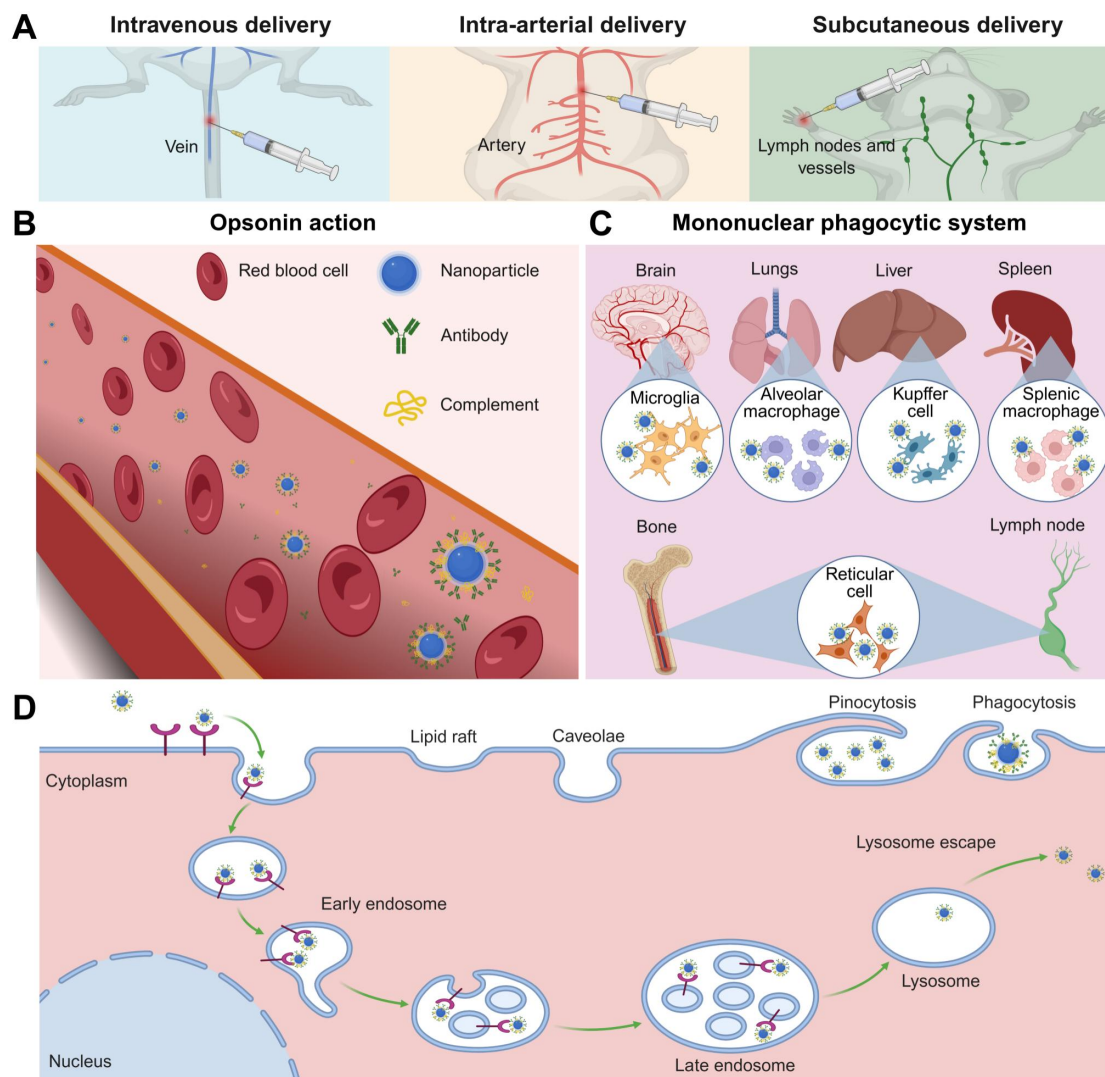


Figure 6. (A) Common delivery strategies. (B) Opsonin action and (C) phagocytosed by mononuclear phagocytic system. (D) Schematic diagram of endocytosis. Created with BioRender.com.



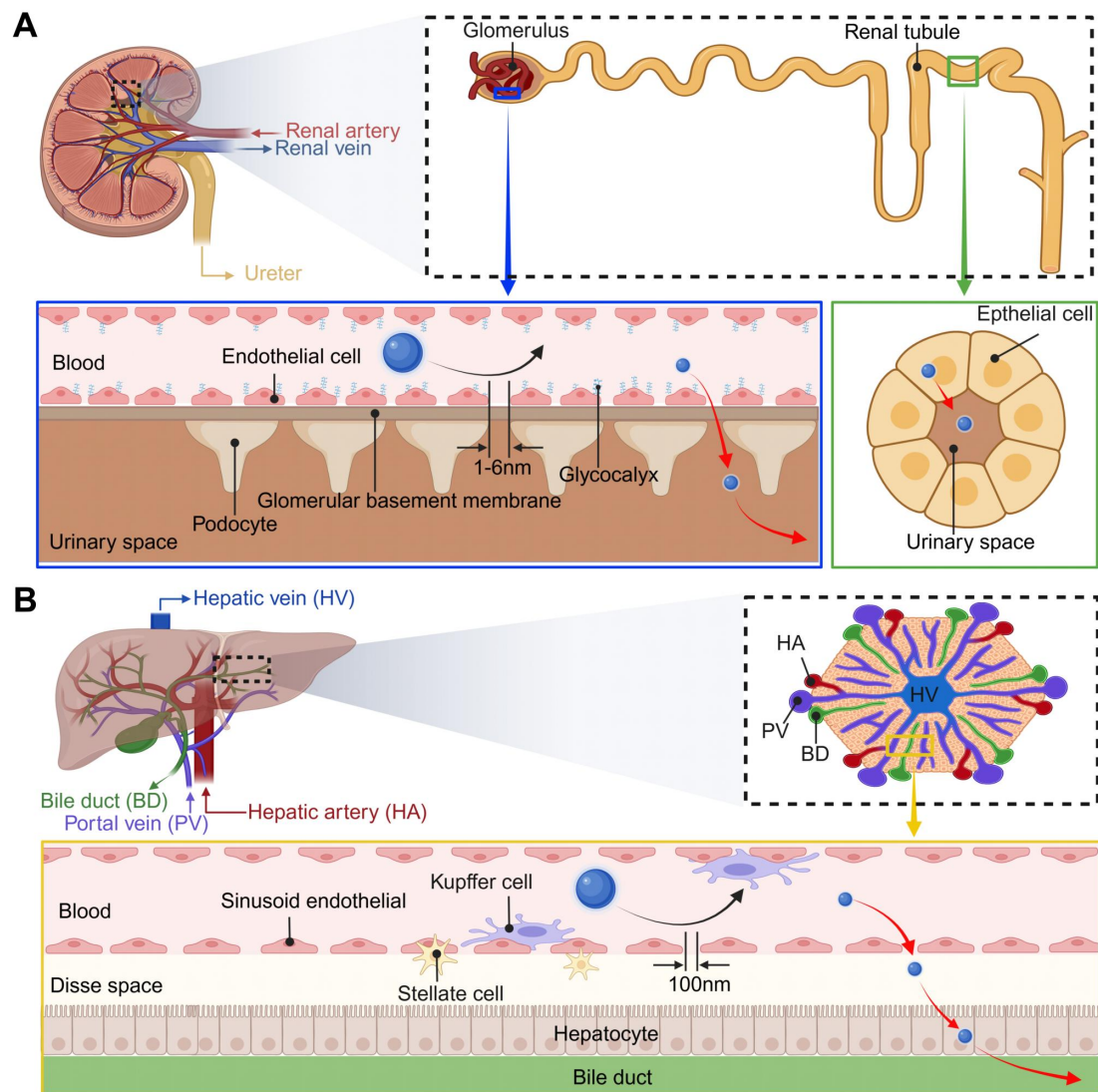


Figure 7. Size-dependent excretion of NPs in the kidneys and liver. (A) Kidney structures and excretion of NPs in the kidney. (B) Liver structures and excretion of NPs in the liver. Created with BioRender.com.



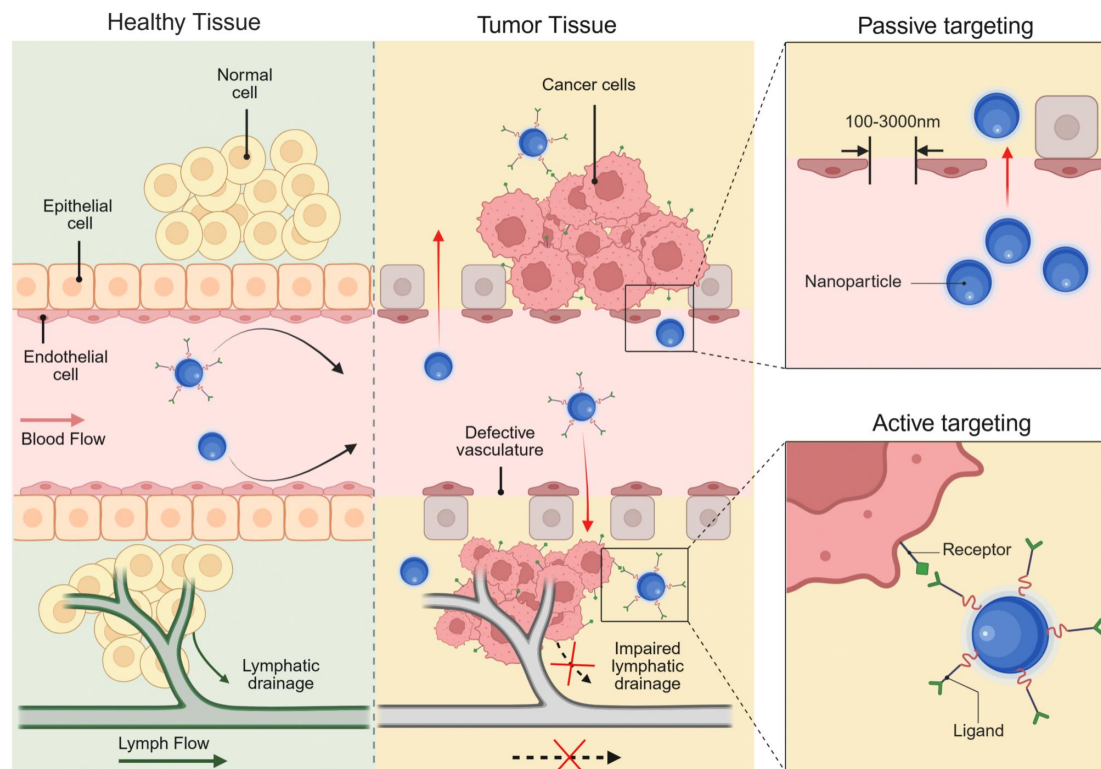


Figure 8. Passive and active targeting mechanism of NP on cancer cells. Created with BioRender.com.

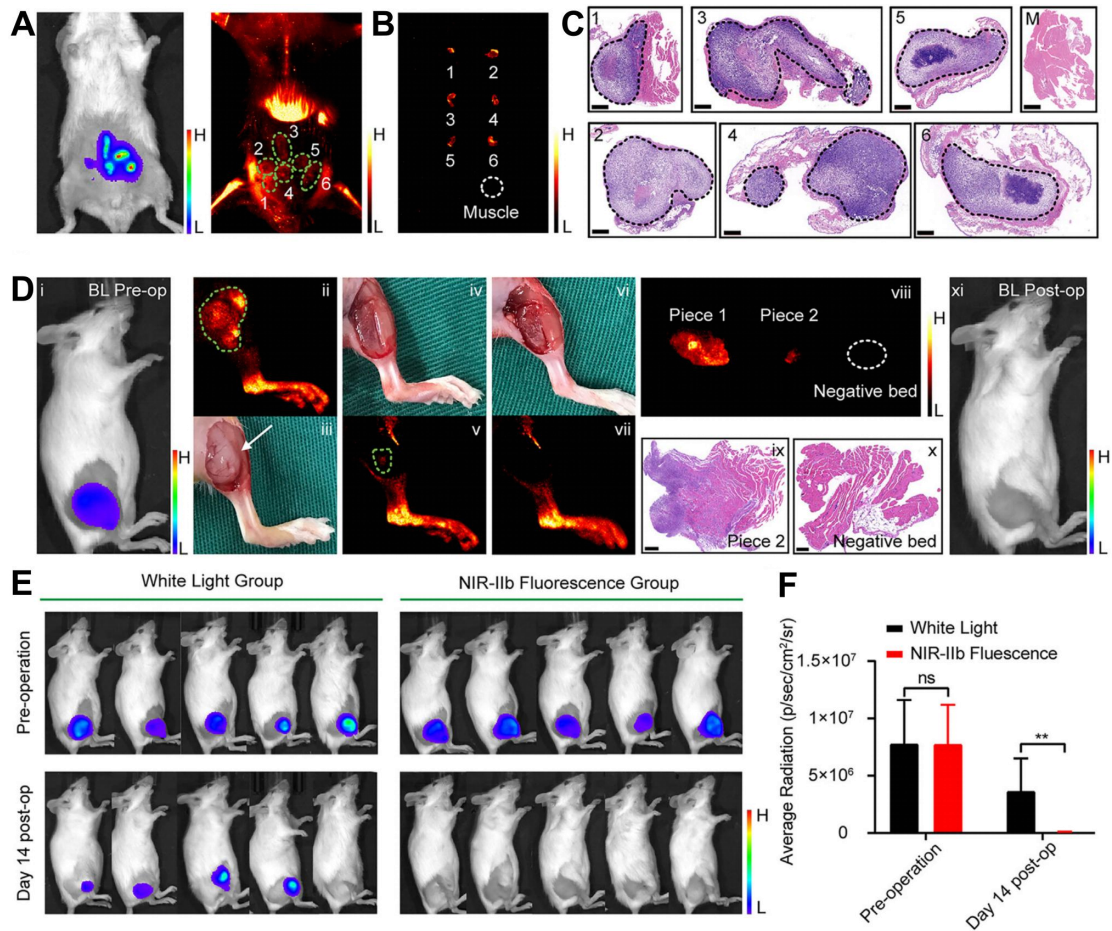


Figure 9. The identification and surgery of tumors in tumor-bearing mice under NIR-IIb fluorescence imaging navigation. (A) Representative bioluminescence (left) and NIR-IIb (right) images of a multiple microtumor mouse model. (B) Ex vivo NIR-IIb fluorescence imaging of resected pieces. (C) H&E staining of resected pieces. (D) Representative images during NIR-IIb fluorescence-guided surgery. (E) Bioluminescence images of mice before and 14 days after surgery under white-light (left) and NIR-IIb fluorescence guidance (right). (F) The corresponding average radiation of region of interest. Adapted with permission from [224], copyright 2022, under a Creative Commons CC BY license.

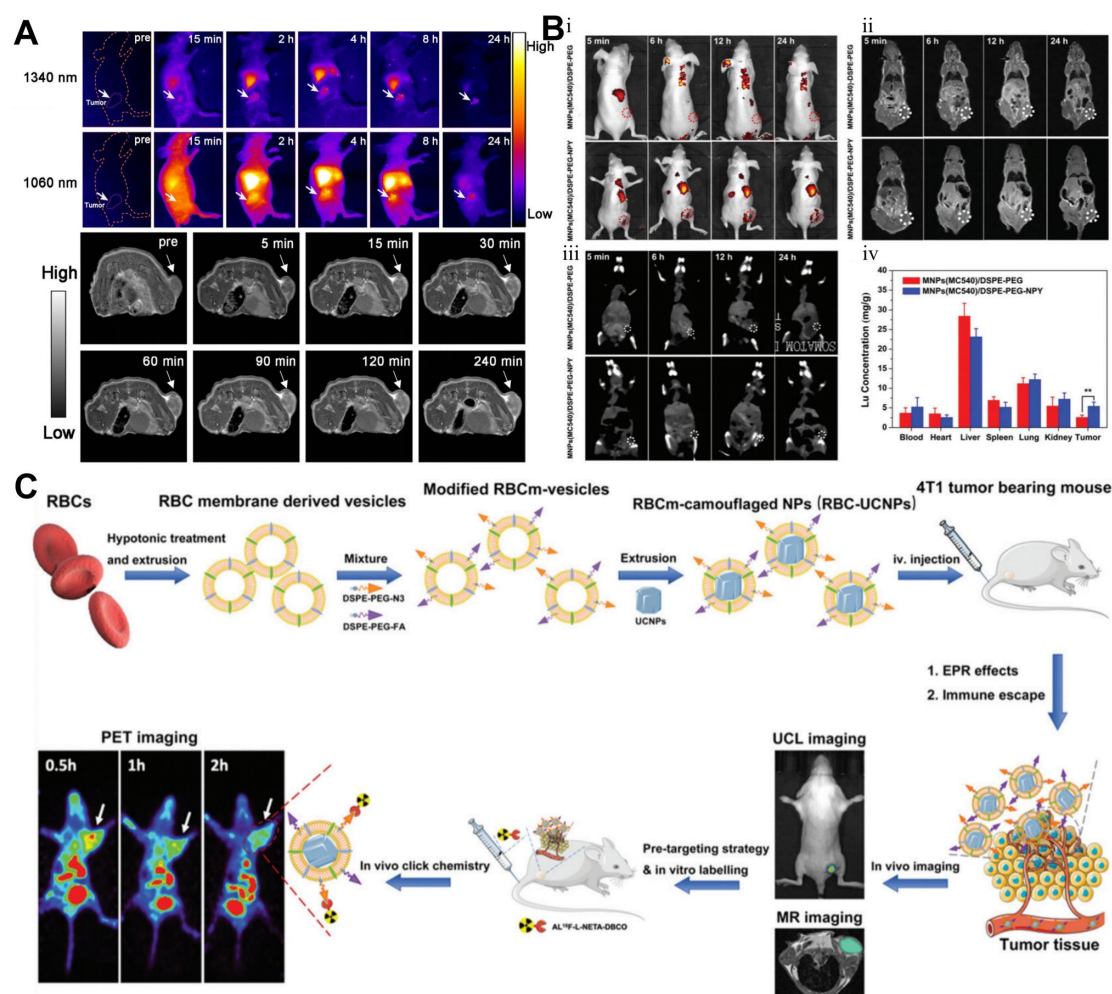


Figure 10. (A) In vivo dual-modal imaging based on the NPs. NIR-II fluorescence images of 4T1-tumor-bearing mice at 1060 and 1340 nm after NPs administration (top); T1-weighted MRI of breast tumor after injection with NPs for 0, 5, 15, 30, 60, 90, 120, and 240 min. The tumor area was marked with arrow (bottom). Adapted with permission from [226], copyright 2021, under a Creative Commons CC BY license. (B) In vivo multimodality imaging and biodistribution of  $Y_1$ Rs-ligand-functionalized nanocomposites. (i) UCL, (ii) MRI, and (iii) CT imaging of MCF-7 tumor-bearing nude mice after the intravenous injection of nanocomposites at 5 min, 6 h, 12 h, and 24 h; (iv) biodistribution of nanocomposites in the main organs of MCF-7 tumor-bearing mice at 12 h post-injection. Adapted with permission from [168], copyright 2018, Royal Society of Chemistry. (C) The schematic of the preparation process of the modified RBC-UCNPs and their applications of MRI, UCL imaging and PET imaging in TNBC bearing mice. Adapted with permission from [208], copyright 2020, Royal Society of Chemistry.



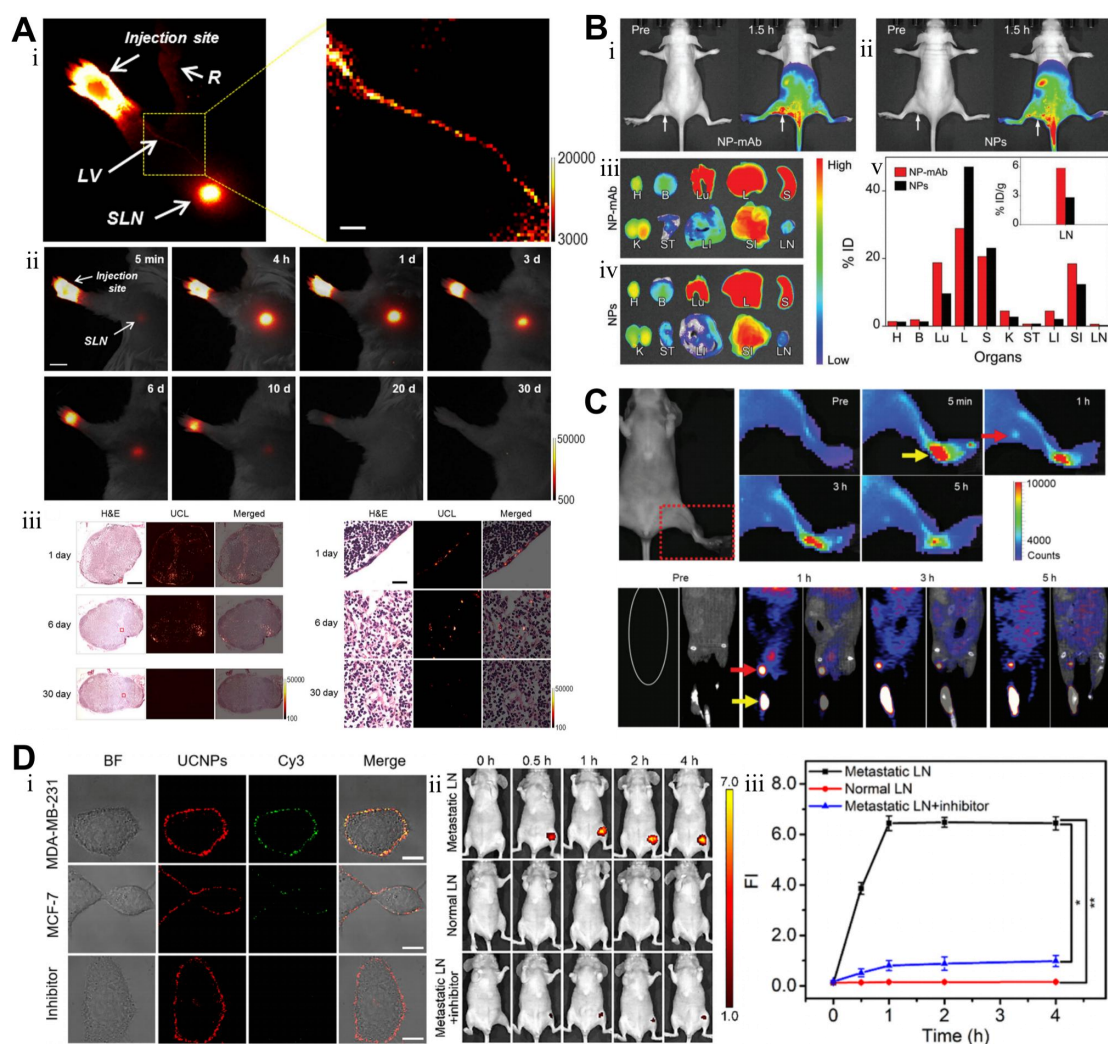


Figure 11. (A) Dynamic distribution of UCNPs in mice after footpad injection. (i) In vivo UCL image of mice after injection of the surface-modified UCNPs. LV, lymphatic vessel; SLN, sentinel lymph node; R, reflected secondary; (ii) In vivo UCL imaging of lymph node in the same mouse at different post-injection times. Mice were subcutaneously injected in the forepaw footpad with the UCNPs; (iii) H&E staining and corresponding UCL images of dissected axillary lymph nodes from the mice treated with UCNPs. The lymph nodes were obtained on 1, 6, and 30 days after the injections. Adapted with permission from [237], copyright 2016, under a Creative Commons CC BY license. (B) UCL images captured before and at 1.5 h after intravenously delivering the nanoprobe (i) and mother NPs (ii), respectively, into nude mice bearing metastatic lymph nodes as indicated by the white arrows; ex vivo UCL images of the main organs and lymph nodes captured right after acquiring the above images (iii, iv) (H, heart; B, brain; L, liver; S, spleen; LU, lung; K, kidney; ST, stomach; LI, large intestine; SI, small intestine; LN, lymph node), together with the quantified biodistribution profile (vi). Adapted with permission from [238], copyright 2018, Royal Society of Chemistry. (C) Fluorescence (top) and PET imaging (bottom) of metastatic lymph nodes (red arrow: lymphatic metastasis, yellow arrow: injection site in foot pad). Adapted with permission from [201], copyright 2022, under a Creative Commons CC BY license. (D) In situ protease secretion visualization and

metastatic lymph nodes imaging via a cell membrane-anchored upconversion nanoprobe. (i) Confocal microscopy images of upconversion nanoprobe-anchored MDA-MB-231 cells, MCF-7 cells, and inhibitor pre-treated MDA-MB-231 cells upon lipopolysaccharide activation; (ii) Fluorescence images and (iii) average fluorescence intensities of Cyanine 3 at 580 nm from metastatic lymph node, normal lymph node, and metastatic lymph node with the inhibitor in living mice before (0 h) and 0.5, 1, 2, and 4 h post NPs injection. Adapted with permission from [240], copyright 2021, American Chemical Society.

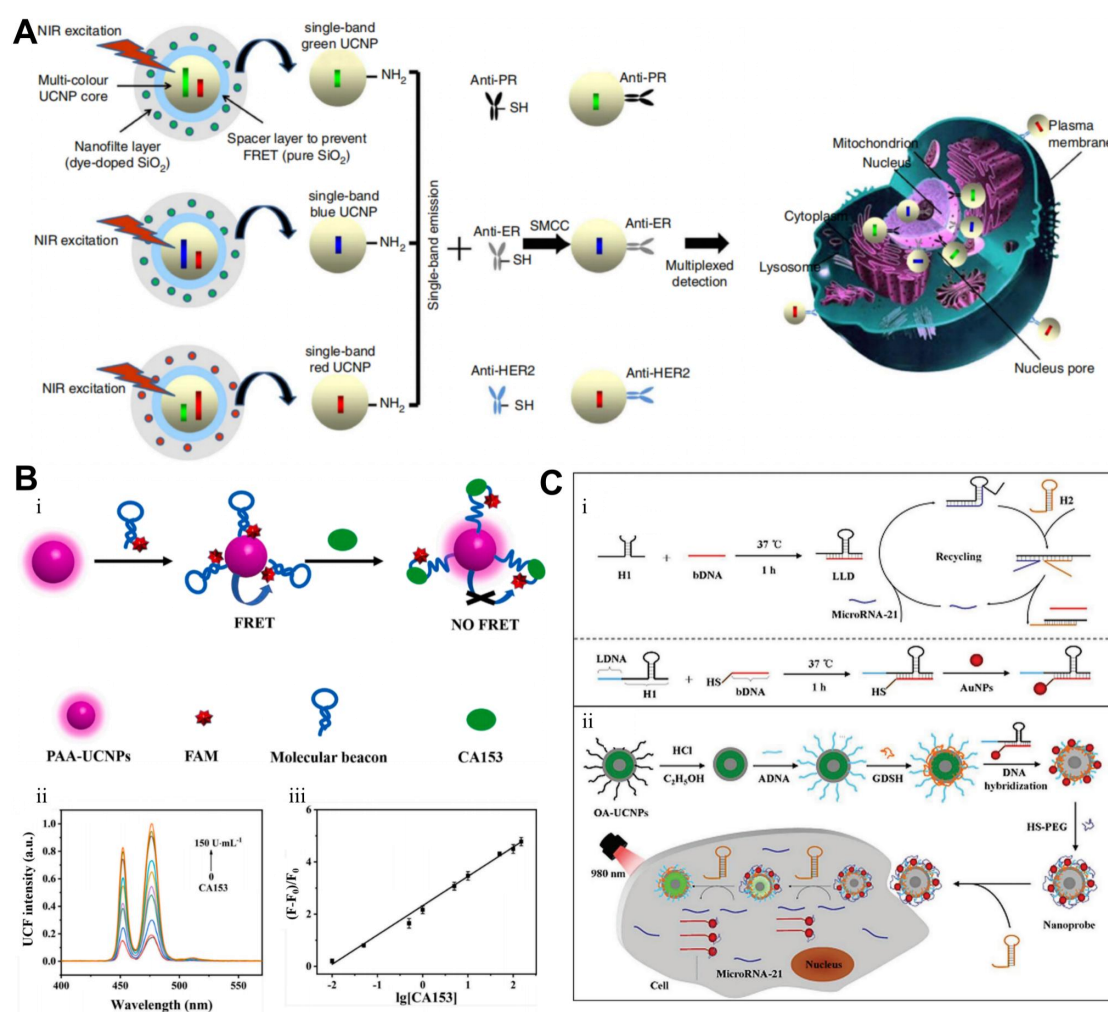


Figure 12. (A) Surface amino modifications of green, blue, and red single-band UCNP and antibody conjugates for multiplexed in situ molecular mapping of BC biomarkers PR, ER, and HER2. Adapted with permission from [247], copyright 2015, under a Creative Commons CC BY license. (B) (i) Working principle of CA153 biosensor based on FRET; (ii) UCL spectrum and (iii) the corresponding UCL intensity at 475 nm of the nanoprobe after reaction with various concentrations of CA153 in 100-fold diluted human serum. Adapted with permission from [253], copyright 2022, under a Creative Commons CC BY license. (C) Schematic illustration

of the preparation of lock-like DNA (top) and upconversion nanoprobe (bottom), and application in monitoring microRNA-21 in living cells. Adapted with permission from [269], copyright 2018, WILEY-VCH Verlag GmbH & Co. KGaA, Weinheim.

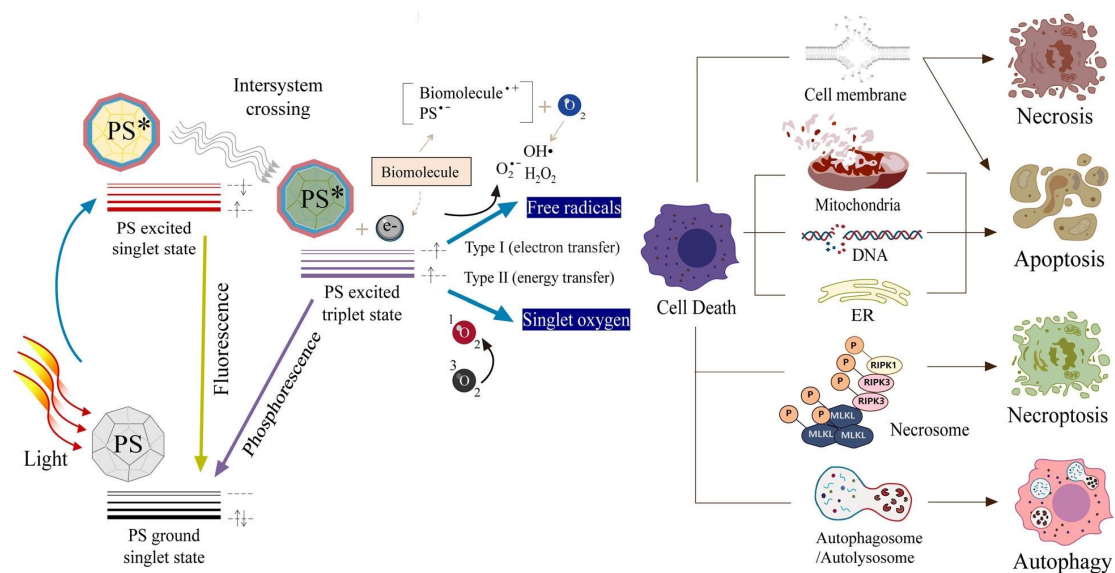


Figure 13. Mechanism of photodynamic reactions (either type I or type II) and cell death pathways in the process of PDT. Adapted with permission from [279], copyright 2021, under a Creative Commons CC BY license.

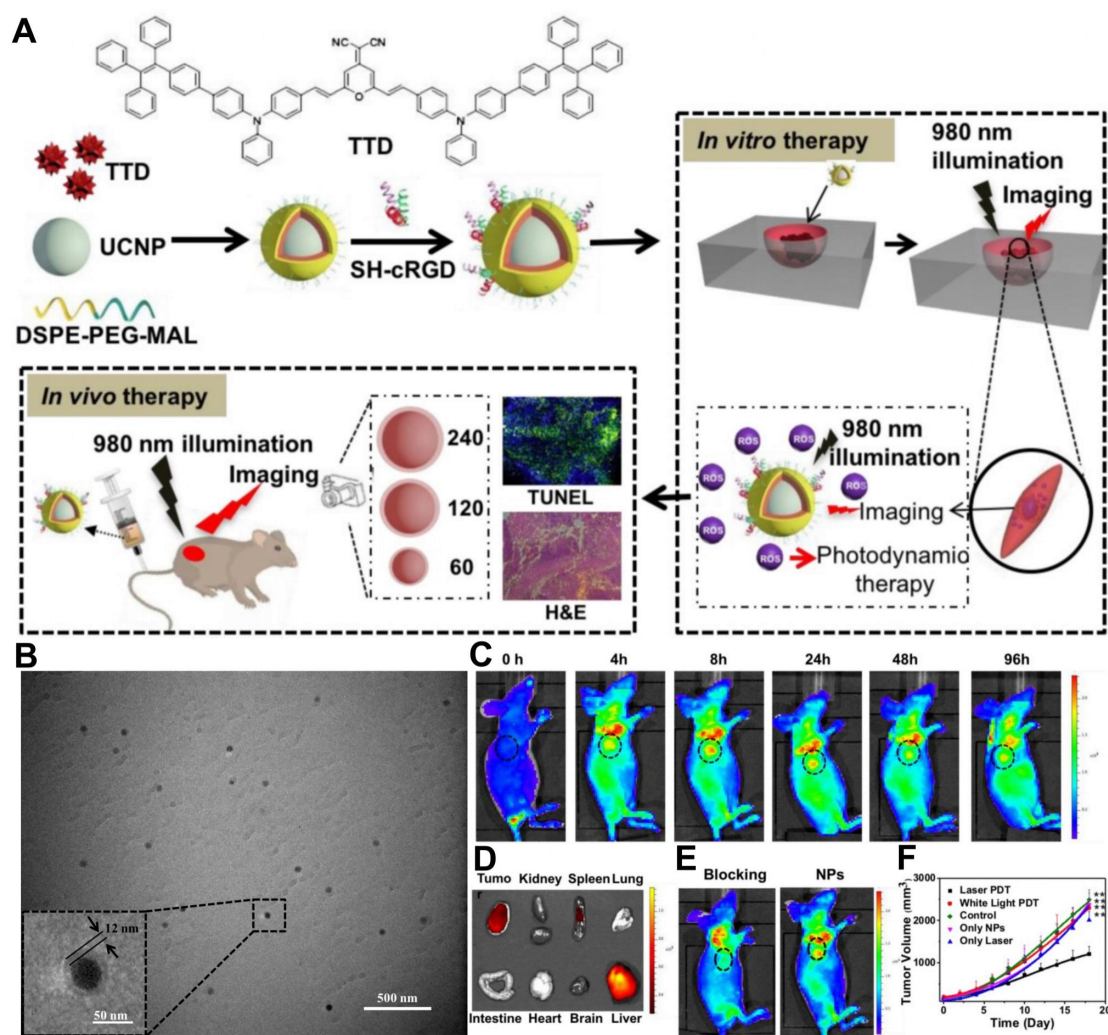


Figure 14. (A) Schematic illustration of preparation of NPs and their applications in bioimaging and PDT of deep-seated tumors upon NIR laser illumination, in an *in vitro* three-dimensional cancer cell spheroid and in a murine tumor model, respectively. (B) The morphology of NPs under transmission electron microscopy. (C) Biodistribution of NPs in tumor-bearing mice after intravenous injection of NPs (30 mg/kg) at different times. Black circles indicate the tumor. (D) Ex vivo fluorescence imaging of various organs and tumor tissues from mice intravenously injected with NPs. The mice were sacrificed at 12 h post-injection. (E) Biodistribution of NPs in tumor-bearing mice 8 h after intravenous injection of NPs (30 mg/kg) without or with blocking the receptors. Red circles indicate the tumor. (F) Growth curves of tumors in laser PDT, white light PDT, NP-only, laser-only and control groups, respectively, and NPs were intravenously injected into tumors with an initial tumor volume of 120 mm<sup>3</sup>. Adapted with permission from [286], copyright 2019, under a Creative Commons CC BY license.



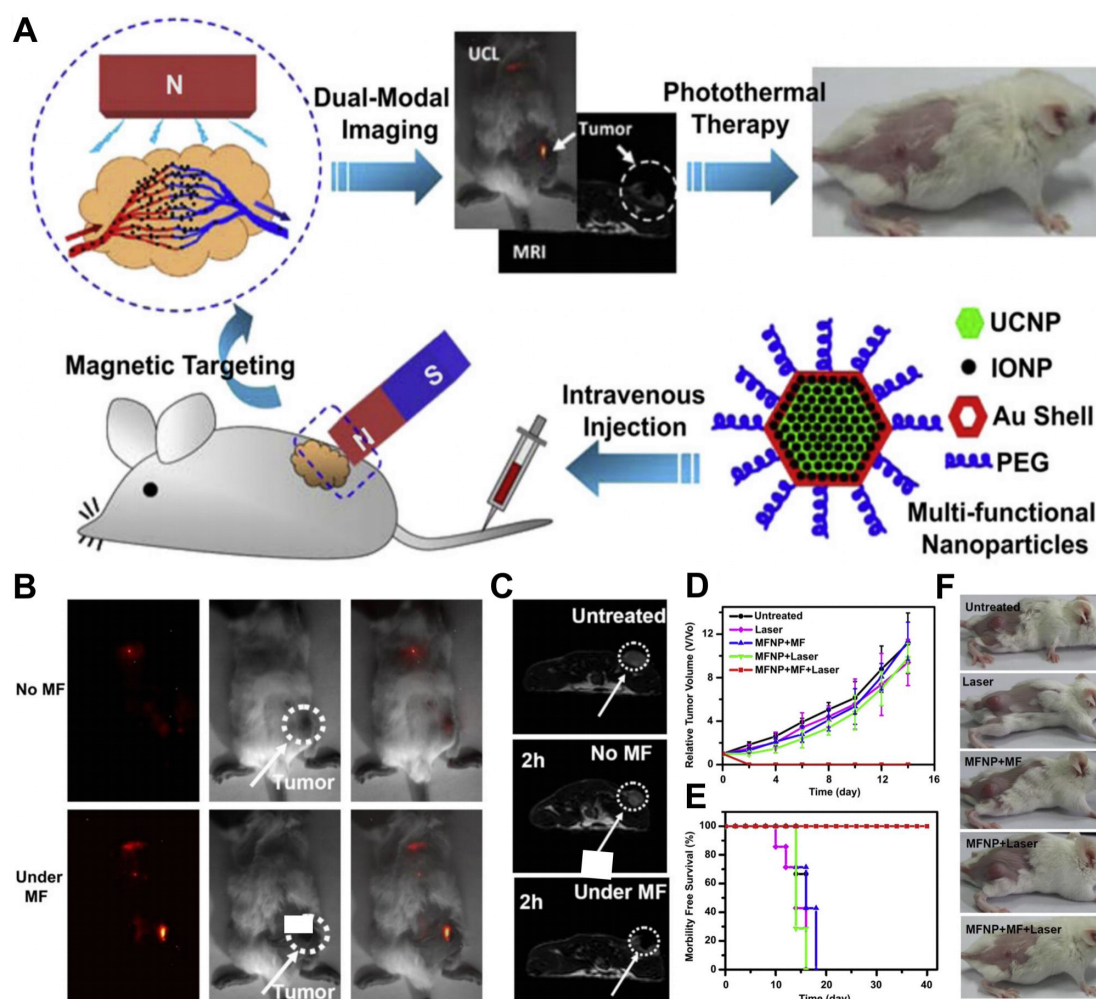


Figure 15. (A) A schematic illustration showing the composition of nanocomposites and the concept of in vivo imaging-guided magnetically targeted photothermal therapy. (B) Representative In vivo UCL images of 4T1 tumor-bearing Balb/c mice taken 2 h after injection of NPs under the tumor-targeted magnetic filed (top) and without the magnetic field (bottom). (C) Representative In vivo T2-weighted MRI images of 4T1 tumor-bearing mice with and without magnetic targeting acquired 2 h after injection of NPs. (D) The growth of 4T1 tumors in different groups of mice after treatment. (E) Survival curves of mice bearing 4T1 tumor after various treatments indicated. (F) Representative photos of mice after various treatments indicated. Adapted with permission from [294], copyright 2011, Elsevier Ltd. All rights reserved.



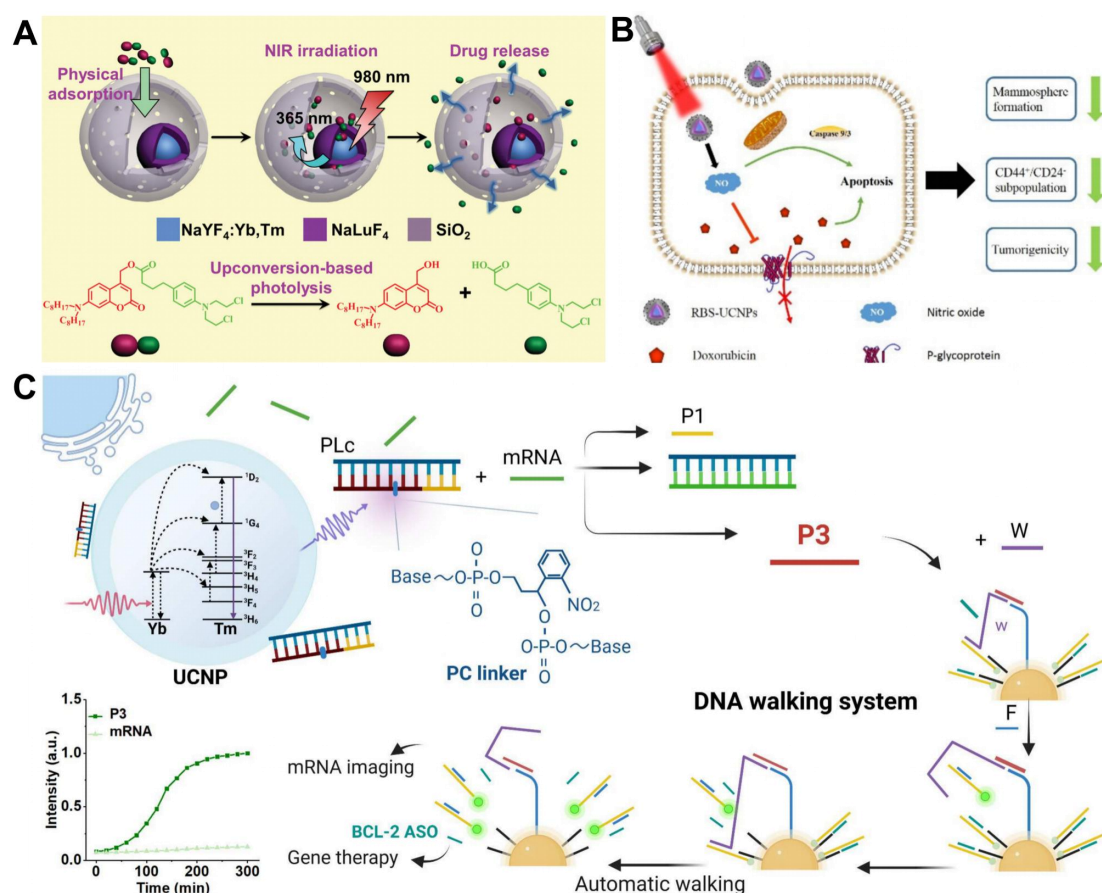


Figure 16. (A) Schematic illustration of the NIR-regulated upconversion-based phototrigger-controlled drug-release device and the photolysis of the prodrug under upconversion emission from the UCNPs. Adapted with permission from [308], copyright 2013, WILEY-VCH Verlag GmbH & Co. KGaA, Weinheim. (B) Schematic diagram of the synergistic treatment of NO released from NPs and DOX. Adapted with permission from [313], copyright 2017, Science China Press. Published by Elsevier B.V. and Science China Press. All rights reserved. (C) Illustration of Intracellular NIR photoactivatable NPs can released P3 DNA in the presence of mRNA, and P3 can activated downstream operation of entropy-driven DNA walking system for survivin mRNA imaging and gene therapy with highly spatiotemporal resolution. The fluorescence dynamic curve on the left showed the P3-initiated DNA walking system. Adapted with permission from [316], copyright 2023, Elsevier Ltd. All rights reserved.

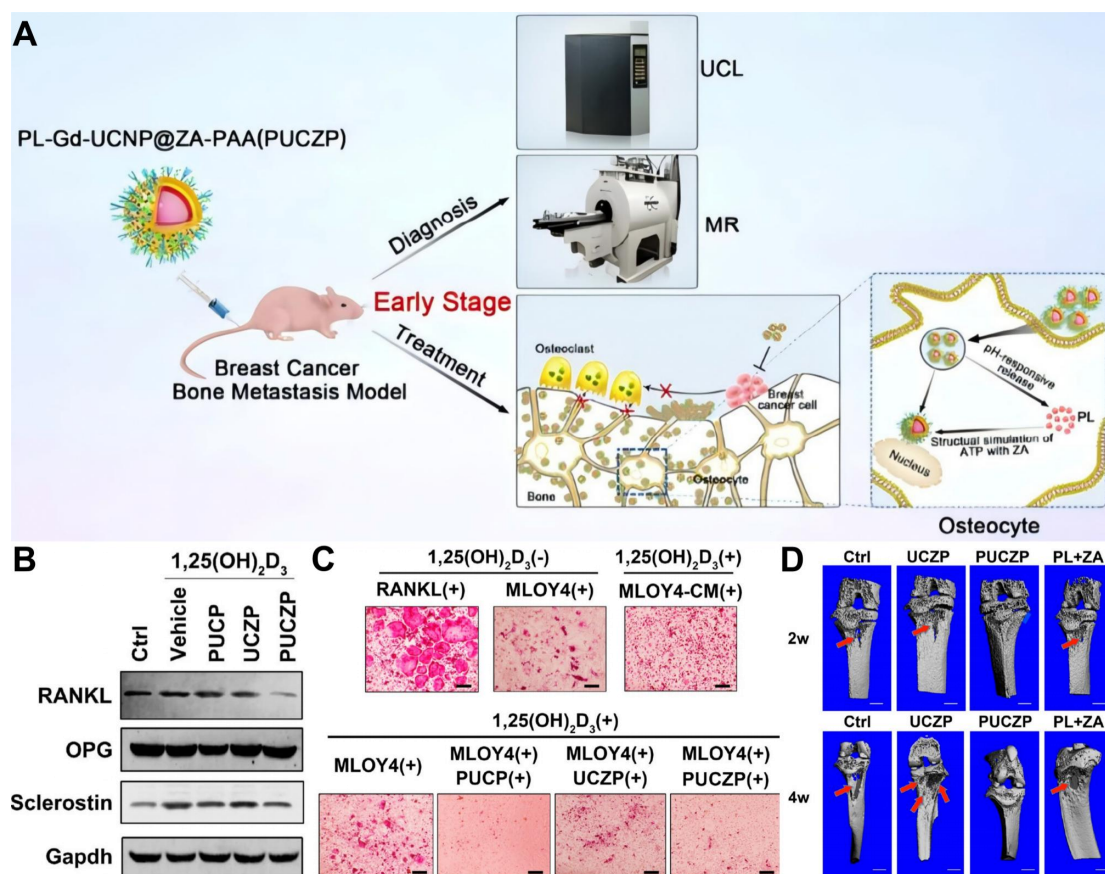


Figure 17. (A) Scheme illustration of the theranostic bone-targeting Gd (III)-doped UCNPs. (B) Western blot of RANKL, OPG, and sclerostin in MLOY-4 cells treated with varying NPs. (C) Murine bone marrow monocytes were treated with various interventions for 7 consecutive days. TRAP staining was used to indicate mature multinucleated osteoclast cells. (D) Representative  $\mu$ CT tomography of bone metastasis in specimens from nude mice treated with various NPs after 2/4 weeks. Red arrows indicate the osteolysis lesions. Adapted with permission from [320], copyright 2017, American Chemical Society.

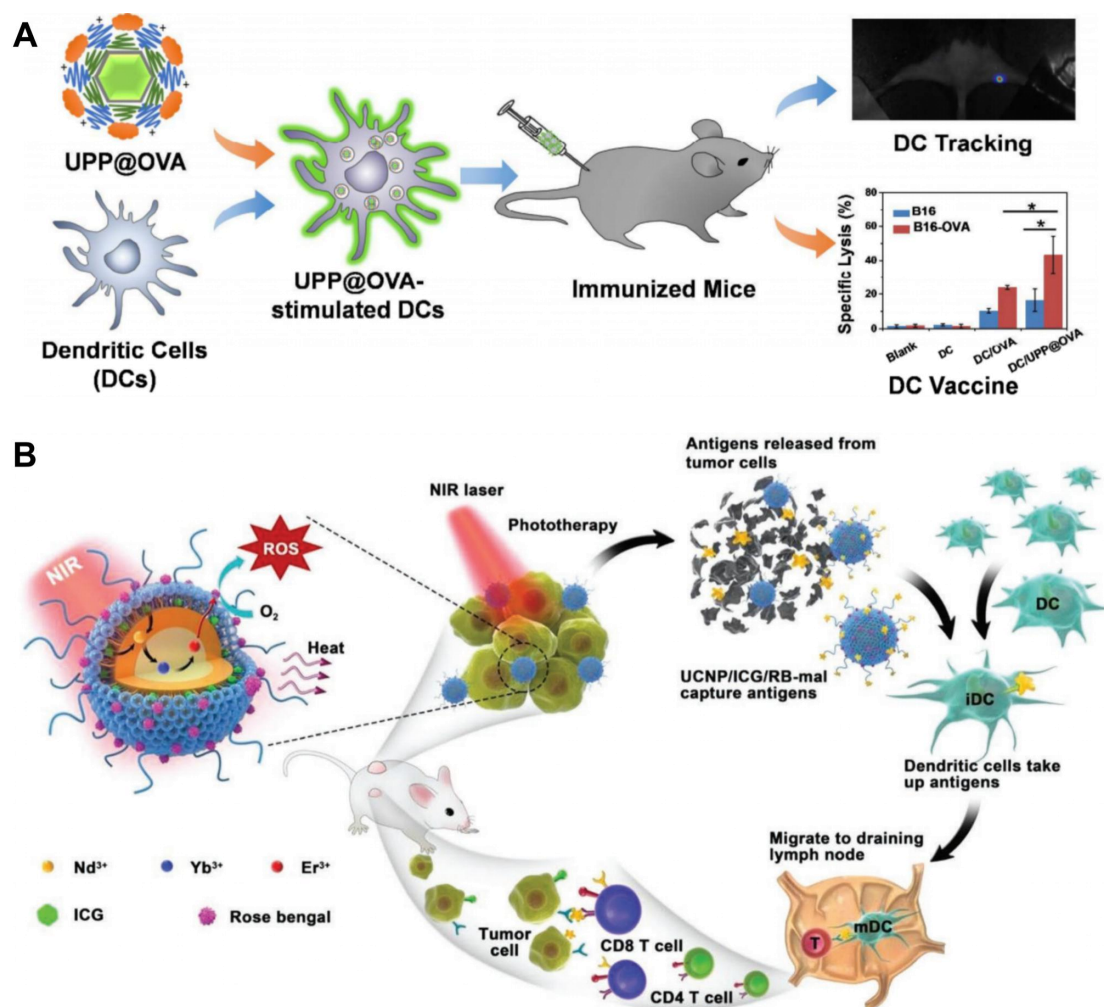


Figure 18. (A) Schematic illustration of antigenloaded UCNPs for DC stimulation, tracking and vaccination in DC based immunotherapy. Bipolymer-coated UCNPs-PEG-PEI (UPP) NPs were synthesized and loaded with ovalbumin (OVA) via electrostatic interaction to form UPP@OVA complexes. These complexes were efficiently internalized by DCs, inducing DC maturation and cytokine secretion. The UCL property of UCNPs enabled highly sensitive in vivo tracking of DC migration, demonstrating homing of labeled DCs to draining lymph nodes. Compared with free OVA-pulsed DCs, UPP@OVA-pulsed DC vaccines significantly enhanced T cell proliferation, interferon- $\gamma$  secretion, and cytotoxic T lymphocyte mediated responses, providing a novel trackable strategy for immunotherapy. Adapted with permission from [335], copyright 2015, American Chemical Society. (B) Schematic illustration of both fabrication and mechanism of NIR-triggered antigen-capturing nanoplatform for synergistic photo-immunotherapy. The NIR-triggered antigen-capturing nanoplatform was constructed via self-assembly of PEG and indocyanine green onto the oleate-capped UCNPs, followed by remote loading of RB. Upon NIR laser activation, the photodynamic therapy efficiency of NPs was significantly enhanced by indocyanine green modification, while simultaneously achieving selective PTT. Next, tumor-derived protein antigens arising from NPs based phototherapy can be captured and retained in situ, which increases the effects of antigen uptake by

antigen-presenting cells to induce a tumor-specific immune response. Adapted with permission from [345], copyright 2019, under a Creative Commons CC BY license.



Figure 19. Challenges in nanomedicine clinical translation. Key translational and industrial aspects of nanomedicine product development are depicted. Challenges are traditionally approached in a bottom-up manner. However, also considering challenges in a top-down manner, from the vantage point of end-users, with commercial, practical, and clinical feasibility firmly in mind, is considered to be important for ensuring success. The top-down analysis allows for the identification-from the initiation of the clinical translation process onwards-of the most important issues that can be encountered along the way, triggering proactive thinking and planning to overcome potential challenges already at early stages. Adapted with permission from [363], copyright 2020, under a Creative Commons CC BY license.

Table 1. Advantages and disadvantages of common fluorescent probes.

Probes	Examples	Advantages	Disadvantages	Ref.
UCNPs	NaYF <sub>4</sub> :Yb,Er; NaGdF <sub>4</sub> :Yb,Tm;	Large anti-Stokes shift; Narrow emission spectra; Long fluorescence lifetime; Strong stability;	Low quantum yield; Potential biotoxicity;	[364]
Fluorescent proteins	GFP; RFP; BFP;	High biocompatibility; Genetically encodable;	Poor stability; Shallow tissue penetration; Moderate quantum yield;	[365]

Organic dyes	Cy5; FITC; ICG;	High quantum yield; Ease of functionalization and bioconjugation;	Poor stability; Biotoxicity; Broad emission spectra;	[366 ]
Quantum dots	CdSe@ZnS; CdTe; InP@ZnS;	High quantum yield; Broad excitation spectra; Narrow tunable emission; Strong stability;	Heavy metal toxicity; Photoblinking;	[367 ]
Metal complexes	[Ru(bpy) <sub>3</sub> ] <sup>2+</sup> ; Ir(ppy) <sub>3</sub> ;	Long fluorescence lifetime; Strong stability; Tunable redox activity;	Heavy metal toxicity; Poor stability; Shallow tissue penetration;	[368 ]
Carbon dots	Nitrogen-doped carbon dots; B-doped carbon dots;	Low biotoxicity; Strong stability;	Moderate quantum yield; Broad emission spectra; Limited functionalization and bioconjugation capacity;	[369 ]

GFP: green fluorescent protein; RFP: red fluorescent protein; BFP: blue fluorescent protein; Cy5: cyanine 5; FITC: fluorescein isothiocyanate; ICG: indocyanine green.

Table 2. Cell viability after incubation with UCNPs.

UCNPs	Surface modification	Size (nm)	Zeta potential (mV)	Exposure time (h)	Concentration ( μ g·mL <sup>-1</sup> )	Viability	Cell line	Ref.
Ba <sub>2</sub> GdF <sub>7</sub> :Yb,Er	PEG	24±5	25.73	24	5000	>85%	HepG2	[163]
BaYbF <sub>5</sub> :Tm	PAA	14.7±3.5	-19.8	24	0.1–1000	>90%	HepG2	[370]
				48	0.1–1000	>90%		
NaYF <sub>4</sub> :Gd,Yb,Er	Citrate; <sup>18</sup> F;	28.2	18.1	4	100–500	>89%	KB	[371]
				24	100–500	81%		
Lu <sub>2</sub> O <sub>3</sub> :Gd,Yb,Er	PEG	85–130	-0.65	48	1000	>90%	MCF-7	[372]
NaLaMgWO <sub>6</sub> :Yb, Er	-	105	-	48	50–200	100%	WI-38	[373]
NaGdF <sub>4</sub> :Tm,Er,Yb	Azelaic acid (carboxylic acid)	25–60	-	4	62.5–500	>90%	KB	[374]
				12	62.5–500	>90%		
NaGdF <sub>4</sub> :Yb,Er	PEI; Phycocyanin;	260.6±7.3	8.1±1.2	24	12.5–200	>80%	RAW264 .7	[375]
				24	12.5–200	>80%	HeLa	
NaYF <sub>4</sub> :Yb,Er	PEI; FA;	7	-55	24	750–12000	90%	HeLa	[376]
				4	125–500	80%		
LaF <sub>3</sub> :Yb,Ho	PEG	15	-	12	125–250	>80%	KB	[377]
				24	125–250	>80%		
NaYF <sub>4</sub> :Tm,Yb @NaYF <sub>4</sub> :Nd,Yb	SiO <sub>2</sub> ; MMP2-sensiti ve peptide;	30	-	72	1–250	100%	Cal27	[378]
					1–250	>90%	FADU	
					1–250	>90%	OEC-M1	



NaLuF <sub>4</sub> :Yb,Er	CuInS <sub>2</sub> /ZnS quantum dot; Polypyrrole; PEG; DNA; DOX; PEG;	70	4.6	48	200–1000	>80%	HEK293 T	[379]
NaYF <sub>4</sub> :Yb,Tm	Metal-organic framework; SiO <sub>2</sub> ; Polyvinylpyrrolidone; Methylene blue;	500	-	24	25–1000	>90%	MCF-7	[380]
K <sub>0.3</sub> Bi <sub>0.7</sub> F <sub>2.4</sub> :Yb,Er		50	-	24	75–100	90%	C6	[381]
Y <sub>2</sub> O <sub>3</sub> :Er,Yb	FA; SiO <sub>2</sub> ;	70±10	-11.8±4.30	24	0.001–1	>80% >80% >80%	HeLa MDA-MB-231 MCF-7	[219]
NaYF <sub>4</sub> :Yb,Tm@NaYF <sub>4</sub>	4T1 cell membrane; Semiconductor material; Hydrogen-bonded organic framework materials; PAA;	110	-	24	25–150	>90%	L929	[382]
NaYF <sub>4</sub> :Yb,Er@NaYF <sub>4</sub> :Nd@NaYF <sub>4</sub>		48.2	-12.97	24	37.5–600	>90%	4T1	[383]
NaYF <sub>4</sub> :Yb,Tm@NaYF <sub>4</sub> :Yb,Nd	SiO <sub>2</sub> ; Covalent organic framework;	421.0±40.3	10.8±2.5	24 48 72	10–200 10–200 10–200	100% 100% 110%	BJ BJ BJ	[384]
PEG: polyethylene glycol; PAA: polyacrylic acid; PEI: polyethylene imine; FA: folic acid; MMP: matrix metalloproteinase; DOX: doxorubicin.								

Table 3. Safety studies of UCNPs in rodents.

UCNPs	Surface modification	Size (nm)	Zeta potential (mV)	Animal	Route	Dosage	Results	Ref.
Ba <sub>2</sub> GdF <sub>7</sub> :Yb,Er	PEG	24±5	25.73	Nude mice (25 g)	Tail vein injection	2–4 mg/mL (0.2 mL)	Major organ pathological sections normal; Hemolysis assay confirmed no blood cell damage;	[163]
BaYbF <sub>5</sub> :Tm	PAA	14.7±3.5	-19.8	Kunming mice	Oral	100 mg/mL	Major organ pathological sections normal; Female	[370]

						(0.4 mL)	mice litter size unchanged;	
					Anus	20 mg/mL (0.8 mL)	Rectal mucosa epithelium intact, no ulcers or inflammatory cell infiltration;	
				Wistar rats	Oral	20 mg/mL (5 mL)	Blood concentrations of Ba <sup>2+</sup> , Yb <sup>3+</sup> < 0.1 ng/mL	
					Anus	20 mg/mL (5 mL)	In vitro hemolysis rate < 0.5%	
Lu <sub>2</sub> O <sub>3</sub> : Gd,Yb, Er	PEG	85–13 0	-0.65	Kunming mice	Tail vein injection	100 mg/kg	Body weight stable; normal diet, activity, and hair; major organ pathological sections normal; Hematological and biochemical parameters normal; Female mice litter size unchanged;	[372]
NaGdF <sub>4</sub> :Tm,Er, Yb	Azelaic acid (carboxylic acid)	25–60	-	Kunming mice (20 g)	Tail vein injection	1.5 mg/kg	No significant weight loss, abnormal behavior, or reproductive changes	[374]
NaLuF <sub>4</sub> :Yb,Er	Polypyrrole; PEG; DNA; DOX;	70	4.6	BALB/c nude mice (16–18 g)	Intraven ous injection	9.4 mg/kg	Major organ pathological sections normal; Hematological and biochemical parameters normal;	[379]
NaLuF <sub>4</sub> : <sup>153</sup> Sm, Yb,Tm	6-aminohexa noic acid	25–30	-	Kunming mice (20 g)	Tail vein injection	20 mg/kg	Major organ pathological sections normal; Hematological and biochemical parameters normal;	[385]
Gd <sub>2</sub> O <sub>3</sub> : Yb,Er	PEG	90–15 0	-	Kunming mice	Tail vein injection	10 mg/kg	Body weight gain patterns normal; Mild inflammation in liver/spleen tissues; Hematological and biochemical parameters normal;	[66]
NaLuF <sub>4</sub> :Yb,Er	Polyaniline NPs; Pluronic F127;	120	0	NU/NU nude mice	Intraven ous injection	2 mg/mL (0.1 mL)	Major organ pathological sections normal; Biochemical and renal parameters normal;	[386]

PEG: polyethylene glycol; PAA: polyacrylic acid; PEI: polyethylene imine; FA: folic acid; DOX: doxorubicin; NPs: nanoparticles; Pluronic F127: poly (ethylene

glycol)-block-poly (propylene glycol)-block-poly (ethylene glycol).

Table 4. Applications of UCNPs in BC molecular imaging.

Application	UCNPs	Surface modification	Size (nm)	Zeta potential (mV)	Results	Ref.
UCL imaging	NaYF <sub>4</sub> :Yb, Er	Recombi-nant scFv4D5 mini-antibody; Poly(maleic anhydride-alt-1-octadecene) Methylene blu;	120±20	-53	Showned specific binding and uptake to SK-BR-3 cells; Predicted UCNPs-assisted cancer detection feasible at up to 4 mm tissue depth;	[206]
UCL imaging	NaYF <sub>4</sub> :Yb, Er	Liposomes; PEG; Anti-HER2 peptides; Zinc tetracarboxyp	90±1.9 2	-18.3±1. 56	Showned specific binding and uptake to SKBR-3 cells	[202]
UCL imaging	NaYF <sub>4</sub> :Yb, Er	henoxy phthalocyanine; Trastuzumab; FA-PEG-poly (aspartic acid-hydrazo	23	-14.5±4. 3	Showned specific binding and uptake to SKBR-3 cells	[216]
UCL imaging	NaYF <sub>4</sub> :Yb, Er	ne)-dihydroli poic acid; Pheophorbide a;	90.3	-	Showned specific binding and uptake to MCF-7 cells	[221]
UCL imaging	Y <sub>2</sub> O <sub>3</sub> :Yb, Er/Gd <sub>2</sub> O <sub>3</sub> : Yb,Er	SiO <sub>2</sub> ; FA;	70/50	-	Showned specific binding and uptake to MCF-7 cells	[220]
UCL imaging	Y <sub>2</sub> O <sub>3</sub> :Yb, Er	SiO <sub>2</sub> ; FA;	70	-11.8±4. 30	Showned specific binding and uptake to MCF-7 and MDA-MB-231 cells	[219]
UCL imaging	NaYF <sub>4</sub> :Yb, Er	Nanoscale metal organic framework; FA;	180±20	-	Showned specific binding and uptake to MDA-MB-468 cells	[222]



UCL imaging	NaYF <sub>4</sub> :Yb, Er,Tm	Arginine-glycine-aspartate; PEG;	25.8	-	<p>Showed specific binding and uptake to U87MG cells; Maximum binding of the material in U87MG tumors occurred at 4 hours after tail-vein injection and persisted until 24 hours; The SNR was about 24; Detected no autofluorescence signal even at 600 <math>\mu</math>m depth;</p>	[223]
FL imaging	NaErF <sub>4</sub> @NaYF <sub>4</sub>	Cyclic Arg-Gly-Asp sequence-containing pentapeptide c; PEG;	61.3	-	<p>Showed specific binding and uptake to 4T1 cells; Imaging penetration depth 9 mm; SBR at 5 mm depth fourfold ICG; Effectively distinguished malignant from normal tissues, identified microtumors, and guided complete tumor resection during surgery;</p>	[224]
FL/MRI imaging	NaGdF <sub>4</sub> :Nd@NaLuF <sub>4</sub>	PEG	32.7	-	<p>The fluorescence signal peaked at 4 h post-injection, with a TBR of 8.2 at 1340 nm; The 4T1 tumor MRI signal was enhanced by 1.46-fold at 6 h post-injection;</p>	[226]
UCL/MRI imaging	NaGdF <sub>4</sub> :Yb,Er@NaGdF <sub>4</sub> :Yb@NaGdF <sub>4</sub> :Yb,Nd	mSiO <sub>2</sub> ; Site-specific peptide; Chlorin e6;	157.7	12.4	<p>Showed specific binding and uptake to MDA-MB-435 cells; Showed good T<sub>1</sub>-weighted MRI performance;</p>	[387]
UCL/MRI/CT imaging	LiLuF <sub>4</sub> :Yb,Er@nLiGdF <sub>4</sub>	PEG; mSiO <sub>2</sub> ; The Y <sub>1</sub> receptor ligand;	106.7	-12.7	<p>Red blood cell membrane; PEG; FA;</p>	[228]
UCL/MRI/PE T imaging;	NaGdF <sub>4</sub> :Yb,Tm	MDA-MB-231 cell membrane; PEG; <sup>18</sup> F;	138.9	-12.1	<p>Showed specific binding and uptake to 4T1 cells; UCL signal persisted <math>\geq</math>48 h; Enhanced tumor MRI signal;</p>	
UCL/MRI/PE T imaging	NaGdF <sub>4</sub> :Yb,Tm@NaGdF <sub>4</sub>	PEG; Anti-HER2 monoclonal antibody;	200	-10 to -20	<p>Showed specific binding and uptake to MDA-MB-231 cells; UCL signal persisted <math>\geq</math>48 h;</p>	[235]
UCL imaging	NaGdF <sub>4</sub> :Yb,Tm,Ca@NaLuF <sub>4</sub>		137	-0.7	<p>Showed specific binding and uptake to SK-BR-3 cells; Blood half-life 421 min; Tissue penetration depth 7.7 mm; Metastatic lymph nodes revealed; Fluorescence intensity stable <math>\geq</math>7 days in various solutions; Showed stronger optical stability (vs. ICG) under continuous laser, deeper penetration;</p>	[238]
FL imaging	NaErF <sub>4</sub> @NaYF <sub>4</sub>	PAA; Balixafortide;	18.6 $\pm$ 0.8	-23.41		[239]

					Sentinel lymph node metastasis accurately detected;	
UCL/PET/SP ECT imaging	NaGdF <sub>4</sub> :Yb,Tm@NaLuF <sub>4</sub>	PEG; Anti-HER2 monoclonal antibody; <sup>68</sup> Ga; <sup>177</sup> Lu; Cyanine 3; Anti-EGFR antibody; PEG; Atrix	22.5±2.94	12.63	Shown specific binding and uptake to SK-BR-3 cells; Reduced lymph node metastasis, inhibited tumor growth;	[201]
UCL imaging	NaYF <sub>4</sub> :Gd,Yb,Er@NaYF <sub>4</sub>	metalloprotein 2 substrate peptide labeled with QSY7 quencher;	85.7±2.3	10.8±1.5	Metastatic lymph nodes revealed	[240]
PEG: polyethylene glycol; FA: folic acid; UCL: upconversion luminescence; FL: fluorescence; PET: positron emission tomography; SPET: single-photon emission computed tomography; CT: computed tomography; SNR: signal-to-noise ratio; SBR: signal-to-background ratio; ICG: indocyanine green; TBR: tumor-to-background ratio; PAA: polypropylene acid.						

Table 5. Applications of UCNPs in BC biomarker detection.

UCNPs	Surface modification	Size (nm)	Zeta potential (mV)	Biomarkers	Results				Ref.
					Linear range	Limit of detection	Recovery	Relative standard deviation	
NaYF <sub>4</sub> :Yb,Tm	PEG; Streptavidin	78.7	-	HER2	SBR=319; UCNP labeling compatible with H&E staining; Signal stable within 20 min;				[245]
NaYF <sub>4</sub> :Yb,Tm	PEG; Streptavidin	44.2±4.0	-	HER2	SBR=319				[246]
NaGdF <sub>4</sub> :Yb,Er@NaGdF <sub>4</sub>	NPTAT-doped SiO <sub>2</sub> ; Anti-PR antibody	39.2±4.1	-	PR	Excellent correlation with WB/IHC; More accurate low-level protein quantification vs. IHC; Enabled multiplex in situ biodetection;				[247]
NaGdF <sub>4</sub> :Yb,Tm@NaGdF <sub>4</sub>	SiO <sub>2</sub> ; NPTAT-doped SiO <sub>2</sub> ; Anti-ER	38.1±4.1	-	ER					

NaYbF <sub>4</sub> :Er@NaYF <sub>4</sub>	antibody SiO <sub>2</sub> ; Rhodamine B isothiocyanate-doped SiO <sub>2</sub> ; Anti-HER2 antibody;	24.2 2±1.50	-	HER2					
NaYbF <sub>4</sub> :Er	Aptamer	6–7	-	VEGF	50–200 0 pM	6 pM	98.0%– 113.0%	2.9%–3.6%	[248]
NaYbF <sub>4</sub> :Er	PAA; Aptamer; PAA;	50	-	VEGF <sub>165</sub>	0.1–16 ng/mL	0.1 ng/mL	96.5%– 112%	<6.2%	[249]
NaYF <sub>4</sub> :Yb, Tm	6-Carboxyfluorescein; Aptamer; PEI;	43.4	-	CA15-3	0.01–1 50 U/mL	4.5 mU/mL	98.0%– 105.0%	<5%	[253]
NaYF <sub>4</sub> :Yb, Tm	Anti-CA125 antibody;	20	17	CA125	5–100 ng/mL	120 pg/mL	-	-	[255]
NaYF <sub>4</sub> :Yb, Er	PAA; Aptamer;	41.7 ±3.6	-	CA125	0.01–1 00 U/mL	9 mU/mL	98%–1 02%	<6%	[256]
NaYF <sub>4</sub> :Yb, Er	PAA; Anti-CEA antibody;	55	-	CEA	0.5–30 ng/mL	0.36 ng/mL	-	-	[259]
NaYF <sub>4</sub> :Yb, Tm	PDA	36	-13.1	CEA	2–200 ng/mL	0.1 ng/mL	96.7%– 104.8%	<5%	[260]
NaYF <sub>4</sub> :Yb, Er	PAA; Aptamer;	52±1 1	-	CEA	0.05–1 0 ng/mL	0.008 ng/mL	92.0%– 110.0%	1.4%–6%	[261]
NaYF <sub>4</sub> :Yb, Tm	PDA	-	-	CEA	0.1–10 0 ng/mL	0.031 ng/mL	92.6%– 107.0%	1.0%–3.0%	[262]
NaYF <sub>4</sub> :Yb, Tm	TiO <sub>2</sub>	150	-	CEA	0.01–4 0 ng/mL	3.6 pg/mL	-	8.9%	[263]
NaErF <sub>4</sub> :Tm@NaYF <sub>4</sub> @NaNdF <sub>4</sub>	PAA; G-quadruplex DNAzyme; cDNA;	399.9	-14.16	CEA	50–200 0 ng/mL	0.910 pg/mL	94.12% –103.9 2%	2.12%–5.33 %	[264]
NaYF <sub>4</sub> :Yb, Er	cDNA	30	-35.6	CEA	0.02–6.0 0 ng/mL (0.1–	65 fM (0.013 ng/mL)	-	-	[265]

NaGdF <sub>4</sub> :Yb,Er	PEG; Thiolated ssDNA;	10±3	-	TK1 mRNA	30 pM) 1.17–6 5.21 fmol/10 μg	0.67 fmol/10 μg	-	-	[266]
				microRNA-21	0.043– 41.25 fmol/10 μg	0.019 fmol/10 μg	-	-	
NaYF <sub>4</sub> :Yb,Er	PEI; Molecular beacon;	-	-	TK1 mRNA	0–100× 10 <sup>-9</sup> M	1.1×10 <sup>-9</sup> M	-	-	[267]
NaGdF <sub>4</sub> :Yb,Er	PEG; Cell-penetrating peptide;	-	-	microRNA-21	0.073– 43.65 fmol/10 μg	0.03 fmol/10 μg	-	-	[268]
NaYF <sub>4</sub> @NaYF <sub>4</sub> :Yb,Er	PEG; Anchor DNA; Glycerol phosphate disodium salt hydrate;	-	-	microRNA-21	10×10 <sup>-1</sup> 5- 10×10 <sup>-1</sup> <sup>1</sup> M	0.74×10 <sup>-15</sup> M	95.0%– 96.7%	-	[269]
NaYF <sub>4</sub> :Yb:Tm@NaYF <sub>4</sub>	Plasmid DNA	46.8 3	-12.0	ctDNA (KRAS)	5–1000 pM	6.30 pM	93.14% –98.51 %	2.02%–4.80 %	[271]
NaYF <sub>4</sub> :Tm,Yb@NaYF <sub>4</sub>	SiO <sub>2</sub> ; DNA probe;	60	-	ctDNA (PIK3CA E542K)	1–500 fM	1 nM	-	-	[272]

PEG: polyethylene glycol; PAA: polypropylene acid; SBR: signal-to-background ratio; IHC: immunohistochemistry; PEI: polyethyleneimine; PDA: polydopamine; WB: western blotting; NPTAT: nickel (II) phthalocyanine-tetrasulfonic acid tetrasodium salt.

Table 6. Applications of UCNP s in BC phototherapy.

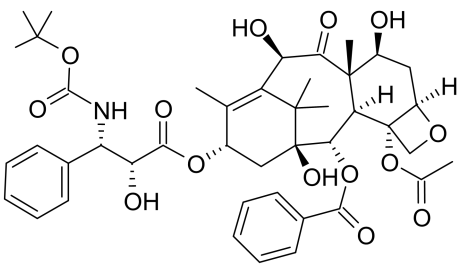
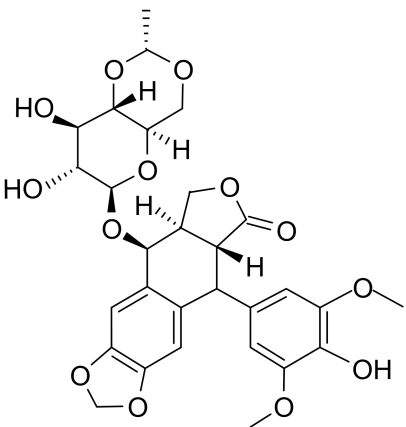
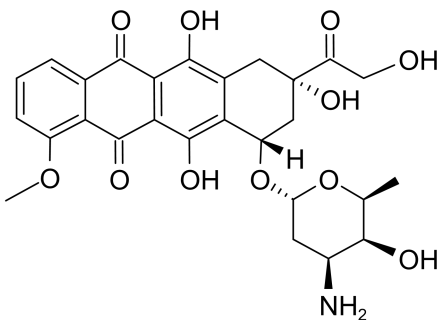
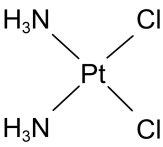
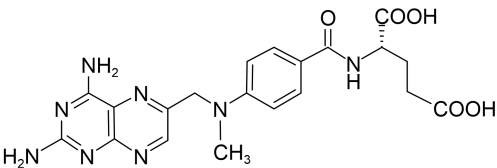
UCNPs	Beneficial molecules	Application		Results	Ref.
NaYF <sub>4</sub> :Yb,Tm@NaYF <sub>4</sub>	Riboflavin	PDT	In SK-BR-3 xenograft mice, tumor volume inhibition rate reached 90% post-PDT; Treatment depth achieved 4–6 mm;		[280]
NaYF <sub>4</sub> :Yb,Er,Gd@NaYF <sub>4</sub>	RB	PDT	Under 980 nm light irradiation, SK-BR-3 cell death rate 67%; Dark toxicity 5%;		[388]

NaYF <sub>4</sub> :Yb,Er/ Tm@NaYF <sub>4</sub> : Yb@NaYF <sub>4</sub>	Protoporphyrin IX	PDT	Experimental group tumor volume decreased 50% vs. control on day 15	[281]
NaYF <sub>4</sub> :Yb,Er @NaYF <sub>4</sub>	KillerRed	PDT	Achieved 70% PDT efficiency through 1 cm tissue; KillerRed showed 7% under identical conditions;	[282]
NaYF <sub>4</sub> :Yb,Er	ZnPc	PDT	After 5 min 975 nm irradiation, SK-BR-3 cell viability reduced to 21.8%; MCF-7 cells showed slight decrease under identical conditions;	[216]
NaYF <sub>4</sub> :Yb,Tm	Graphene quantum dots	PDT	20 days post-treatment, 4T1 tumor inhibition rate reached 75.3%	[283]
NaGdF <sub>4</sub> :Yb,Er @NaGdF <sub>4</sub> :Yb, Nd@NaGdF <sub>4</sub>	Porphyrins	PDT	Post-PDT, 4T1 cell viability reduced to 27.0%; Suppressed tumor growth over 14 days; 808 nm laser mitigated thermal damage risk during PDT;	[284]
NaY (Mn) F <sub>4</sub> :Yb,Er	Chlorin e6	PDT	4T1 relative tumor volume increased to 2–3 times initial at 14 days, significantly lower than control group	[285]
NaYF <sub>4</sub> :Yb,Er	TTD	PDT	<sup>1</sup> O <sub>2</sub> yield was 36.4%, higher than mTHPC (31%); Targeted MDA-MB-231 cells with high integrin αβ3 expression via cRGD peptide; After NIR irradiation, cell viability decreased to 28.3%, with negligible toxicity to MCF-7 and NIH 3T3 cells;	[286]
NaYF <sub>4</sub> :Yb,Er @NaLuF <sub>4</sub>	ZnPc	PDT	NIR irradiation reduced 4T1 viability to 38%; 12-day treatment significantly inhibited tumor growth; Material degraded to <6 nm NPs in vivo, excreted renally;	[152]
NaYF <sub>4</sub> :Yb,Er	Gold shell	PTT	UCL/MRI dual-modal imaging enabled; With magnetic field near tumor, NP accumulation increased 8-fold vs. no field; Magnetically targeted NPs combined with 808 nm laser eliminated 4T1 tumor completely;	[294]
NaYF <sub>4</sub> :Yb,Er	AuNPs	PTT	With 5-min NIR irradiation, MCF-7 cell viability reduced >60%. The 525/545 nm green emission ratio allowed ratiometric temperature sensing (25–50 °C) for monitoring;	[295]
NaGdF <sub>4</sub> :Yb:Er	RB; IR825;	PTT-PDT	UCL/MRI dual-modal imaging enabled; Combined therapy significantly inhibited tumor growth;	[297]
NaYF <sub>4</sub> @NaY F <sub>4</sub> :Yb,Er@Na YF <sub>4</sub> :Yb,Nd@ NaYF <sub>4</sub>	RB; AuNPs;	PTT-PDT	Combined therapy reduced the viability of MCF-7 cells to less than 40%	[298]
NaYF <sub>4</sub> :Yb,Er, Nd@NaYF <sub>4</sub> :N d	AgBiS <sub>2</sub>	PTT-PDT	160 µg/mL NPs combined with 808 nm laser irradiation (3 min) induced near-zero 4T1 cell survival; 0.5 W/cm <sup>2</sup> 808 nm laser (10 min) raised tumor temperature to 56.3 °C, sustaining tumor inhibition for 14 days;	[299]

RB: rose bengal; ZnPc: zinc phthalocyanine; TTD: 2-(2,6-bis ((E)-4-(phenyl  
(40-(1,2,2-triphenylvinyl)-[1,10-biphenyl]-4-yl) amino) styryl)-4H-pyran-4-ylidene)

malononitrile; mTHPC: meso-tetrakis (m-hydroxyphenyl) chlorin.

Table 7. Clinical uses of anti-BC drugs.

Drugs	Chemical Structure	Ref.
Hydrophobic drugs		
Docetaxel		[389]
Etoposide		[390]
Doxorubicin		[391]
Cisplatin		[392]
Methotrexate		[393]

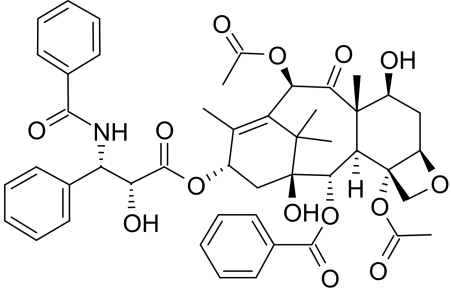
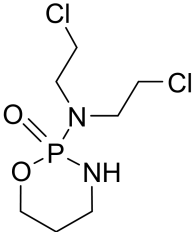
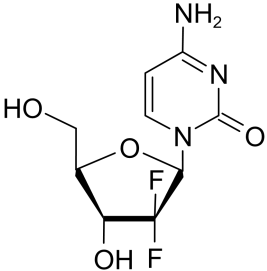
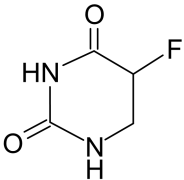
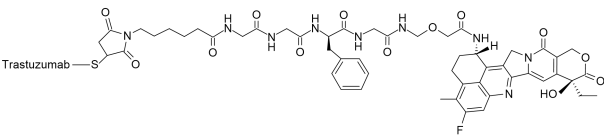
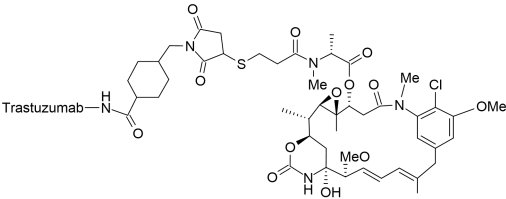
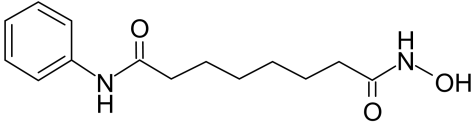
Paclitaxel		[394]
Hydrophilic drugs		
Cyclophosphamide		[395]
Gemcitabine		[396]
5-Fluorouracil		[397]
Bevacizumab	Monoclonal antibody	[398]
Pembrolizumab	Monoclonal antibody	[399]
Trastuzumab deruxtecan		[400]
Trastuzumab emtansine		[401]
Vorinosta		[402]

Table 8. Applications of UCNPs in smart drug/gene delivery.

UCNPs	Agents	Loading method	Loading capacity	Stimulus type	Responder	Results	Ref.
NaYF <sub>4</sub> :Yb, Tm@NaLuF <sub>4</sub>	Chlorambucil	Physical absorption	49%	980 nm light	Amino-coumarin derivative	In dark enzymatic physiological environment, chlorambucil released only 3% within 48 h; With 980 nm light irradiation, over 50% was released within 6 hours, peaking at 68% at 15 h;	[308]
LiYF <sub>4</sub> :Tm, Yb	DOX	Coordination	Approximately 1500 molecules of doxorubicin were loaded onto each NP	980 nm light	Nitroveratryl	In dark, ultrasound and centrifugation for 60 min induced negligible DOX release; 980 nm light irradiation for 60 min triggered 40% DOX release;	[309]
NaYF <sub>4</sub> :Tm, Yb@NaYF <sub>4</sub>	DOX	Physical absorption	4.75%	980 nm light	2-Diazo-1, 2-naphthoquinones	In dark, cumulative DOX release remained below 6%; With 980 nm light at 1.0 W/cm <sup>2</sup> for 60 min, the release reached 30%, and at 1.5 W/cm <sup>2</sup> , it reached 40%;	[310]
NaYF <sub>4</sub> :Tm, Yb@NaYF <sub>4</sub>	DOX	Physical absorption	-	980 nm light	Spiropyran group	In dark, cumulative DOX release stayed below 5%; 980 nm light induced 80% drug release within 24 h;	[311]
NaYbF <sub>4</sub> :Tm@NaYbF <sub>4</sub> :Yb,Er	Roussin's black salt	Physical absorption	10%	980 nm light	Roussin's black salt	Burst NO release achieved	[312]
NaYbF <sub>4</sub> :Tm@NaYF <sub>4</sub> :Yb,Nd@NaYF <sub>4</sub>	Roussin's black salt	Physical absorption	11%	808 nm light	Roussin's black salt	Burst NO release achieved	[313]
NaYF <sub>4</sub> :Yb, Tm	Plasmid DNA; siRNA;	Physical absorption	0.7%	980 nm light	4,5-dimethoxy-2-nitroacetophenone	Spatiotemporal control of GFP expression achieved	[314]



NaYF <sub>4</sub> :Yb, Tm	siRNA	Physical absorption	0.7%	980 nm light	Photocage d linker	Spatiotemporal suppression of EGFP expression achieved	[315]
NaYF <sub>4</sub> :Yb, Tm@NaYF <sub>4</sub>	Bcl-2 antisense oligonucleo tides	Physical absorption	Approximately 38 DNA probes containing photocle avable groups were loaded on each NP	980 nm light	Photoclea vable linker	Bcl-2 mRNA expression in HeLa cells reduced by 50%	[316]
NaYF <sub>4</sub> :Yb, Er	DOX	Physical absorption	14.2%	pH	mSiO <sub>2</sub>	DOX release accelerated at pH 5.0, releasing >55% within 96 h; At pH 7.4, release was 35.2%;	[403]
NaYF <sub>4</sub> :Yb, Tm	DOX	Physical absorption	60%	pH	PEG	At pH 5.8, DOX cumulative release 60% in 10 h; At pH 7.4, release <20%;	[380]

NaYF <sub>4</sub> :Yb, Tm@NaGd F <sub>4</sub>	Plumbagin	Physical absorption	22.63 ± 1.28%	pH	PAA	At pH 7.4, plumbagin release was 4.32% in 24 h, with negligible release in 96 h; At pH 5.86 and 4.01, 24 h release was 36.37% and 85.72%, stabilizing to 39.79% and 86.17% at 96 h, respectively;	[320]
NaYF <sub>4</sub> :Yb, Er	DOX	Physical absorption	58.7%	pH	UIO-66(NH <sub>2</sub> )	At pH 7.4, 30% and 40% of DOX were released in 12 and 24 h, respectively; At pH 5.5, 65% and 72% were released over the same times;	[222]
NaGaF <sub>4</sub> :Yb, Tm@NaGaF <sub>4</sub> : Yb,Er@NaGaF <sub>4</sub>	DOX	Physical absorption	7.9%	pH	Metal-phenolic networks	At pH 5.0, cumulative DOX release reached 51.1%; At pH 7.4, it was only 3.2%;	[321]
NaYF <sub>4</sub> :Yb, Tm	DOX	Physical absorption	7.23%	980 nm light; pH;	O-nitrobenzyl; Poly(methacrylic acid);	Under visible light at pH 7.4, cumulative DOX release was 8.35% after 5 h; Under 980 nm light irradiation and acidic conditions, it reached 59.5% in the same time;	[322]
NaYF <sub>4</sub> :Yb, Er@NaYF <sub>4</sub>	DOX; Fe <sup>2+</sup> ;	Physical absorption	21.02% (DOX); 4.99% (Fe <sup>2+</sup> );	980 nm light; pH;	Bis-(alkylthio) alkene; Bovine serum albumin;	At pH 7.4, 6.39% DOX released in 48 h; At pH 5.6, 35.76% released in same time; Fe <sup>2+</sup> release rate significantly accelerated under 980 nm laser irradiation;	[323]

NaYF <sub>4</sub> :Yb, Er	Camptothecin	Self-assembly	11.5%	980 nm light; GSH;	Eosin Y; Disulfide bond;	NIR light-activated photochemical internalization promoted vesicle escape to cytoplasm, enabling GSH-triggered camptothecin release	[326]
NaYF <sub>4</sub> :Yb, Er@NaGdF <sub>4</sub>	DOX	Physical absorption	8.7%	980 nm light; GSH;	CuS; Disulfide bond;	At pH 5.0 with 10 mM GSH, DOX release reached 76% in 48 h under laser irradiation; Without laser, it was 71%;	[327]
NaGdF <sub>4</sub> :Yb, Er@NaGdF <sub>4</sub> :Nd,Yb	DOX	Physical absorption	54.3%	808 nm light; pH; GSH;	Polyoxometalate; Mn-doped silica;	DOX release rate significantly increased under combined acidic, reductive conditions and NIR light irradiation	[328]
Y <sub>2</sub> O <sub>3</sub> :Yb,Er @Y <sub>2</sub> O <sub>3</sub> :Yb	DOX	Physical absorption	6.89%	Temperature; pH;	Poly (N-isopropylacrylamide-co-methacrylic acid)	At pH 7.4, DOX release in 36 h was 12.5%; At pH 4.0, it reached 73.6%; At 25 °C, release was 8.1% in 36 h; At 50 °C, it increased to 51.4%;	[329]
NaYF <sub>4</sub> :Yb, Er	DOX	Physical absorption	-	Temperature; pH;	Poly (N-isopropylacrylamide-co-methacrylic acid)	At low temperature/high pH, DOX showed low release; At higher temperature/lower pH, release increased significantly;	[330]

NaYF <sub>4</sub> :Yb, Er@NaYF <sub>4</sub>	DOX	Covalent bonding	4.36 ± 0.5%	Enzyme; pH;	Succinic acid-glyci ne-phenyl alanine-le ucine-glyc ine linker	DOX release significantly enhanced under combined enzymatic and acidic conditions	[331]
--	-----	---------------------	----------------	----------------	---	---	-------

siRNA: small interfering RNA; GFP: green fluorescent protein; EGFP: enhanced green fluorescent protein; mRNA: messenger RNA; PEG: polyethylene glycol; PAA: polyacrylic acid.

Table 9. Summary of UCNPs combined with immunotherapy.

UCNPs	Immunotherapy agents	Results	Ref.
NaYF <sub>4</sub> :Yb, Er,Gd	Ovalbumin	Highly sensitive in vivo UCL imaging for DC migration tracking achieved; UCNP-based DC vaccine induced strong antigen-specific immune responses;	[335]
NaYF <sub>4</sub> :Yb, Tm@NaYF <sub>4</sub>	Zn <sub>x</sub> Mn <sub>1-x</sub> S	Significant inhibition of primary 4T1 tumor and lung metastasis growth	[382]
NaYF <sub>4</sub> :Yb, Er	MC540; Ovalbumin/Tumor cell fragment;	More effective tumor growth inhibition and survival prolongation by nanovaccine vs. PDT/immunotherapy alone	[337]
NaYF <sub>4</sub> :Yb, Er	DOX; RB;	Combination therapy induced 73.1% 4T1 cell apoptosis, significantly higher than single PDT (47.2%) or chemotherapy (24.5%); In TNBC mice, intravenous nanocarriers with NIR irradiation inhibited orthotopic tumor growth, suppressed lung metastasis, and prolonged survival;	[338]
K <sub>3</sub> ZrF <sub>7</sub> :Yb, Er	-	Biodegradable NPs released ions in cancer cells to induce pyroptosis, enhancing anti-tumor immunity and inhibiting tumor growth and lung metastasis	[339]
NaGdF <sub>4</sub> :Yb, Er	PDA; Ce6; α-PD-1 antibody;	Primary tumor ablation; Antitumor immunity activation; BC metastasis inhibition;	[340]
NaGdF <sub>4</sub> :Yb, Er@NaYF <sub>4</sub> @NaYF <sub>4</sub> :Yb, Tm@NaYF <sub>4</sub> :Nd@NaYF <sub>4</sub>	RB; α-PD-1 antibody;	Significant inhibition of primary tumors; Abscopal effect on non-irradiated distant tumors, suppressing growth;	[341]
GdOF:Yb,E r	AuNPs; Anti-CTLA-4 antibody;	Combined therapy showed 90% 4T1 tumor volume reduction vs. control; Efficacy superior to single PDT or immunotherapy;	[342]
NaYF <sub>4</sub> :Yb,	DOX; RB; Anti-CD73	Significant 4T1 tumor growth inhibition (93.4%); Reduction	[343]



8. Li H-H, Wang Y-K, Liao L-S. Near-infrared luminescent materials incorporating rare earth/transition metal ions: from materials to applications. *Adv Mater Deerfield Beach Fla.* 2024; 36: e2403076.
9. Li C, Chen G, Zhang Y, Wu F, Wang Q. Advanced fluorescence imaging technology in the near-infrared-II window for biomedical applications. *J Am Chem Soc.* 2020; 142: 14789–804.
10. Anderson RR, Parrish JA. The optics of human skin. *J Invest Dermatol.* 1981; 77: 13–9.
11. Smith AM, Mancini MC, Nie S. Bioimaging: second window for in vivo imaging. *Nat Nanotechnol.* 2009; 4: 710–1.
12. Fan Y, Zhang F. A new generation of NIR-II probes: lanthanide-based nanocrystals for bioimaging and biosensing. *Adv Opt Mater.* 2019; 7: 1801417.
13. Stolik S, Delgado JA, Pérez A, Anasagasti L. Measurement of the penetration depths of red and near infrared light in human ‘ex vivo’ tissues. *J Photochem Photobiol B.* 2000; 57: 90–3.
14. Larnac E, Méthot S, Pelchat F, Millette M-A, Montoni A, Salesse C, et al. Synergistic toxicity of pollutant and ultraviolet exposure from a mitochondrial perspective. *Int J Mol Sci.* 2024; 25: 9146.
15. del Valle CA, Hirsch T, Marín MJ. Recent advances in near infrared upconverting nanomaterials for targeted photodynamic therapy of cancer. *Methods Appl Fluoresc.* 2022; 10: 34003.
16. Genina EA, Lazareva EN, Surkov YI, Serebryakova IA, Shushunova NA. Optical parameters of healthy and tumor breast tissues in mice. *J Biophotonics.* 2024; 17: e202400123.
17. Tromberg BJ, Shah N, Lanning R, Cerussi A, Espinoza J, Pham T, et al. Non-invasive in vivo characterization of breast tumors using photon migration spectroscopy. *Neoplasia N Y N.* 2000; 2: 26–40.
18. Jacques SL. Optical properties of biological tissues: a review. *Phys Med Biol.* 2013; 58: R37.
19. Peters VG, Wyman DR, Patterson MS, Frank GL. Optical properties of normal and diseased human breast tissues in the visible and near infrared. *Phys Med Biol.* 1990; 35: 1317.
20. Chintamaneni PK, Nagasen D, Babu KC, Mourya A, Madan J, Srinivasarao DA, et al. Engineered upconversion nanocarriers for synergistic breast cancer imaging and therapy: current state of art. *J Controlled Release.* 2022; 352: 652–72.

21. Zheng B, Fan J, Chen B, Qin X, Wang J, Wang F, et al. Rare-earth doping in nanostructured inorganic materials. *Chem Rev.* 2022; 122: 5519–603.
22. Zhao H, Li Y, Zhang X, Wu K, Lv J, Chen C, et al. Orthogonal excitations of lanthanide nanoparticle up/down conversion emissions via switching NIR lights for in-vivo theranostics. *Biomaterials.* 2022; 291: 121873.
23. Bloembergen N. Solid state infrared quantum counters. *Phys Rev Lett.* 1959; 2: 84–5.
24. Auzel F. History of upconversion discovery and its evolution. *J Lumin.* 2020; 223: 116900.
25. Ovsyankin VV, Feofilov PP. Mechanism of summation of electronic excitations in activated crystals. *Sov J Exp Theor Phys Lett.* 1966; 3: 322.
26. Ballato J, Lewis JS, Holloway P. Display applications of rare-earth-doped materials. *MRS Bull.* 1999; 24: 51–6.
27. Zijlmans HJMAA, Bonnet J, Burton J, Kardos K, Vail T, Niedbala RS, et al. Detection of cell and tissue surface antigens using up-converting phosphors: a new reporter technology. *Anal Biochem.* 1999; 267: 30–6.
28. Zhou J, Liu Q, Feng W, Sun Y, Li F. Upconversion luminescent materials: advances and applications. *Chem Rev.* 2015; 115: 395–465.
29. Li F, Tu L, Zhang Y, Huang D, Liu X, Zhang X, et al. Size-dependent lanthanide energy transfer amplifies upconversion luminescence quantum yields. *Nat Photonics.* 2024; 18: 440–9.
30. Wang J, Sheng T, Zhu X, Li Q, Wu Y, Zhang J, et al. Spectral engineering of lanthanide-doped upconversion nanoparticles and their biosensing applications. *Mater Chem Front.* 2021; 5: 1743–70.
31. Liang G, Wang H, Shi H, Wang H, Zhu M, Jing A, et al. Recent progress in the development of upconversion nanomaterials in bioimaging and disease treatment. *J Nanobiotechnology.* 2020; 18: 154.
32. Zheng X, Kankala RK, Liu C-G, Wang S-B, Chen A-Z, Zhang Y. Lanthanides-doped near-infrared active upconversion nanocrystals: upconversion mechanisms and synthesis. *Coord Chem Rev.* 2021; 438: 213870.
33. Zheng W, Huang P, Tu D, Ma E, Zhu H, Chen X. Lanthanide-doped upconversion nano-bioprobes: electronic structures, optical properties, and biodetection. *Chem Soc Rev.* 2015; 44: 1379–415.
34. Yin X, Xu W, Zhu G, Ji Y, Xiao Q, Dong X, et al. Towards highly efficient NIR II response up-conversion phosphor enabled by long lifetimes of  $\text{Er}^{3+}$ . *Nat Commun.* 2022; 13: 6549.
35. Dong H, Sun L-D, Yan C-H. Energy transfer in lanthanide upconversion studies for

- extended optical applications. *Chem Soc Rev*. 2015; 44: 1608–34.
36. Menyuk N, Dwight K, Pierce JW. NaYF<sub>4</sub>: Yb,Er—an efficient upconversion phosphor. *Appl Phys Lett*. 1972; 21: 159–61.
  37. Qin W-P, Liu Z-Y, Sin C-N, Wu C-F, Qin G-S, Chen Z, et al. Multi-ion cooperative processes in Yb<sup>3+</sup> clusters. *Light Sci Appl*. 2014; 3: e193–e193.
  38. Wen S, Zhou J, Zheng K, Bednarkiewicz A, Liu X, Jin D. Advances in highly doped upconversion nanoparticles. *Nat Commun*. 2018; 9: 2415.
  39. Fu X, Fu S, Lu Q, Zhang J, Wan P, Liu J, et al. Excitation energy mediated cross-relaxation for tunable upconversion luminescence from a single lanthanide ion. *Nat Commun*. 2022; 13: 4741.
  40. Chen D, Liu L, Huang P, Ding M, Zhong J, Ji Z. Nd<sup>3+</sup>-sensitized Ho<sup>3+</sup> single-band red upconversion luminescence in core-shell nanoarchitecture. *J Phys Chem Lett*. 2015; 6: 2833–40.
  41. Chivian JS, Case WE, Eden DD. The photon avalanche: a new phenomenon in Pr<sup>3+</sup>-based infrared quantum counters. *Appl Phys Lett*. 1979; 35: 124–5.
  42. da Silva JF, da Silva RF, Santos EP, Maia LJQ, Moura AL. Photon-avalanche-like upconversion in NdAl<sub>3</sub>(BO<sub>3</sub>)<sub>4</sub> nanoparticles excited at 1064nm. *Appl Phys Lett*. 2020; 117: 151102.
  43. Marciniak L, Bednarkiewicz A, Elzbieciak K. NIR–NIR photon avalanche based luminescent thermometry with Nd<sup>3+</sup> doped nanoparticles. *J Mater Chem C*. 2018; 6: 7568–75.
  44. Wen H, Zhu H, Chen X, Hung TF, Wang B, Zhu G, et al. Upconverting near-infrared light through energy management in core-shell-shell nanoparticles. *Angew Chem-Int Ed*. 2013; 52: 13419–23.
  45. Zhao J, Lu Z, Yin Y, McRae C, Piper JA, Dawes JM, et al. Upconversion luminescence with tunable lifetime in NaYF<sub>4</sub>:Yb,Er nanocrystals: role of nanocrystal size. *Nanoscale*. 2013; 5: 944–52.
  46. Liang L, Teh DBL, Dinh N-D, Chen W, Chen Q, Wu Y, et al. Upconversion amplification through dielectric superlensing modulation. *Nat Commun*. 2019; 10: 1391.
  47. Rodríguez-Sevilla P, Zhang Y, de Sousa N, Marqués MI, Sanz-Rodríguez F, Jaque D, et al. Optical torques on upconverting particles for intracellular microrheometry. *Nano Lett*. 2016; 16: 8005–14.
  48. Wang L, Xue X, Shi F, Zhao D, Zhang DM, Zheng K, et al. Ultraviolet and violet upconversion fluorescence of europium (III) doped in YF<sub>3</sub> nanocrystals. *Opt Lett*. 2009; 34:



2781–3.

49. Chen G, Ågren H, Ohulchanskyy TY, Prasad PN. Light upconverting core-shell nanostructures: nanophotonic control for emerging applications. *Chem Soc Rev.* 2015; 44: 1680–713.
50. Homann C, Krukewitt L, Frenzel F, Grauel B, Würth C, Resch-Genger U, et al. NaYF<sub>4</sub>:Yb,Er/NaYF<sub>4</sub> core/shell nanocrystals with high upconversion luminescence quantum yield. *Angew Chem Int Ed.* 2018; 57: 8765–9.
51. Wang Y-F, Sun L-D, Xiao J-W, Feng W, Zhou J-C, Shen J, et al. Rare-earth nanoparticles with enhanced upconversion emission and suppressed rare-earth-ion leakage. *Chem Weinh Bergstr Ger.* 2012; 18: 5558–64.
52. Zuo J, Wang W, Zhang D, Wang X, Ma Y, Li P, et al. Ultra-sensitive water detection based on NaErF<sub>4</sub>@NaYF<sub>4</sub> high-level-doping upconversion nanoparticles. *Appl Surf Sci.* 2022; 575: 151701.
53. Li K, Li D, Jia M, Guo D, Dai M, Zhao J, et al. Li-based nanoprobe with boosted photoluminescence for temperature visualization in NIR imaging-guided drug release. *Nano Lett.* 2025; 25: 776–85.
54. Chen J, Gao Y, Wang C, Yin Y, Song J, Zeng X, et al. Effective regulation of upconversion luminescence in NaErF<sub>4</sub> and NaErF<sub>4</sub>@SiO<sub>2</sub> core-shell particles. *Ceram Int.* 2022; 48: 14315–22.
55. Wang X, Valiev RR, Ohulchanskyy TY, Ågren H, Yang C, Chen G. Dye-sensitized lanthanide-doped upconversion nanoparticles. *Chem Soc Rev.* 2017; 46: 4150–67.
56. Wang L, Guo S, Liu D, He J, Zhou J, Zhang K, et al. Plasmon-enhanced blue upconversion luminescence by indium nanocrystals. *Adv Funct Mater.* 2019; 29: 1901242.
57. Wang F, Deng R, Wang J, Wang Q, Han Y, Zhu H, et al. Tuning upconversion through energy migration in core-shell nanoparticles. *Nat Mater.* 2011; 10: 968–73.
58. Jia H, Li D, Zhang D, Dong Y, Ma S, Zhou M, et al. High color-purity red, green, and blue-emissive core-shell upconversion nanoparticles using ternary near-infrared quadrature excitations. *ACS Appl Mater Interfaces.* 2021; 13: 4402–9.
59. Xu D, Xu J, Shang X, Yu S, Zheng W, Tu D, et al. Boosting the energy migration upconversion through inter-shell energy transfer in Tb<sup>3+</sup>-doped sandwich structured nanocrystals. *CCS Chem.* 2022; 4: 2031–42.
60. Zhu X, Zhang J, Liu J, Zhang Y. Recent progress of rare-earth doped upconversion nanoparticles: synthesis, optimization, and applications. *Adv Sci.* 2019; 6: 1901358.
61. Zhang Y-W, Sun X, Si R, You L-P, Yan C-H. Single-crystalline and monodisperse LaF<sub>3</sub>

- triangular nanoplates from a single-source precursor. *J Am Chem Soc.* 2005; 127: 3260–1.
62. Yi GS, Chow GM. Synthesis of hexagonal-phase NaYF<sub>4</sub>:Yb,Er and NaYF<sub>4</sub>:Yb,Tm nanocrystals with efficient up-conversion fluorescence. *Adv Funct Mater.* 2006; 16: 2324–9.
  63. Mai H-X, Zhang Y-W, Si R, Yan Z-G, Sun L, You L-P, et al. High-quality sodium rare-earth fluoride nanocrystals: controlled synthesis and optical properties. *J Am Chem Soc.* 2006; 128: 6426–36.
  64. Mai H-X, Zhang Y-W, Sun L-D, Yan C-H. Size- and phase-controlled synthesis of monodisperse NaYF<sub>4</sub>:Yb,Er nanocrystals from a unique delayed nucleation pathway monitored with upconversion spectroscopy. *J Phys Chem C.* 2007; 111: 13730–9.
  65. Liu D, Xu X, Du Y, Qin X, Zhang Y, Ma C, et al. Three-dimensional controlled growth of monodisperse sub-50 nm heterogeneous nanocrystals. *Nat Commun.* 2016; 7: 10254.
  66. Liu Z, Pu F, Huang S, Yuan Q, Ren J, Qu X. Long-circulating Gd<sub>2</sub>O<sub>3</sub>:Yb<sup>3+</sup>, Er<sup>3+</sup> up-conversion nanoprobe as high-performance contrast agents for multi-modality imaging. *Biomaterials.* 2013; 34: 1712–21.
  67. Du Y-P, Zhang Y-W, Yan Z-G, Sun L-D, Yan C-H. Highly luminescent self-organized sub-2-nm EuOF nanowires. *J Am Chem Soc.* 2009; 131: 16364–5.
  68. Du Y-P, Zhang Y-W, Sun L-D, Yan C-H. Atomically efficient synthesis of self-assembled monodisperse and ultrathin lanthanide oxychloride nanoplates. *J Am Chem Soc.* 2009; 131: 3162–3.
  69. Shi Y, Li J, Cui W, Peng Y, Huang Y, Chen L. Solvothermal synthesis and upconversion properties in Yb<sup>3+</sup>/Ln<sup>3+</sup> (Ln<sup>3+</sup>=Er<sup>3+</sup>/ Ho<sup>3+</sup>/ Tm<sup>3+</sup>) codoped In<sub>2</sub>O<sub>3</sub> nanoparticles with fine stability. *Opt Mater.* 2021; 121: 111601.
  70. Wang L, Li Y. Controlled synthesis and luminescence of lanthanide doped NaYF<sub>4</sub> nanocrystals. *Chem Mater.* 2007; 19: 727–34.
  71. Wang X, Zhuang J, Peng Q, Li Y. Hydrothermal synthesis of rare-earth fluoride nanocrystals. *Inorg Chem.* 2006; 45: 6661–5.
  72. Ren J, Jia G, Guo Y, Wang A, Xu S. Unraveling morphology and phase control of NaLnF<sub>4</sub> upconverting nanocrystals. *J Phys Chem C.* 2016; 120: 1342–51.
  73. Wang X, Zhuang J, Peng Q, Li Y. A general strategy for nanocrystal synthesis. *Nature.* 2005; 437: 121–4.
  74. Stouwdam JW, Van Veggel FCJM. Near-infrared emission of redispersible Er<sup>3+</sup>, Nd<sup>3+</sup>, and Ho<sup>3+</sup> doped LaF<sub>3</sub> nanoparticles. *Nano Lett.* 2002; 2: 733–7.
  75. Yi G, Lu H, Zhao S, Ge Y, Yang W, Chen D, et al. Synthesis, characterization, and

- biological application of size-controlled nanocrystalline NaYF<sub>4</sub>:Yb,Er infrared-to-visible up-conversion phosphors. *Nano Lett.* 2004; 4: 2191–6.
76. Ai Y, Tu D, Zheng W, Liu Y, Kong J, Hu P, et al. Lanthanide-doped NaScF<sub>4</sub> nanoprobes: crystal structure, optical spectroscopy and biodetection. *Nanoscale.* 2013; 5: 6430.
  77. Wang J, Deng R, MacDonald MA, Chen B, Yuan J, Wang F, et al. Enhancing multiphoton upconversion through energy clustering at sublattice level. *Nat Mater.* 2014; 13: 157–62.
  78. Lezhnina MM, Jüstel T, Kätker H, Wiechert DU, Kynast UH. Efficient luminescence from rare-earth fluoride nanoparticles with optically functional shells. *Adv Funct Mater.* 2006; 16: 935–42.
  79. Chen G, Shen J, Ohulchanskyy TY, Patel NJ, Kutikov A, Li Z, et al. ( $\alpha$ -NaYbF<sub>4</sub>:Tm(3+))/CaF<sub>2</sub> core/shell nanoparticles with efficient near-infrared to near-infrared upconversion for high-contrast deep tissue bioimaging. *ACS Nano.* 2012; 6: 8280–7.
  80. Yi G-S, Chow G-M. Water-soluble NaYF<sub>4</sub>:Yb,Er(Tm)/NaYF<sub>4</sub>/polymer core/shell/shell nanoparticles with significant enhancement of upconversion fluorescence. *Chem Mater.* 2007; 19: 341–3.
  81. Huang P, Zheng W, Zhou S, Tu D, Chen Z, Zhu H, et al. Lanthanide-doped LiLuF<sub>4</sub> upconversion nanoprobes for the detection of disease biomarkers. *Angew Chem Int Ed.* 2014; 53: 1252–7.
  82. Liu J, Chen G, Hao S, Yang C. Sub-6 nm monodisperse hexagonal core/shell NaGdF<sub>4</sub> nanocrystals with enhanced upconversion photoluminescence. *Nanoscale.* 2016; 9: 91–8.
  83. Li X, Guo Z, Zhao T, Lu Y, Zhou L, Zhao D, et al. Filtration shell mediated power density independent orthogonal excitations–emissions upconversion luminescence. *Angew Chem Int Ed.* 2016; 55: 2464–9.
  84. Li X, Shen D, Yang J, Yao C, Che RC, Zhang F, et al. Successive layer-by-layer strategy for multi-shell epitaxial growth: shell thickness and doping position dependence in upconverting optical properties. *Chem Mater.* 2013; 25: 106–12.
  85. Dong C, Van Veggel FCJM. Cation exchange in lanthanide fluoride nanoparticles. *ACS Nano.* 2009; 3: 123–30.
  86. Shin J-H, Moon B-S, Kim D-H. Upconversion nanoparticles coated with mesoporous silica nanoshells loaded with dyes for fine-tuned multicolor emission in bioimaging applications. *ACS Appl Nano Mater.* 2022; 5: 3541–7.
  87. Han R, Wu S, Tang K, Hou Y. Facilitating drug release in mesoporous silica coated upconversion nanoparticles by photoacid assistance upon near-infrared irradiation. *Adv Powder Technol.* 2020; 31: 3860–6.

88. Xu J, Liu N, Wu D, Gao Z, Song Y-Y, Schmuki P. Upconversion nanoparticle-assisted payload delivery from TiO<sub>2</sub> under near-infrared light irradiation for bacterial inactivation. *ACS Nano*. 2020; 14: 337–46.
89. Wu S, Wang F, Li Q, Wang J, Zhou Y, Duan N, et al. Photocatalysis and degradation products identification of deoxynivalenol in wheat using upconversion nanoparticles@TiO<sub>2</sub> composite. *Food Chem*. 2020; 323: 126823.
90. Zhou M, Ge X, Ke D-M, Tang H, Zhang J-Z, Calvaresi M, et al. The bioavailability, biodistribution, and toxic effects of silica-coated upconversion nanoparticles in vivo. *Front Chem*. 2019; 7: 218.
91. Zhou J, Liu Z, Li F. Upconversion nanophosphors for small-animal imaging. *Chem Soc Rev*. 2012; 41: 1323–49.
92. Kostiv U, Farka Z, Mickert MJ, Gorris HH, Velychkivska N, Pop-Georgievski O, et al. Versatile bioconjugation strategies of PEG-modified upconversion nanoparticles for bioanalytical applications. *Biomacromolecules*. 2020; 21: 4502–13.
93. Dong A, Ye X, Chen J, Kang Y, Gordon T, Kikkawa JM, et al. A generalized ligand-exchange strategy enabling sequential surface functionalization of colloidal nanocrystals. *J Am Chem Soc*. 2011; 133: 998–1006.
94. Ling H, Guan D, Wen R, Hu J, Zhang Y, Zhao F, et al. Effect of surface modification on the luminescence of individual upconversion nanoparticles. *Small*. 2024; 20: 2309035.
95. Janjua TI, Cao Y, Yu C, Popat A. Clinical translation of silica nanoparticles. *Nat Rev Mater*. 2021; 6: 1072–4.
96. Sivakumar S, Diamante PR, van Veggel FCJM. Silica-coated Ln<sup>3+</sup>-doped LaF<sub>3</sub> nanoparticles as robust down- and upconverting biolabels. *Chem Weinh Bergstr Ger*. 2006; 12: 5878–84.
97. Su Y, Mao Y, Wu S, Liu L, Wen S. Silica coated upconversion nanoplatform for Ag-based chemo-/photodynamic therapy against drug-resistant bacteria. *ACS Appl NANO Mater*. 2023; 6: 8685–94.
98. Lin M, Gao Y, Diefenbach TJ, Shen JK, Hornicek FJ, Park YI, et al. Facial layer-by-layer engineering of upconversion nanoparticles for gene delivery: near-infrared-initiated fluorescence resonance energy transfer tracking and overcoming drug resistance in ovarian cancer. *ACS Appl Mater Interfaces*. 2017; 9: 7941–9.
99. Zhang H, Wang X, Jin R, Su Q. Preparation and applications of polymer-modified lanthanide-doped upconversion nanoparticles. *Giant*. 2022; 12: 100130.
100. Plohl O, Kralj S, Majaron B, Fröhlich E, Ponikvar-Svet M, Makovec D, et al. Amphiphilic coatings for the protection of upconverting nanoparticles against dissolution in aqueous

- media. Dalton Trans. 2017; 46: 6975–84.
101. Jiang G, Pichaandi J, Johnson NJJ, Burke RD, Van Veggel FCJM. An effective polymer cross-linking strategy to obtain stable dispersions of upconverting NaYF<sub>4</sub> nanoparticles in buffers and biological growth media for biolabeling applications. *Langmuir*. 2012; 28: 3239–47.
  102. Märkl S, Schroter A, Hirsch T. Small and bright water-protected upconversion nanoparticles with long-time stability in complex, aqueous media by phospholipid membrane coating. *Nano Lett*. 2020; 20: 8620–5.
  103. Zhao Y, Wei R, Feng X, Sun L, Liu P, Su Y, et al. Dual-mode luminescent nanopaper based on ultrathin g-C<sub>3</sub>N<sub>4</sub> nanosheets grafted with rare-earth upconversion nanoparticles. *ACS Appl Mater Interfaces*. 2016; 8: 21555–62.
  104. Huang M, Wang L, Zhang X, Zhou J, Liu L, Pan Y, et al. Synthesis and characterization of folic acid labeled upconversion fluorescent nanoprobe for in vitro cancer cells targeted imaging. *Nano*. 2017; 12: 1750057.
  105. Lim K, Kim HK, Le XT, Nguyen NT, Lee ES, Oh KT, et al. Highly red light-emitting erbium- and lutetium-doped core-shell upconverting nanoparticles surface-modified with PEG-folic acid/TCPP for suppressing cervical cancer HeLa cells. *Pharmaceutics*. 2020; 12: 1102.
  106. Zhang D, Peng R, Liu W, Donovan MJ, Wang L, Ismail I, et al. Engineering DNA on the surface of upconversion nanoparticles for bioanalysis and therapeutics. *ACS Nano*. 2021; 15: 17257–74.
  107. Malhotra K, Fuku R, Kumar B, Hrovat D, Van Houten J, Piunno PAE, et al. Unlocking long-term stability of upconversion nanoparticles with biocompatible phosphonate-based polymer coatings. *Nano Lett*. 2022; 22: 7285–93.
  108. Liu J, Guo M, Chen C. Nano-bio interactions: a major principle in the dynamic biological processes of nano-assemblies. *Adv Drug Deliv Rev*. 2022; 186: 114318.
  109. Couvreur P. Nanoparticles in drug delivery: past, present and future. *Adv Drug Deliv Rev*. 2013; 65: 21–3.
  110. Shanwar S, Liang L, Nechaev AV, Bausheva DK, Balalaeva IV, Vodenev VA, et al. Controlled formation of a protein corona composed of denatured BSA on upconversion nanoparticles improves their colloidal stability. *Materials*. 2021; 14: 1657.
  111. Liang L, Everest-Dass AV, Kostyuk AB, Khabir Z, Zhang R, Trushina DB, et al. The surface charge of polymer-coated upconversion nanoparticles determines protein corona properties and cell recognition in serum solutions. *Cells*. 2022; 11: 3644.
  112. Nsubuga A, Sgarzi M, Zarschler K, Kubeil M, Hübner R, Steudtner R, et al. Facile

- preparation of multifunctionalisable ‘stealth’ upconverting nanoparticles for biomedical applications. *Dalton Trans.* 2018; 47: 8595–604.
113. Malhotra K, Kumar B, Piuanno PAE, Krull UJ. Cellular uptake of upconversion nanoparticles based on surface polymer coatings and protein corona. *ACS Appl Mater Interfaces.* 2024; 16: 35985–6001.
  114. Zhang L, Cao C, Tay SS, Chen C, Macmillan A, Wen S, et al. Exploring the effect of drug loading on the biological fate of polymer-coated solid nanoparticles. *Chem Mater.* 2023; 35: 4471–88.
  115. Ansari AA, Parchur AK, Li Y, Jia T, Lv R, Wang Y, et al. Cytotoxicity and genotoxicity evaluation of chemically synthesized and functionalized upconversion nanoparticles. *Coord Chem Rev.* 2024; 504: 215672.
  116. Nikolaeva ME, Nechaev AV, Shmendel EV, Akasov RA, Maslov MA, Mironov AF. New cysteine-containing PEG-glycerolipid increases the bloodstream circulation time of upconverting nanoparticles. *Molecules.* 2022; 27: 2763.
  117. Nsubuga A, Zarschler K, Sgarzi M, Graham B, Stephan H, Joshi T. Towards utilising photocrosslinking of polydiacetylenes for the preparation of “stealth” upconverting nanoparticles. [cited 20 June 2025]; Available at: <https://onlinelibrary.wiley.com/doi/10.1002/anie.201811003>
  118. Peng J, Sun Y, Zhao L, Wu Y, Feng W, Gao Y, et al. Polyphosphoric acid capping radioactive/upconverting NaLuF<sub>4</sub>:Yb,Tm,153Sm nanoparticles for blood pool imaging in vivo. *Biomaterials.* 2013; 34: 9535–44.
  119. Chen B-M, Cheng T-L, Roffler SR. Polyethylene glycol immunogenicity: theoretical, clinical, and practical aspects of anti-polyethylene glycol antibodies. *ACS Nano.* 2021; 15: 14022–48.
  120. Xiong L, Yang T, Yang Y, Xu C, Li F. Long-term in vivo biodistribution imaging and toxicity of polyacrylic acid-coated upconversion nanophosphors. *Biomaterials.* 2010; 31: 7078–85.
  121. Zha S, Liu H, Li H, Li H, Wong K-L, All AH. Functionalized nanomaterials capable of crossing the blood-brain barrier. *ACS NANO.* 2024; 18: 1820–45.
  122. Li M, Zou P, Tyner K, Lee S. Physiologically based pharmacokinetic (PBPK) modeling of pharmaceutical nanoparticles. *AAPS J.* 2017; 19: 26–42.
  123. Chen Y, Fei X, Ye C, Qian Q, Ye Z, Xie S, et al. Acute hepatotoxicity of multimodal targeted imaging contrast agent NaLuF<sub>4</sub>:Gd,Yb,Er-PEG/PEI-FA in mice. *J Toxicol Sci.* 2019; 44: 621–32.
  124. Zhu X, Da Silva B, Zou X, Shen B, Sun Y, Feng W, et al. Intra-arterial infusion of

- PEGylated upconversion nanophosphors to improve the initial uptake by tumors in vivo. RSC Adv. 2014; 4: 23580.
125. Lee J, Gordon AC, Kim H, Park W, Cho S, Lee B, et al. Targeted multimodal nano-reporters for pre-procedural MRI and intra-operative image-guidance. Biomaterials. 2016; 109: 69–77.
  126. Swartz MA. The physiology of the lymphatic system. Adv DRUG Deliv Rev. 2001; 50: 3–20.
  127. Helle M, Rampazzo E, Monchanin M, Marchal F, Guillemin F, Bonacchi S, et al. Surface chemistry architecture of silica nanoparticles determine the efficiency of *in vivo* fluorescence lymph node mapping. ACS NANO. 2013; 7: 8645–57.
  128. Sun Y, Peng J, Feng W, Li F. Upconversion nanophosphors NaLuF<sub>4</sub>:Yb,Tm for lymphatic imaging in vivo by real-time upconversion luminescence imaging under ambient light and high-resolution X-ray CT. Theranostics. 2013; 3: 346–53.
  129. Borbás E, Sinkó B, Tsinman O, Tsinman K, Kiserdei É, Démuth B, et al. Investigation and mathematical description of the real driving force of passive transport of drug molecules from supersaturated solutions. Mol Pharm. 2016; 13: 3816–26.
  130. Scott CC, Vacca F, Gruenberg J. Endosome maturation, transport and functions. Semin Cell Dev Biol. 2014; 31: 2–10.
  131. He W, Xing X, Wang X, Wu D, Wu W, Guo J, et al. Nanocarrier-mediated cytosolic delivery of biopharmaceuticals. Adv Funct Mater. 2020; 30: 1910566.
  132. Fu L, Shi B, Wen S, Morsch M, Wang G, Zhou Z, et al. Aspect ratio of PEGylated upconversion nanocrystals affects the cellular uptake In vitro and In vivo. Acta Biomater. 2022; 147: 403–13.
  133. Ansari AA, Parchur AK, Chen G. Surface modified lanthanide upconversion nanoparticles for drug delivery, cellular uptake mechanism, and current challenges in NIR-driven therapies. Coord Chem Rev. 2022; 457: 214423.
  134. Zhang D, Wei L, Zhong M, Xiao L, Li H-W, Wang J. The morphology and surface charge-dependent cellular uptake efficiency of upconversion nanostructures revealed by single-particle optical microscopy. Chem Sci. 2018; 9: 5260–9.
  135. Jin J, Gu Y-J, Man CW-Y, Cheng J, Xu Z, Zhang Y, et al. Polymer-coated NaYF<sub>4</sub>:Yb<sup>3+</sup>, Er<sup>3+</sup> upconversion nanoparticles for charge-dependent cellular imaging. ACS Nano. 2011; 5: 7838–47.
  136. Xing H, Bu W, Ren Q, Zheng X, Li M, Zhang S, et al. A NaYbF<sub>4</sub>: Tm<sup>3+</sup> nanoprobe for CT and NIR-to-NIR fluorescent bimodal imaging. Biomaterials. 2012; 33: 5384–93.

137. Li X, Tang Y, Xu L, Kong X, Zhang L, Chang Y, et al. Dependence between cytotoxicity and dynamic subcellular localization of up-conversion nanoparticles with different surface charges. *RSC Adv.* 2017; 7: 33502–9.
138. Li X, Zhao H, Ji Y, Yin C, Li J, Yang Z, et al. Lysosome-assisted mitochondrial targeting nanoprobe based on dye-modified upconversion nanophosphors for ratiometric imaging of mitochondrial hydrogen sulfide. *ACS Appl Mater Interfaces.* 2018; 10: 39544–56.
139. Rebelo C, Reis T, Guedes J, Saraiva C, Rodrigues AF, Simões S, et al. Efficient spatially targeted gene editing using a near-infrared activatable protein-conjugated nanoparticle for brain applications. *Nat Commun.* 2022; 13: 4135.
140. Chen G, Ma B, Xie R, Wang Y, Dou K, Gong S. NIR-induced spatiotemporally controlled gene silencing by upconversion nanoparticle-based siRNA nanocarrier. *J Control Release Off J Control Release Soc.* 2018; 282: 148–55.
141. Longmire M, Choyke PL, Kobayashi H. Clearance properties of nano-sized particles and molecules as imaging agents: considerations and caveats. *Nanomed.* 2008; 3: 703–17.
142. Choi HS, Liu W, Misra P, Tanaka E, Zimmer JP, Ito Ipe B, et al. Renal clearance of quantum dots. *Nat Biotechnol.* 2007; 25: 1165–70.
143. Ohlson M, Sörensson J, Haraldsson B. A gel-membrane model of glomerular charge and size selectivity in series. *Am J Physiol Renal Physiol.* 2001; 280: F396–405.
144. Kamimura M, Miyamoto D, Saito Y, Soga K, Nagasaki Y. Design of poly(ethylene glycol)/streptavidin coimmobilized upconversion nanophosphors and their application to fluorescence biolabeling. *Langmuir.* 2008; 24: 8864–70.
145. Cao T, Yang Y, Sun Y, Wu Y, Gao Y, Feng W, et al. Biodistribution of sub-10 nm PEG-modified radioactive/upconversion nanoparticles. *Biomaterials.* 2013; 34: 7127–34.
146. Venturoli D, Rippe B. Ficoll and dextran vs. globular proteins as probes for testing glomerular permselectivity: effects of molecular size, shape, charge, and deformability. *Am J Physiol Renal Physiol.* 2005; 288: F605–13.
147. Williams RM, Shah J, Ng BD, Minton DR, Gudas LJ, Park CY, et al. Mesoscale nanoparticles selectively target the renal proximal tubule epithelium. *Nano Lett.* 2015; 15: 2358–64.
148. Tsoi KM, MacParland SA, Ma X-Z, Spetzler VN, Echeverri J, Ouyang B, et al. Mechanism of hard-nanomaterial clearance by the liver. *Nat Mater.* 2016; 15: 1212–21.
149. Fischer HC, Liu L, Pang KS, Chan WCW. Pharmacokinetics of nanoscale quantum dots: In vivo distribution, sequestration, and clearance in the rat. *Adv Funct Mater.* 2006; 16: 1299–305.



150. Sun Y, Liu Q, Peng J, Feng W, Zhang Y, Yang P, et al. Radioisotope post-labeling upconversion nanophosphors for *in vivo* quantitative tracking. *BIOMATERIALS*. 2013; 34: 2289–95.
151. Peng P, Wu N, Ye L, Jiang F, Feng W, Li F, et al. Biodegradable inorganic upconversion nanocrystals for *in vivo* applications. *ACS Nano*. 2020; 14: 16672–80.
152. Wang Y, Feng M, Lin B, Peng X, Wang Z, Lv R. MET-targeted NIR II luminescence diagnosis and up-conversion guided photodynamic therapy for triple-negative breast cancer based on a lanthanide nanoprobe. *Nanoscale*. 2021; 13: 18125–33.
153. Xu J, He F, Cheng Z, Lv R, Dai Y, Gulzar A, et al. Yolk-structured upconversion nanoparticles with biodegradable silica shell for FRET sensing of drug release and imaging-guided chemotherapy. *Chem Mater*. 2017; 29: 7615–28.
154. Service RF. Nanomaterials show signs of toxicity. *Science*. 2003; 300: 243–243.
155. Oliveira H, Bednarkiewicz A, Falk A, Fröhlich E, Lisjak D, Prina-Mello A, et al. Critical considerations on the clinical translation of upconversion nanoparticles (UCNPs): recommendations from the european upconversion network (COST action CM1403). *Adv Healthc Mater*. 2019; 8: 1801233.
156. Zhou J-C, Yang Z-L, Dong W, Tang R-J, Sun L-D, Yan C-H. Bioimaging and toxicity assessments of near-infrared upconversion luminescent NaYF<sub>4</sub>:Yb,Tm nanocrystals. *Biomaterials*. 2011; 32: 9059–67.
157. Lay A, Sheppard OH, Siefe C, McLellan CA, Mehlenbacher RD, Fischer S, et al. Optically robust and biocompatible mechanosensitive upconverting nanoparticles. *ACS Cent Sci*. 2019; 5: 1211–22.
158. Ao Y, Zeng K, Yu B, Miao Y, Hung W, Yu Z, et al. An upconversion nanoparticle enables near infrared-optogenetic manipulation of the *caenorhabditis elegans* motor circuit. *ACS Nano*. 2019; 13: 3373–86.
159. Khan IA, Yu T, Li Y, Hu C, Zhao X, Wei Q, et al. In vivo toxicity of upconversion nanoparticles (NaYF<sub>4</sub>:Yb, Er) in zebrafish during early life stages: developmental toxicity, gut-microbiome disruption, and proinflammatory effects. *Ecotoxicol Environ Saf*. 2024; 284: 116905.
160. Wang K, Ma J, He M, Gao G, Xu H, Sang J, et al. Toxicity assessments of near-infrared upconversion luminescent LaF<sub>3</sub>:Yb,Er in early development of zebrafish embryos. *Theranostics*. 2013; 3: 258–66.
161. Sun Y, Feng W, Yang P, Huang C, Li F. The biosafety of lanthanide upconversion nanomaterials. *Chem Soc Rev*. 2015; 44: 1509–25.
162. Yu J, Yin W, Peng T, Chang Y, Zu Y, Li J, et al. Biodistribution, excretion, and toxicity of

- polyethyleneimine modified NaYF<sub>4</sub>:Yb,Er upconversion nanoparticles in mice via different administration routes. *Nanoscale*. 2017; 9: 4497–507.
163. Feng Y, Chen H, Ma L, Shao B, Zhao S, Wang Z, et al. Surfactant-free aqueous synthesis of novel Ba<sub>2</sub>GdF<sub>7</sub>:Yb<sup>3+</sup>, Er<sup>3+</sup>@PEG upconversion nanoparticles for in vivo trimodality imaging. *ACS Appl Mater Interfaces*. 2017; 9: 15096–102.
  164. Urdzikova LM, Marekova D, Vasylyshyn T, Matous P, Patsula V, Oleksa V, et al. Toxicity of large and small surface-engineered upconverting nanoparticles for In vitro and In vivo bioapplications. *Int J Mol Sci*. 2024; 25: 5294.
  165. An R, Lei P, Zhang P, Xu X, Feng J, Zhang H. Near-infrared optical and X-ray computed tomography dual-modal imaging probe based on novel lanthanide-doped K<sub>0.3</sub>Bi<sub>0.7</sub>F<sub>2.4</sub> upconversion nanoparticles. *NANOSCALE*. 2018; 10: 1394–402.
  166. Liu C, Shao H, Li D, Sui X, Liu N, Rahman SU, et al. Safety and efficacy of citric acid-upconverting nanoparticles for multimodal biological imaging in BALB/c mice. *PHOTODIAGNOSIS Photodyn Ther*. 2021; 36: 102485.
  167. Liu C, Gao Z, Zeng J, Hou Y, Fang F, Li Y, et al. Magnetic/upconversion fluorescent NaGdF<sub>4</sub>:Yb,Er nanoparticle-based dual-modal molecular probes for imaging tiny tumors *in vivo*. *ACS Nano*. 2013; 7: 7227–40.
  168. Yu Z, Xia Y, Xing J, Li Z, Zhen J, Jin Y, et al. Y<sub>1</sub>-receptor-ligand-functionalized ultrasmall upconversion nanoparticles for tumor-targeted trimodality imaging and photodynamic therapy with low toxicity. *NANOSCALE*. 2018; 10: 17038–52.
  169. Rucki M, Kejlova K, Vlkova A, Jirova D, Dvorakova M, Svobodova L, et al. Evaluation of toxicity profiles of rare earth elements salts (lanthanides). *J Rare Earths*. 2021; 39: 225–32.
  170. Gnach A, Lipinski T, Bednarkiewicz A, Rybka J, Capobianco JA. Upconverting nanoparticles: assessing the toxicity. *Chem Soc Rev*. 2015; 44: 1561–84.
  171. Wang W, Yang Y, Wang D, Huang L. Toxic effects of rare earth elements on human health: a review. *Toxics*. 2024; 12: 317.
  172. Wang C, He M, Chen B, Hu B. Study on cytotoxicity, cellular uptake and elimination of rare-earth-doped upconversion nanoparticles in human hepatocellular carcinoma cells. *Ecotoxicol Environ Saf*. 2020; 203: 110951.
  173. Alkahtani M, Alsofyani N, Alfahd A, Almuqhim AA, Almughem FA, Alshehri AA, et al. Engineering red-enhanced and biocompatible upconversion nanoparticles. *Nanomaterials*. 2021; 11: 284.
  174. Zhang J-Q, Zhou W, Zhu S-S, Lin J, Wei P-F, Li F-F, et al. Persistency of enlarged autolysosomes underscores nanoparticle-induced autophagy in hepatocytes. *Small*. 2017; 13: 1602876.

175. Abraham JL, Thakral C, Skov L, Rossen K, Marckmann P. Dermal inorganic gadolinium concentrations: evidence for *in vivo* transmetallation and long-term persistence in nephrogenic systemic fibrosis: dermal gadolinium in nephrogenic systemic fibrosis. *Br J Dermatol*. 2007; 158: 273–80.
176. Chen J-P, Shi S-S, Liu G-F, Chen Y, Zheng S-S, Wang X-B, et al. Potential clinical risk of inflammation and toxicity from rare-earth nanoparticles in mice. *Chin Med J (Engl)*. 2018; 131: 1591–7.
177. Semashko VV, Pudovkin MS, Cefalas A-C, Zelenikhin PV, Gavril VE, Nizamutdinov AS, et al. Tiny rare-earth fluoride nanoparticles activate tumour cell growth via electrical polar interactions. *Nanoscale Res Lett*. 2018; 13: 370.
178. Guller AE, Nadort A, Generalova AN, Khaydukov EV, Nechaev AV, Kornienko IA, et al. Rational surface design of upconversion nanoparticles with polyethylenimine coating for biomedical applications: better safe than brighter? *ACS Biomater Sci Eng*. 2018; 4: 3143–53.
179. Samhadaneh DM, Mandl GA, Han Z, Mahjoob M, Weber SC, Tuznik M, et al. Evaluation of lanthanide-doped upconverting nanoparticles for *in vitro* and *in vivo* applications. *ACS Appl Bio Mater*. 2020; 3: 4358–69.
180. Vedunova MV, Mishchenko TA, Mitroshina EV, Ponomareva NV, Yudintsev AV, Generalova AN, et al. Cytotoxic effects of upconversion nanoparticles in primary hippocampal cultures. *RSC Adv*. 2016; 6: 33656–65.
181. Ylitalo R, Lehtinen S, Wuolijoki E, Ylitalo P, Lehtimäki T. Cholesterol-lowering properties and safety of chitosan. *Arzneim Forsch*. 2011; 52: 1–7.
182. Fubini B, Hubbard A. Reactive oxygen species (ROS) and reactive nitrogen species (RNS) generation by silica in inflammation and fibrosis. *Free Radic Biol Med*. 2003; 34: 1507–16.
183. Warheit DB. Nanoparticles. *Mater Today*. 2004; 7: 32–5.
184. Webster R, Didier E, Harris P, Siegel N, Stadler J, Tilbury L, et al. PEGylated proteins: evaluation of their safety in the absence of definitive metabolism studies. *Drug Metab Dispos Biol Fate Chem*. 2007; 35: 9–16.
185. Lammers T. Nanomedicine tumor targeting. *Adv Mater*. 2024; 36: 2312169.
186. Matsumura Y, Maeda H. A new concept for macromolecular therapeutics in cancer chemotherapy: mechanism of tumoritropic accumulation of proteins and the antitumor agent smancs. *Cancer Res*. 1986; 46: 6387–92.
187. Kim J, Cho H, Lim D-K, Joo MK, Kim K. Perspectives for improving the tumor targeting of nanomedicine via the EPR effect in clinical tumors. *Int J Mol Sci*. 2023; 24: 10082.

188. Oerlemans C, Bult W, Bos M, Storm G, Nijsen JFW, Hennink WE. Polymeric micelles in anticancer therapy: targeting, imaging and triggered release. *Pharm Res.* 2010; 27: 2569–89.
189. Maeda H, Bharate GY, Daruwalla J. Polymeric drugs for efficient tumor-targeted drug delivery based on EPR-effect. *Eur J Pharm Biopharm Off J Arbeitsgemeinschaft Pharm Verfahrenstechnik EV.* 2009; 71: 409–19.
190. Wilhelm S, Tavares AJ, Dai Q, Ohta S, Audet J, Dvorak HF, et al. Analysis of nanoparticle delivery to tumours. *Nat Rev Mater.* 2016; 1: 16014.
191. Subhan MA, Yalamarty SSK, Filipczak N, Parveen F, Torchilin VP. Recent advances in tumor targeting via EPR effect for cancer treatment. *J Pers Med.* 2021; 11: 571.
192. Veselov VV, Nosyrev AE, Jicsinszky L, Alyautdin RN, Cravotto G. Targeted delivery methods for anticancer drugs. *Cancers.* 2022; 14: 622.
193. Ojha T, Pathak V, Shi Y, Hennink WE, Moonen CTW, Storm G, et al. Pharmacological and physical vessel modulation strategies to improve EPR-mediated drug targeting to tumors. *Adv Drug Deliv Rev.* 2017; 119: 44–60.
194. Nagamitsu A, Greish K, Maeda H. Elevating blood pressure as a strategy to increase tumor-targeted delivery of macromolecular drug SMANCS: cases of advanced solid tumors. *Jpn J Clin Oncol.* 2009; 39: 756–66.
195. Seki T, Carroll F, Illingworth S, Green N, Cawood R, Bachtarzi H, et al. Tumour necrosis factor- $\alpha$  increases extravasation of virus particles into tumour tissue by activating the rho a/rho kinase pathway. *J Control Release Off J Control Release Soc.* 2011; 156: 381–9.
196. Islam W, Fang J, Imamura T, Etrych T, Subr V, Ulbrich K, et al. Augmentation of the enhanced permeability and retention effect with nitric oxide-generating agents improves the therapeutic effects of nanomedicines. *Mol Cancer Ther.* 2018; 17: 2643–53.
197. Diop-Frimpong B, Chauhan VP, Krane S, Boucher Y, Jain RK. Losartan inhibits collagen I synthesis and improves the distribution and efficacy of nanotherapeutics in tumors. *Proc Natl Acad Sci U S A.* 2011; 108: 2909–14.
198. Zhao Y, Cao J, Melamed A, Worley M, Gockley A, Jones D, et al. Losartan treatment enhances chemotherapy efficacy and reduces ascites in ovarian cancer models by normalizing the tumor stroma. *Proc Natl Acad Sci U S A.* 2019; 116: 2210–9.
199. Prieložná J, Mikušová V, Mikuš P. Advances in the delivery of anticancer drugs by nanoparticles and chitosan-based nanoparticles. *Int J Pharm X.* 2024; 8: 100281.
200. Leserman LD, Barbet J, Kourilsky F, Weinstein JN. Targeting to cells of fluorescent liposomes covalently coupled with monoclonal antibody or protein a. *Nature.* 1980; 288: 602–4.

201. Zhang C, Zhang Y, Liang M, Shi X, Jun Y, Fan L, et al. Near-infrared upconversion multimodal nanoparticles for targeted radionuclide therapy of breast cancer lymphatic metastases. *Front Immunol.* 2022; 13: 1063678.
202. Panikar SS, Ramírez-García G, Banu N, Vallejo-Cardona AA, Lugo-Fabres P, Camacho-Villegas TA, et al. Ligand-targeted theranostic liposomes combining methylene blue attached upconversion nanoparticles for NIR activated bioimaging and photodynamic therapy against HER-2 positive breast cancer. *J Lumin.* 2021; 237: 118143.
203. Sitia L, Sevieri M, Signati L, Bonizzi A, Chesi A, Mainini F, et al. HER-2-targeted nanoparticles for breast cancer diagnosis and treatment. *Cancers.* 2022; 14: 2424.
204. Houdaihed L, Evans JC, Allen C. Dual-targeted delivery of nanoparticles encapsulating paclitaxel and everolimus: a novel strategy to overcome breast cancer receptor heterogeneity. *Pharm Res.* 2020; 37: 39.
205. Holliger P, Hudson PJ. Engineered antibody fragments and the rise of single domains. *Nat Biotechnol.* 2005; 23: 1126–36.
206. Grebenik EA, Nadort A, Generalova AN, Nechaev AV, Sreenivasan VKA, Khaydukov EV, et al. Feasibility study of the optical imaging of a breast cancer lesion labeled with upconversion nanoparticle biocomplexes. *J Biomed Opt.* 2013; 18: 76004.
207. Guryev EL, Volodina NO, Shilyagina NY, Gudkov SV, Balalaeva IV, Volovetskiy AB, et al. Radioactive (<sup>90</sup>Y) upconversion nanoparticles conjugated with recombinant targeted toxin for synergistic nanotheranostics of cancer. *Proc Natl Acad Sci U S A.* 2018; 115: 9690–5.
208. Li M, Fang H, Liu Q, Gai Y, Yuan L, Wang S, et al. Red blood cell membrane-coated upconversion nanoparticles for pretargeted multimodality imaging of triple-negative breast cancer. *Biomater Sci.* 2020; 8: 1802–14.
209. Jia X, Liu D, Yu C, Niu N, Li D, Wang J, et al. Tumor microenvironment stimuli-responsive single-NIR-laser activated synergistic phototherapy for hypoxic cancer by perylene functionalized dual-targeted upconversion nanoparticles. *Adv Sci.* 2022; 9: 2203292.
210. Ovais M, Mukherjee S, Pramanik A, Das D, Mukherjee A, Raza A, et al. Designing stimuli-responsive upconversion nanoparticles that exploit the tumor microenvironment. *Adv Mater.* 2020; 32: 2000055.
211. Giaquinto AN, Sung H, Miller KD, Kramer JL, Newman LA, Minihan A, et al. Breast cancer statistics, 2022. *CA Cancer J Clin.* 2022; 72: 524–41.
212. Weissleder R, Mahmood U. Molecular imaging. *Radiology.* 2001; 219: 316–33.
213. Chatterjee DK, Rufaihah AJ, Zhang Y. Upconversion fluorescence imaging of cells and small animals using lanthanide doped nanocrystals. *Biomaterials.* 2008; 29: 937–43.

214. Schalper KA, Kumar S, Hui P, Rimm DL, Gershkovich P. A retrospective population-based comparison of HER2 immunohistochemistry and fluorescence In situ hybridization in breast carcinomas: impact of 2007 american society of clinical oncology/ college of american pathologists criteria. *Arch Pathol Lab Med*. 2014; 138: 213–9.
215. Waks AG, Winer EP. Breast cancer treatment: a review. *JAMA*. 2019; 321: 288.
216. Ramírez-García G, Panikar SS, López-Luke T, Piazza V, Honorato-Colin MA, Camacho-Villegas T, et al. An immunoconjugated up-conversion nanocomplex for selective imaging and photodynamic therapy against HER2-positive breast cancer. *Nanoscale*. 2018; 10: 10154–65.
217. Lu Y, Low PS. Immunotherapy of folate receptor-expressing tumors: review of recent advances and future prospects. *J Controlled Release*. 2003; 91: 17–29.
218. Norton N, Youssef B, Hillman DW, Nassar A, Geiger XJ, Necela BM, et al. Folate receptor alpha expression associates with improved disease-free survival in triple negative breast cancer patients. *Npj Breast Cancer*. 2020; 6: 1–9.
219. Chávez-García D, Juárez-Moreno K, Campos CH, Tejeda EM, Alderete JB, Hirata GA. Cytotoxicity, genotoxicity and uptake detection of folic acid-functionalized green upconversion nanoparticles Y<sub>2</sub>O<sub>3</sub>/Er<sup>3+</sup>, Yb<sup>3+</sup> as biolabels for cancer cells. *J Mater Sci*. 2018; 53: 6665–80.
220. Chávez-García D, Juárez-Moreno K, Campos CH, Alderete JB, Hirata GA. Upconversion rare earth nanoparticles functionalized with folic acid for bioimaging of MCF-7 breast cancer cells. *J Mater Res*. 2018; 33: 191–200.
221. Zhao L, Choi J, Lu Y, Kim SY. NIR photoregulated theranostic system based on hexagonal-phase upconverting nanoparticles for tumor-targeted photodynamic therapy and fluorescence imaging. *Nanomaterials*. 2020; 10: 2332.
222. Chowdhuri AR, Laha D, Chandra S, Karmakar P, Sahu SK. Synthesis of multifunctional upconversion NMOFs for targeted antitumor drug delivery and imaging in triple negative breast cancer cells. *Chem Eng J*. 2017; 319: 200–11.
223. Xiong L, Chen Z, Tian Q, Cao T, Xu C, Li F. High contrast upconversion luminescence targeted imaging in vivo using peptide-labeled nanophosphors. *Anal Chem*. 2009; 81: 8687–94.
224. Lou K-L, Wang P-Y, Yang R-Q, Gao Y-Y, Tian H-N, Dang Y-Y, et al. Fabrication of tumor targeting rare-earth nanocrystals for real-time NIR-IIb fluorescence imaging-guided breast cancer precise surgery. *Nanomedicine Nanotechnol Biol Med*. 2022; 43: 102555.
225. Zheng X-Y, Pellico J, Khrapitchev AA, Sibson NR, Davis JJ. Dy-DOTA integrated mesoporous silica nanoparticles as promising ultrahigh field magnetic resonance imaging contrast agents. *Nanoscale*. 2018; 10: 21041–5.

226. Wei Z, Duan G, Huang B, Qiu S, Zhou D, Zeng J, et al. Rapidly liver-clearable rare-earth core-shell nanoprobe for dual-modal breast cancer imaging in the second near-infrared window. *J Nanobiotechnology*. 2021; 19: 369.
227. Du H, Yu J, Guo D, Yang W, Wang J, Zhang B. Improving the MR imaging sensitivity of upconversion nanoparticles by an internal and external incorporation of the  $Gd^{3+}$  strategy for in vivo tumor-targeted imaging. *Langmuir*. 2016; 32: 1155–65.
228. Zhu X, Zhou J, Chen M, Shi M, Feng W, Li F. Core-shell  $Fe_3O_4@NaLuF_4:Yb,Er/Tm$  nanostructure for MRI, CT and upconversion luminescence tri-modality imaging. *Biomaterials*. 2012; 33: 4618–27.
229. Zhang Q, Wang W, Zhang M, Wu F, Zheng T, Sheng B, et al. A theranostic nanocomposite with integrated black phosphorus nanosheet,  $Fe_3O_4@MnO_2$ -doped upconversion nanoparticles and chlorin for simultaneous multimodal imaging, highly efficient photodynamic and photothermal therapy. *Chem Eng J*. 2020; 391: 123525.
230. Wang X, Kang C, Pan Y, Jiang R. Photothermal effects of  $NaYF_4:Yb,Er@PE_3@Fe_3O_4$  superparamagnetic nanoprobe in the treatment of melanoma. *Int J NANOMEDICINE*. 2019; 14: 4319–31.
231. Xia A, Gao Y, Zhou J, Li C, Yang T, Wu D, et al. Core-shell  $NaYF_4:Yb^{3+},Tm^{3+}@Fe_3O_4$  nanocrystals for dual-modality T2-enhanced magnetic resonance and NIR-to-NIR upconversion luminescent imaging of small-animal lymphatic node. *Biomaterials*. 2011; 32: 7200–8.
232. Wang S, Zhang H, Wang X, Yu J, Zhang Q, Zheng Y, et al. Development and validation of a nomogram for axillary lymph node metastasis risk in breast cancer. *J Cancer*. 2024; 15: 6122–34.
233. Haller C, Hizoh I. The cytotoxicity of iodinated radiocontrast agents on renal cells in vitro. *Invest Radiol*. 2004; 39: 149–54.
234. Devaraj NK, Keliher EJ, Thurber GM, Nahrendorf M, Weissleder R.  $^{18}F$  labeled nanoparticles for *in vivo* PET-CT imaging. *Bioconjug Chem*. 2009; 20: 397–401.
235. Fang H, Li M, Liu Q, Gai Y, Yuan L, Wang S, et al. Ultra-sensitive nanoprobe modified with tumor cell membrane for UCL/MRI/PET multimodality precise imaging of triple-negative breast cancer. *Nano-Micro Lett*. 2020; 12: 62.
236. Qiu S-Q, Zhang G-J, Jansen L, de Vries J, Schröder CP, de Vries EGE, et al. Evolution in sentinel lymph node biopsy in breast cancer. *Crit Rev Oncol Hematol*. 2018; 123: 83–94.
237. Park HS, Nam SH, Kim J, Shin HS, Suh YD, Hong KS. Clear-cut observation of clearance of sustainable upconverting nanoparticles from lymphatic system of small living mice. *Sci Rep*. 2016; 6: 27407.

238. Qiu S, Zeng J, Hou Y, Chen L, Ge J, Wen L, et al. Detection of lymph node metastasis with near-infrared upconversion luminescent nanoprobe. *Nanoscale*. 2018; 10: 21772–81.
239. Zhu Y-Y, Song L, Zhang Y-Q, Liu W-L, Chen W-L, Gao W-L, et al. Development of a rare earth nanoprobe enables In vivo real-time detection of sentinel lymph node metastasis of breast cancer using NIR-IIb imaging. *Cancer Res*. 2023; 83: 3428–41.
240. Fang Y, Li Y, Li Y, He R, Zhang Y, Zhang X, et al. *In situ* protease secretion visualization and metastatic lymph nodes imaging via a cell membrane-anchored upconversion nanoprobe. *Anal Chem*. 2021; 93: 7258–65.
241. Li D, He S, Wu Y, Liu J, Liu Q, Chang B, et al. Excretable lanthanide nanoparticle for biomedical imaging and surgical navigation in the second near-infrared window. *Adv Sci*. 2019; 6: 1902042.
242. Kuningas K, Ukonaho T, Pääkilä H, Rantanen T, Rosenberg J, Lövgren T, et al. Upconversion fluorescence resonance energy transfer in a homogeneous immunoassay for estradiol. *Anal Chem*. 2006; 78: 4690–6.
243. Jin B, Li S, Zhang C, Ma C, Hu J, Wang J, et al. Systematic optimization of UCNPs-LFA for helicobacter pylori nucleic acid detection at point-of-care. *Microchim Acta*. 2024; 191: 650.
244. Kumar M, Salem K, Tevaarwerk AJ, Strigel RM, Fowler AM. Recent advances in imaging steroid hormone receptors in breast cancer. *J Nucl Med Off Publ Soc Nucl Med*. 2020; 61: 172–6.
245. Farka Z, Mickert MJ, Mikušová Z, Hlaváček A, Bouchalová P, Xu W, et al. Surface design of photon-upconversion nanoparticles for high-contrast immunocytochemistry. *Nanoscale*. 2020; 12: 8303–13.
246. Hlaváček A, Farka Z, Mickert MJ, Kostiv U, Brandmeier JC, Horák D, et al. Bioconjugates of photon-upconversion nanoparticles for cancer biomarker detection and imaging. *Nat Protoc*. 2022; 17: 1028–72.
247. Zhou L, Wang R, Yao C, Li X, Wang C, Zhang X, et al. Single-band upconversion nanoprobe for multiplexed simultaneous in situ molecular mapping of cancer biomarkers. *Nat Commun*. 2015; 6: 6938.
248. Lan J, Li L, Liu Y, Yan L, Li C, Chen J, et al. Upconversion luminescence assay for the detection of the vascular endothelial growth factor, a biomarker for breast cancer. *Microchim ACTA*. 2016; 183: 3201–8.
249. Yuan Y, Yu H, Yin Y. A highly sensitive aptasensor for vascular endothelial growth factor based on fluorescence resonance energy transfer from upconversion nanoparticles to MoS<sub>2</sub> nanosheets. *Anal Methods*. 2020; 12: 4466–72.



250. Hayes DF, Zurawski VR, Kufe DW. Comparison of circulating CA15-3 and carcinoembryonic antigen levels in patients with breast cancer. *J Clin Oncol.* 1986; 4: 1542–50.
251. Uehara M, Kinoshita T, Hojo T, Akashi-Tanaka S, Iwamoto E, Fukutomi T. Long-term prognostic study of carcinoembryonic antigen (CEA) and carbohydrate antigen 15-3 (CA 15-3) in breast cancer. *Int J Clin Oncol.* 2008; 13: 447–51.
252. Di Gioia D, Dresse M, Mayr D, Nagel D, Heinemann V, Stieber P. Serum HER2 in combination with CA 15-3 as a parameter for prognosis in patients with early breast cancer. *Clin Chim Acta Int J Clin Chem.* 2015; 440: 16–22.
253. Liang T, Ma X, Zhang X, Ye M, Wang Y, Li C. A homogeneous biosensor for carbohydrate antigen 153 detection in human serum based on upconversion fluorescence resonance energy transfer. *Talanta Open.* 2022; 6: 100154.
254. Li J, Liu L, Feng Z, Wang X, Huang Y, Dai H, et al. Tumor markers CA15-3, CA125, CEA and breast cancer survival by molecular subtype: a cohort study. *Breast Cancer Tokyo Jpn.* 2020; 27: 621–30.
255. Liu J, Xu S, Sun L, Hu S, Sun J, Liu M, et al. Up-conversion fluorescence biosensor for sensitive detection of CA-125 tumor markers. *J RARE EARTHS.* 2019; 37: 943–8.
256. Zhang X, Wang Y, Deng H, Xiong X, Zhang H, Liang T, et al. An aptamer biosensor for CA125 quantification in human serum based on upconversion luminescence resonance energy transfer. *Microchem J.* 2021; 161: 105761.
257. Ekman M, Salminen T, Raiko K, Soukka T, Gidwani K, Martiskainen I. Spectrally separated dual-label upconversion luminescence lateral flow assay for cancer-specific STn-glycosylation in CA125 and CA15-3. *Anal Bioanal Chem.* 2024; 416: 3251–60.
258. Wu S, He Z, Zhou J, Sun J, Li F, Lin Q, et al. Serum levels of CEA and CA15-3 in different molecular subtypes and prognostic value in chinese breast cancer. *Breast Edinb Scotl.* 2014; 23: 88–93.
259. He M, Shang N, Shen L, Liu Z. A paper-supported sandwich immunosensor based on upconversion luminescence resonance energy transfer for the visual and quantitative determination of a cancer biomarker in human serum. *Analyst.* 2020; 145: 4181–7.
260. Han Y, Shen L, Li Z, Liu Z. A strategy to facilitate the assembly of DNA and upconversion nanoparticles for biosensor construction. *Anal Methods.* 2018; 10: 3933–8.
261. Yuan Y, Di Y, Chen Y, Yu H, Li R, Yu S, et al. A fluorescent aptasensor for highly sensitive and selective detection of carcinoembryonic antigen based on upconversion nanoparticles and WS2 nanosheets. *Anal Methods.* 2024; 16: 1225–31.
262. Yu D, Zha Z, Tang S, Qiu Y, Liu D. Modification-free fluorescent biosensor for CEA based

- on polydopamine-coated upconversion nanoparticles. *J Fluoresc.* 2022; 32: 1289–97.
263. Qiu Z, Shu J, Tang D. Near-infrared-to-ultraviolet light-mediated photoelectrochemical aptasensing platform for cancer biomarker based on core shell NaYF<sub>4</sub>:Yb,Tm@TiO<sub>2</sub> upconversion microrods. *Anal Chem.* 2018; 90: 1021–8.
  264. Shao K, Xie W, Ling Q, Wang T, Zhang H, Teng Y, et al. Dumbbell-like upconversion nanoparticles synthesized by controlled epitaxial growth for light-heat-color tri-modal sensing of carcinoembryonic antigen. *Biosens Bioelectron.* 2023; 228: 115186.
  265. Xu Z, Wang C, Ma R, Sha Z, Liang F, Sun S. Aptamer-based biosensing through the mapping of encoding upconversion nanoparticles for sensitive CEA detection. *Analyst.* 2022; 147: 3350–9.
  266. Gao R, Hao C, Xu L, Xu C, Kuang H. Spiny nanorod and upconversion nanoparticle satellite assemblies for ultrasensitive detection of messenger RNA in living cells. *Anal Chem.* 2018; 90: 5414–21.
  267. Ding Q, Zhan Q, Zhou X, Zhang T, Xing D. Theranostic upconversion nanobeacons for tumor mRNA ratiometric fluorescence detection and imaging-monitored drug delivery. *Small Weinh Bergstr Ger.* 2016; 12: 5944–53.
  268. Li S, Xu L, Ma W, Wu X, Sun M, Kuang H, et al. Dual-mode ultrasensitive quantification of MicroRNA in living cells by chiropalmonic nanopyramids self-assembled from gold and upconversion nanoparticles. *J Am Chem Soc.* 2016; 138: 306–12.
  269. Zhang K, Song S, Huang S, Yang L, Min Q, Wu X, et al. Lighting up MicroRNA in living cells by the disassembly of lock-like DNA-programmed UCNPs-AuNPs through the target cycling amplification strategy. *Small Weinh Bergstr Ger.* 2018; 14: e1802292.
  270. Gao L, Medford A, Spring L, Bar Y, Hu B, Jimenez R, et al. Searching for the ‘holy grail’ of breast cancer recurrence risk: a narrative review of the hunt for a better biomarker and the promise of circulating tumor DNA (ctDNA). *Breast Cancer Res Treat.* 2024; 205: 211–26.
  271. Wang J, Hua G, Li L, Li D, Wang F, Wu J, et al. Upconversion nanoparticle and gold nanocage satellite assemblies for sensitive ctDNA detection in serum. *The Analyst.* 2020; 145: 5553–62.
  272. Gong C, Mao X, Wang Z, Luo Z, Liu Z, Ben Y, et al. Near-infrared light regulation of capture and release of ctDNA platforms based on the DNA assembly system. *Front Bioeng Biotechnol.* 2022; 10: 891727.
  273. Ackroyd R, Kelty C, Brown N, Reed M. The history of photodetection and photodynamic therapy. *Photochem Photobiol.* 2001; 74: 656–69.
  274. Maiman TH. Stimulated optical radiation in ruby. *Nature.* 1960; 187: 493–4.

275. Li X, Lovell JF, Yoon J, Chen X. Clinical development and potential of photothermal and photodynamic therapies for cancer. *Nat Rev Clin Oncol*. 2020; 17: 657–74.
276. Wang D, Liu B, Quan Z, Li C, Hou Z, Xing B, et al. New advances on the marrying of UCNPs and photothermal agents for imaging-guided diagnosis and the therapy of tumors. *J Mater Chem B*. 2017; 5: 2209–30.
277. Cramer GM, Cengel KA, Busch TM. Forging forward in photodynamic therapy. *Cancer Res*. 2022; 82: 534–6.
278. Cengel KA, Simone CB, Glatstein E. PDT: what's past is prologue. *Cancer Res*. 2016; 76: 2497–9.
279. Sai DL, Lee J, Nguyen DL, Kim Y-P. Tailoring photosensitive ROS for advanced photodynamic therapy. *Exp Mol Med*. 2021; 53: 495–504.
280. Khaydukov EV, Mironova KE, Semchishen VA, Generalova AN, Nechaev AV, Khochenkov DA, et al. Riboflavin photoactivation by upconversion nanoparticles for cancer treatment. *Sci Rep*. 2016; 6: 35103.
281. Kamarudin JBM, Sun B, Foo ASC, Lim X-Y, Judd H, Tan X, et al. SIRIUS, ultra-scintillating upconversion breast implant for remote orthotopic photodynamic therapy. *ACS Nano*. 2023; 17: 11593–606.
282. Liang L, Lu Y, Zhang R, Care A, Ortega TA, Deyev SM, et al. Deep-penetrating photodynamic therapy with KillerRed mediated by upconversion nanoparticles. *Acta Biomater*. 2017; 51: 461–70.
283. Zhang D, Wen L, Huang R, Wang H, Hu X, Xing D. Mitochondrial specific photodynamic therapy by rare-earth nanoparticles mediated near-infrared graphene quantum dots. *BIOMATERIALS*. 2018; 153: 14–26.
284. Liu C, Liu B, Zhao J, Di Z, Chen D, Gu Z, et al. Nd<sup>3+</sup>-sensitized upconversion metal–organic frameworks for mitochondria-targeted amplified photodynamic therapy. *Angew Chem Int Ed*. 2020; 59: 2634–8.
285. Wang C, Cheng L, Liu Y, Wang X, Ma X, Deng Z, et al. Imaging-guided pH-sensitive photodynamic therapy using charge reversible upconversion nanoparticles under near-infrared light. *Adv Funct Mater*. 2013; 23: 3077–86.
286. Jin G, He R, Liu Q, Lin M, Dong Y, Li K, et al. Near-infrared light-regulated cancer theranostic nanoplatform based on aggregation-induced emission luminogen encapsulated upconversion nanoparticles. *Theranostics*. 2019; 9: 246–64.
287. Ito A, Shinkai M, Honda H, Yoshikawa K, Saga S, Wakabayashi T, et al. Heat shock protein 70 expression induces antitumor immunity during intracellular hyperthermia using magnetite nanoparticles. *Cancer Immunol Immunother*. 2003; 52: 80–8.

288. Fadok VA, Voelker DR, Campbell PA, Cohen JJ, Bratton DL, Henson PM. Exposure of phosphatidylserine on the surface of apoptotic lymphocytes triggers specific recognition and removal by macrophages. *J Immunol Baltim Md 1950*. 1992; 148: 2207–16.
289. Ai Y, Meng Y, Yan B, Zhou Q, Wang X. The biochemical pathways of apoptotic, necroptotic, pyroptotic, and ferroptotic cell death. *Mol Cell*. 2024; 84: 170–9.
290. Song CW, Park H, Griffin RJ. Improvement of tumor oxygenation by mild hyperthermia. *Radiat Res*. 2001; 155: 515–28.
291. Qian LP, Zhou LH, Too H-P, Chow G-M. Gold decorated NaYF<sub>4</sub>:Yb,Er/NaYF<sub>4</sub>/silica (core/shell/shell) upconversion nanoparticles for photothermal destruction of BE(2)-C neuroblastoma cells. *J Nanoparticle Res*. 2011; 13: 499–510.
292. Chen C-W, Lee P-H, Chan Y-C, Hsiao M, Chen C-H, Wu PC, et al. Plasmon-induced hyperthermia: hybrid upconversion NaYF<sub>4</sub>:Yb/Er and gold nanomaterials for oral cancer photothermal therapy. *J Mater Chem B*. 2015; 3: 8293–302.
293. Jiang X, Wang Y, Xu D, Lin B, Yang F, Lv R. Lanthanide-based nanocomposites for photothermal therapy under near-infrared laser: relationship between light and heat, biostability, and reaction temperature. *Langmuir*. 2020; 36: 4033–43.
294. Cheng L, Yang K, Li Y, Zeng X, Shao M, Lee S-T, et al. Multifunctional nanoparticles for upconversion luminescence/MR multimodal imaging and magnetically targeted photothermal therapy. *Biomaterials*. 2012; 33: 2215–22.
295. Ramírez-García G, Honorato-Colin MÁ, De la Rosa E, López-Luke T, Panikar SS, Ibarra-Sánchez J de J, et al. Theranostic nanocomplex of gold-decorated upconversion nanoparticles for optical imaging and temperature-controlled photothermal therapy. *J Photochem Photobiol Chem*. 2019; 384: 112053.
296. Zhu X, Feng W, Chang J, Tan Y-W, Li J, Chen M, et al. Temperature-feedback upconversion nanocomposite for accurate photothermal therapy at facile temperature. *Nat Commun*. 2016; 7: 10437.
297. Chen Q, Wang C, Cheng L, He W, Cheng Z, Liu Z. Protein modified upconversion nanoparticles for imaging-guided combined photothermal and photodynamic therapy. *BIOMATERIALS*. 2014; 35: 2915–23.
298. Yang L, Yu S, Yan Y, Bi S, Zhu J-J. Upconversion nanoparticle@Au core-satellite assemblies for In situ amplified imaging of MicroRNA in living cells and combined cancer phototherapy. *Anal Chem*. 2022; 94: 7075–83.
299. Chu Z, Tian T, Tao Z, Yang J, Chen B, Chen H, et al. Upconversion nanoparticles@AgBiS<sub>2</sub> core-shell nanoparticles with cancer-cell-specific cytotoxicity for combined photothermal and photodynamic therapy of cancers. *Bioact Mater*. 2022; 17: 71–80.

300. Shao Z, Pang D, Yang H, Li W, Wang S, Cui S, et al. Efficacy, safety, and tolerability of pertuzumab, trastuzumab, and docetaxel for patients with early or locally advanced ERBB2-positive breast cancer in Asia: the PEONY phase 3 randomized clinical trial. *JAMA Oncol.* 2020; 6: e193692.
301. Yang G, Nowsheen S, Aziz K, Georgakilas AG. Toxicity and adverse effects of tamoxifen and other anti-estrogen drugs. *Pharmacol Ther.* 2013; 139: 392–404.
302. Cullis PR, Felgner PL. The 60-year evolution of lipid nanoparticles for nucleic acid delivery. *Nat Rev Drug Discov.* 2024; 23: 709–22.
303. Liu J-N, Bu W-B, Shi J-L. Silica coated upconversion nanoparticles: a versatile platform for the development of efficient theranostics. *Acc Chem Res.* 2015; 48: 1797–805.
304. Wang C, Cheng L, Liu Z. Drug delivery with upconversion nanoparticles for multi-functional targeted cancer cell imaging and therapy. *Biomaterials.* 2011; 32: 1110–20.
305. Zhao J, Yang H, Li J, Wang Y, Wang X. Fabrication of pH-responsive PLGA(UCNPs/DOX) nanocapsules with upconversion luminescence for drug delivery. *Sci Rep.* 2017; 7: 18014.
306. Liu F, He X, Lei Z, Liu L, Zhang J, You H, et al. Facile preparation of doxorubicin-loaded upconversion@polydopamine nanoplatforms for simultaneous In vivo multimodality imaging and chemophotothermal synergistic therapy. *Adv Healthc Mater.* 2015; 4: 559–68.
307. Sun Y, Zhang W, Wang B, Xu X, Chou J, Shimon O, et al. A supramolecular self-assembly strategy for upconversion nanoparticle bioconjugation. *Chem Commun.* 2018; 54: 3851–4.
308. Zhao L, Peng J, Huang Q, Li C, Chen M, Sun Y, et al. Near-infrared photoregulated drug release in living tumor tissue via yolk-shell upconversion nanocages. *Adv Funct Mater.* 2014; 24: 363–71.
309. Dcona MM, Yu Q, Capobianco JA, Hartman MCT. Near infrared light mediated release of doxorubicin using upconversion nanoparticles. *Chem Commun.* 2015; 51: 8477–9.
310. Han R-L, Shi J-H, Liu Z-J, Hou Y-F, Wang Y. Near-infrared light-triggered hydrophobic-to-hydrophilic switch nanovalve for on-demand cancer therapy. *ACS Biomater Sci Eng.* 2018; 4: 3478–86.
311. Xing Q, Li N, Jiao Y, Chen D, Xu J, Xu Q, et al. Near-infrared light-controlled drug release and cancer therapy with polymer-caged upconversion nanoparticles. *RSC Adv.* 2014; 5: 5269–76.
312. Zhang X, Tian G, Yin W, Wang L, Zheng X, Yan L, et al. Controllable generation of nitric oxide by near-infrared-sensitized upconversion nanoparticles for tumor therapy. *Adv Funct Mater.* 2015; 25: 3049–56.

313. Zhang X, Guo Z, Liu J, Tian G, Chen K, Yu S, et al. Near infrared light triggered nitric oxide releasing platform based on upconversion nanoparticles for synergistic therapy of cancer stem-like cells. *Sci Bull.* 2017; 62: 985–96.
314. Jayakumar MKG, Idris NM, Zhang Y. Remote activation of biomolecules in deep tissues using near-infrared-to-UV upconversion nanotransducers. *Proc Natl Acad Sci U S A.* 2012; 109: 8483–8.
315. Yang Y, Liu F, Liu X, Xing B. NIR light controlled photorelease of siRNA and its targeted intracellular delivery based on upconversion nanoparticles. *Nanoscale.* 2013; 5: 231–8.
316. Xiang M, Jiang Y, Zhou J, Bao G, Luo X, Zhang L, et al. NIR light-controlled DNA nanodevice for amplified mRNA imaging and precise gene therapy. *Nano Today.* 2024; 54: 102110.
317. Stubbs M, McSheehy PMJ, Griffiths JR, Bashford CL. Causes and consequences of tumour acidity and implications for treatment. *Mol Med Today.* 2000; 6: 15–9.
318. Zou J, Zhang F, Zhang S, Pollack SF, Elsbahy M, Fan J, et al. Poly(ethylene oxide)-block-polyphosphoester-graft-paclitaxel conjugates with acid-labile linkages as a pH-sensitive and functional nanoscopic platform for paclitaxel delivery. *Adv Healthc Mater.* 2014; 3: 441–8.
319. Wojtkowiak JW, Verduzco D, Schramm KJ, Gillies RJ. Drug resistance and cellular adaptation to tumor acidic pH microenvironment. *Mol Pharm.* 2011; 8: 2032–8.
320. Qiao H, Cui Z, Yang S, Ji D, Wang Y, Yang Y, et al. Targeting osteocytes to attenuate early breast cancer bone metastasis by theranostic upconversion nanoparticles with responsive plumbagin release. *ACS Nano.* 2017; 11: 7259–73.
321. Hu F, Liu B, Chu H, Liu C, Li Z, Chen D, et al. Real-time monitoring of pH-responsive drug release using a metal-phenolic network-functionalized upconversion nanoconstruct. *Nanoscale.* 2019; 11: 9201–6.
322. Wang X, Yang Y, Liu C, Guo H, Chen Z, Xia J, et al. Photo- and pH-responsive drug delivery nanocomposite based on *o*-nitrobenzyl functionalized upconversion nanoparticles. *POLYMER.* 2021; 229: 123961.
323. Chen M, Yang J, Zhou L, Hu X, Wang C, Chai K, et al. Dual-responsive and ROS-augmented nanoplatform for chemo/photodynamic/chemodynamic combination therapy of triple negative breast cancer. *ACS Appl Mater Interfaces.* 2022; 14: 57–68.
324. Thambi T, Park JH, Lee DS. Stimuli-responsive polymersomes for cancer therapy. *Biomater Sci.* 2016; 4: 55–69.
325. Choi KY, Saravanakumar G, Park JH, Park K. Hyaluronic acid-based nanocarriers for intracellular targeting: interfacial interactions with proteins in cancer. *Colloids Surf B*

Biointerfaces. 2012; 99: 82–94.

326. Near-infrared light-activated photochemical internalization of reduction-responsive polyprodrug vesicles for synergistic photodynamic therapy and chemotherapy. *Biomacromolecules*. 2017; 18: 2571–82.
327. Su X, Zhao F, Wang Y, Yan X, Jia S, Du B. CuS as a gatekeeper of mesoporous upconversion nanoparticles-based drug controlled release system for tumor-targeted multimodal imaging and synergetic chemo-thermotherapy. *Nanomedicine Nanotechnol Biol Med*. 2017; 13: 1761–72.
328. Xu J, Han W, Cheng Z, Yang P, Bi H, Yang D, et al. Bioresponsive and near infrared photon co-enhanced cancer theranostic based on upconversion nanocapsules. *Chem Sci*. 2018; 9: 3233–47.
329. Lv R, Yang P, He F, Gai S, Yang G, Dai Y, et al. An imaging-guided platform for synergistic photodynamic/photothermal/chemo-therapy with pH/temperature-responsive drug release. *Biomaterials*. 2015; 63: 115–27.
330. Zhang X, Yang P, Dai Y, Ma P, Li X, Cheng Z, et al. Multifunctional up-converting nanocomposites with smart polymer brushes gated mesopores for cell imaging and thermo/pH dual-responsive drug controlled release. *Adv Funct Mater*. 2013; 23: 4067–78.
331. Zhang T, Huang S, Lin H, An N, Tong R, Chen Y, et al. Enzyme and pH-responsive nanovehicles for intracellular drug release and photodynamic therapy. *New J Chem*. 2017; 41: 2468–78.
332. Li Y, Zhang H, Merkher Y, Chen L, Liu N, Leonov S, et al. Recent advances in therapeutic strategies for triple-negative breast cancer. *J Hematol Oncol*. 2022; 15: 121.
333. Zhang Y, Zhang Z. The history and advances in cancer immunotherapy: understanding the characteristics of tumor-infiltrating immune cells and their therapeutic implications. *Cell Mol Immunol*. 2020; 17: 807–21.
334. Huang L, Rong Y, Tang X, Yi K, Qi P, Hou J, et al. Engineered exosomes as an in situ DC-primed vaccine to boost antitumor immunity in breast cancer. *Mol Cancer*. 2022; 21: 45.
335. Xiang J, Xu L, Gong H, Zhu W, Wang C, Xu J, et al. Antigen-loaded upconversion nanoparticles for dendritic cell stimulation, tracking, and vaccination in dendritic cell-based immunotherapy. *ACS Nano*. 2015; 9: 6401–11.
336. Li Z, Lai X, Fu S, Ren L, Cai H, Zhang H, et al. Immunogenic cell death activates the tumor immune microenvironment to boost the immunotherapy efficiency. *Adv Sci Weinh Baden-Wurt Ger*. 2022; 9: e2201734.

337. Ding B, Shao S, Yu C, Teng B, Wang M, Cheng Z, et al. Large-pore mesoporous-silica-coated upconversion nanoparticles as multifunctional immunoadjuvants with ultrahigh photosensitizer and antigen loading efficiency for improved cancer photodynamic immunotherapy. *Adv Mater.* 2018; 30: 1802479.
338. Jin F, Qi J, Zhu M, Liu D, You Y, Shu G, et al. NIR-triggered sequentially responsive nanocarriers amplified cascade synergistic effect of chemo-photodynamic therapy with inspired antitumor immunity. *ACS Appl Mater Interfaces.* 2020; 12: 32372–87.
339. Ding B, Sheng J, Zheng P, Li C, Li D, Cheng Z, et al. Biodegradable upconversion nanoparticles induce pyroptosis for cancer immunotherapy. *Nano Lett.* 2021; 21: 8281–9.
340. Yan S, Zeng X, Tang Y, Liu B-F, Wang Y, Liu X. Activating antitumor immunity and antimetastatic effect through polydopamine-encapsulated core-shell upconversion nanoparticles. *Adv Mater.* 2019; 31: 1905825.
341. Di Z, Liu B, Zhao J, Gu Z, Zhao Y, Li L. An orthogonally regulatable DNA nanodevice for spatiotemporally controlled biorecognition and tumor treatment. *Sci Adv.* 2020; 6: eaba9381.
342. Lin B, Liu J, Wang Y, Yang F, Huang L, Lv R. Enhanced upconversion luminescence-guided synergistic antitumor therapy based on photodynamic therapy and immune checkpoint blockade. *Chem Mater.* 637231104000000000; 32: 4627–40.
343. Jin F, Qi J, Liu D, You Y, Shu G, Du Y, et al. Cancer-cell-biomimetic upconversion nanoparticles combining chemo-photodynamic therapy and CD73 blockade for metastatic triple-negative breast cancer. *J Controlled Release.* 2021; 337: 90–104.
344. Chu H, Zhao J, Mi Y, Di Z, Li L. NIR-light-mediated spatially selective triggering of anti-tumor immunity via upconversion nanoparticle-based immunodevices. *Nat Commun.* 2019; 10: 2839.
345. Wang M, Song J, Zhou F, Hoover AR, Murray C, Zhou B, et al. NIR-triggered phototherapy and immunotherapy via an antigen-capturing nanoplatfrom for metastatic cancer treatment. *Adv Sci.* 2019; 6: 1802157.
346. Xu J, Xu L, Wang C, Yang R, Zhuang Q, Han X, et al. Near-infrared-triggered photodynamic therapy with multitasking upconversion nanoparticles in combination with checkpoint blockade for immunotherapy of colorectal cancer. *ACS NANO.* 2017; 11: 4463–74.
347. Wang M, Chang M, Li C, Chen Q, Hou Z, Xing B, et al. Tumor-microenvironment-activated reactive oxygen species amplifier for enzymatic cascade cancer starvation/chemodynamic /immunotherapy. *Adv Mater Deerfield Beach Fla.* 2022; 34: e2106010.
348. Xia Y, Fu S, Ma Q, Liu Y, Zhang N. Application of nano-delivery systems in lymph nodes



- for tumor immunotherapy. *Nano Micro Lett.* 2023; 15: 145.
349. Wang J, Shangguan P, Lin M, Fu L, Liu Y, Han L, et al. Dual-site förster resonance energy transfer route of upconversion nanoparticles-based brain-targeted nanotheranostic boosts the near-infrared phototherapy of glioma. *ACS Nano.* 2023; 17: 16840–53.
  350. Dibaba ST, Xiaoqian Ge, Ren W, Sun L. Recent progress of energy transfer and luminescence intensity boosting mechanism in Nd<sup>3+</sup>-sensitized upconversion nanoparticles. *J Rare Earths.* 2019; 37: 791–805.
  351. Lee C, Xu EZ, Liu Y, Teitelboim A, Yao K, Fernandez-Bravo A, et al. Giant nonlinear optical responses from photon-avalanching nanoparticles. *Nature.* 2021; 589: 230–5.
  352. Shah M, Polónia A, Curado M, Vale J, Janowczyk A, Eloy C. Impact of tissue thickness on computational quantification of features in whole slide images for diagnostic pathology. *Endocr Pathol.* 2025; 36: 10.
  353. Dubey N, Chandra S. Upconversion nanoparticles: recent strategies and mechanism based applications. *J Rare Earths.* 2022; 40: 1343–59.
  354. Qiu H, Tan M, Ohulchanskyy TY, Lovell JF, Chen G. Recent progress in upconversion photodynamic therapy. *Nanomaterials.* 2018; 8: 344.
  355. Yang K, Zhao S, Li B, Wang B, Lan M, Song X. Low temperature photothermal therapy: advances and perspectives. *Coord Chem Rev.* 2022; 454: 214330.
  356. Dai Y, Yang D, Ma P, Kang X, Zhang X, Li C, et al. Doxorubicin conjugated NaYF<sub>4</sub>:Yb(3+)/Tm(3+) nanoparticles for therapy and sensing of drug delivery by luminescence resonance energy transfer. *Biomaterials.* 2012; 33: 8704–13.
  357. Zhang Z, Jayakumar MKG, Zheng X, Shikha S, Zhang Y, Bansal A, et al. Upconversion superballs for programmable photoactivation of therapeutics. *Nat Commun.* 2019; 10: 4586.
  358. Sapienza Passos J, Dartora VFMC, Cassone Salata G, Draszesski Malagó I, Lopes LB. Contributions of nanotechnology to the intraductal drug delivery for local treatment and prevention of breast cancer. *Int J Pharm.* 2023; 635: 122681.
  359. Sabin J, Alatorre-Meda M, Miñones J, Domínguez-Arca V, Prieto G. New insights on the mechanism of polyethylenimine transfection and their implications on gene therapy and DNA vaccines. *Colloids Surf B Biointerfaces.* 2022; 210: 112219.
  360. Abolhassani H, Eskandari A, Saremi Poor A, Zarrabi A, Khodadadi B, Karimifard S, et al. Nanobiotechnological approaches for breast cancer management: drug delivery systems and 3D In-vitro models. *Coord Chem Rev.* 2024; 508: 215754.
  361. Bleeker EAJ, De Jong WH, Geertsma RE, Groenewold M, Heugens EHW,

- Koers-Jacquemijns M, et al. Considerations on the EU definition of a nanomaterial: science to support policy making. *Regul Toxicol Pharmacol*. 2013; 65: 119–25.
362. Ali F, Neha K, Parveen S. Current regulatory landscape of nanomaterials and nanomedicines: a global perspective. *J Drug Deliv Sci Technol*. 2023; 80: 104118.
  363. Metselaar JM, Lammers T. Challenges in nanomedicine clinical translation. *Drug Deliv Transl Res*. 2020; 10: 721–5.
  364. Haase M, Schäfer H. Upconverting nanoparticles. *Angew Chem Int Ed*. 2011; 50: 5808–29.
  365. Wang M, Da Y, Tian Y. Fluorescent proteins and genetically encoded biosensors. *Chem Soc Rev*. 2023; 52: 1189–214.
  366. Strack R. Organic dyes for live imaging. *Nat Methods*. 2021; 18: 30–30.
  367. García de Arquer FP, Talapin DV, Klimov VI, Arakawa Y, Bayer M, Sargent EH. Semiconductor quantum dots: technological progress and future challenges. *Science*. 2021; 373: eaaz8541.
  368. Paprocka R, Wiese-Szadkowska M, Janciauskiene S, Kosmalksi T, Kulik M, Helmin-Basa A. Latest developments in metal complexes as anticancer agents. *Coord Chem Rev*. 2022; 452: 214307.
  369. Li S, Li L, Tu H, Zhang H, Silvester DS, Banks CE, et al. The development of carbon dots: from the perspective of materials chemistry. *Mater Today*. 2021; 51: 188–207.
  370. Liu Z, Ju E, Liu J, Du Y, Li Z, Yuan Q, et al. Direct visualization of gastrointestinal tract with lanthanide-doped BaYbF<sub>5</sub> upconversion nanoprobos. *Biomaterials*. 2013; 34: 7444–52.
  371. Zhou J, Yu M, Sun Y, Zhang X, Zhu X, Wu Z, et al. Fluorine-18-labeled Gd<sup>3+</sup>/Yb<sup>3+</sup>/Er<sup>3+</sup> co-doped NaYF<sub>4</sub> nanophosphors for multimodality PET/MR/UCL imaging. *Biomaterials*. 2011; 32: 1148–56.
  372. Liu Z, Dong K, Liu J, Han X, Ren J, Qu X. Anti-biofouling polymer-decorated lutetium-based nanoparticulate contrast agents for In vivo high-resolution trimodal imaging. *Small*. 2014; 10: 2429–38.
  373. Kumar KN, Vijayalakshmi L, Choi J. Investigation of upconversion photoluminescence of Yb<sup>3+</sup>/Er<sup>3+</sup>:NaLaMgWO<sub>6</sub> noncytotoxic double-perovskite nanophosphors. *Inorg Chem*. 2019; 58: 2001–11.
  374. Zhou J, Sun Y, Du X, Xiong L, Hu H, Li F. Dual-modality in vivo imaging using rare-earth nanocrystals with near-infrared to near-infrared (NIR-to-NIR) upconversion luminescence and magnetic resonance properties. *Biomaterials*. 2010; 31: 3287–95.

375. You Y, Cheng S, Zhang L, Zhu Y, Zhang C, Xian Y. Rational modulation of the luminescence of upconversion nanomaterials with phycocyanin for the sensing and imaging of myeloperoxidase during an inflammatory process. *Anal Chem.* 2020; 92: 5091–9.
376. Hu Y, Wu B, Jin Q, Wang X, Li Y, Sun Y, et al. Facile synthesis of 5 nm NaYF<sub>4</sub>:Yb/Er nanoparticles for targeted upconversion imaging of cancer cells. *Talanta.* 2016; 152: 504–12.
377. Hu H, Yu M, Li F, Chen Z, Gao X, Xiong L, et al. Facile epoxidation strategy for producing amphiphilic up-converting rare-earth nanophosphors as biological labels. *Chem Mater.* 2008; 20: 7003–9.
378. Chan Y-C, Chan M-H, Chen C-W, Liu R-S, Hsiao M, Tsai DP. Erratum: near-infrared-activated fluorescence resonance energy transfer-based nanocomposite to sense MMP2-overexpressing oral cancer cells. *ACS Omega.* 2018; 3: 2444.
379. Li L, Hao P, Wei P, Fu L, Ai X, Zhang J, et al. DNA-assisted upconversion nanoplatform for imaging-guided synergistic therapy and laser-switchable drug detoxification. *BIOMATERIALS.* 2017; 136: 43–55.
380. Liu Y, Zhang C, Liu H, Li Y, Xu Z, Li L, et al. Controllable synthesis of up-conversion nanoparticles UCNPs@MIL-PEG for pH-responsive drug delivery and potential up-conversion luminescence/magnetic resonance dual-mode imaging. *J Alloys Compd.* 2018; 749: 939–47.
381. Bungla M, Sharma P, Shanavas A, Ganguli AK. Methylene blue loaded K<sub>0.3</sub>Bi<sub>0.7</sub>F<sub>2.4</sub>:Yb,Er upconversion nanoparticles for near-infrared activated photodynamic therapy. *New J Chem.* 2024; 48: 1800–8.
382. Zhang G, Jiang Y, Zhang W, Kan L, Sun J, Xu L, et al. NIR light activates upconverting nanoparticles/Zn<sub>x</sub>Mn<sub>1-x</sub>S core-shell nanoparticles for improved breast cancer treatment. *Nanoscale.* 2025; 17: 8778–89.
383. Liang Y, An R, Du P, Lei P, Zhang H. NIR-activated upconversion nanoparticles/hydrogen-bonded organic framework nanocomposites for NIR-II imaging-guided cancer therapy. *Nano Today.* 2023; 48: 101751.
384. Kim DW, Wrede P, Rodríguez-Camargo A, Chen Y, Dogan NO, Glück C, et al. Upconversion nanoparticle-covalent organic framework core-shell particles as therapeutic microrobots trackable with optoacoustic imaging. *Adv Mater Deerfield Beach Fla.* 2025; e2418425.
385. Yang Y, Sun Y, Cao T, Peng J, Liu Y, Wu Y, et al. Hydrothermal synthesis of NaLuF<sub>4</sub>:<sup>153</sup>Sm,Yb,Tm nanoparticles and their application in dual-modality upconversion luminescence and SPECT bioimaging. *Biomaterials.* 2013; 34: 774–83.

386. Xing Y, Li L, Ai X, Fu L. Polyaniline-coated upconversion nanoparticles with upconverting luminescent and photothermal conversion properties for photothermal cancer therapy. *Int J Nanomedicine*. 2016; 11: 4327–38.
387. Zeng L, Pan Y, Zou R, Zhang J, Tian Y, Teng Z, et al. 808 nm-excited upconversion nanoprobes with low heating effect for targeted magnetic resonance imaging and high-efficacy photodynamic therapy in HER2-overexpressed breast cancer. *Biomaterials*. 2016; 103: 116–27.
388. Buchner M, García Calavia P, Muhr V, Kröninger A, Bäumner AJ, Hirsch T, et al. Photosensitizer functionalised luminescent upconverting nanoparticles for efficient photodynamic therapy of breast cancer cells. *Photochem Photobiol Sci Off J Eur Photochem Assoc Eur Soc Photobiol*. 2019; 18: 98–109.
389. Ou X, Tan Y, Xie J, Yuan J, Deng X, Shao R, et al. Methylation of GPRC5A promotes liver metastasis and docetaxel resistance through activating mTOR signaling pathway in triple negative breast cancer. *Drug Resist Updat Rev Comment Antimicrob Anticancer Chemother*. 2024; 73: 101063.
390. Chen TW-W, Dai M-S, Tseng L-M, Chen S-C, Chao T-Y, Chao T-C, et al. Whole-brain radiotherapy alone vs preceded by bevacizumab, etoposide, and cisplatin for untreated brain metastases from breast cancer: a randomized clinical trial. *JAMA Oncol*. 2024; 10: 325–34.
391. Zhu Z, Shen H, Xu J, Fang Z, Wo G, Ma Y, et al. GATA3 mediates doxorubicin resistance by inhibiting CYB5R2-catalyzed iron reduction in breast cancer cells. *Drug Resist Updat Rev Comment Antimicrob Anticancer Chemother*. 2023; 69: 100974.
392. Wang H, Guo S, Kim S-J, Shao F, Ho JWK, Wong KU, et al. Cisplatin prevents breast cancer metastasis through blocking early EMT and retards cancer growth together with paclitaxel. *Theranostics*. 2021; 11: 2442–59.
393. Shakeran Z, Varshosaz J, Keyhanfar M, Mohammad-Beigi H, Rahimi K, Sutherland DS. Co-delivery of STAT3 siRNA and methotrexate in breast cancer cells. *Artif Cells Nanomedicine Biotechnol*. 2022; 50: 29–39.
394. Abu Samaan TM, Samec M, Liskova A, Kubatka P, Büsselberg D. Paclitaxel's mechanistic and clinical effects on breast cancer. *Biomolecules*. 2019; 9: 789.
395. Wimmer K, Sachet M, Ramos C, Frantal S, Birnleitner H, Brostjan C, et al. Differential immunomodulatory effects of epirubicin/cyclophosphamide and docetaxel in breast cancer patients. *J Exp Clin Cancer Res CR*. 2023; 42: 300.
396. Pandit B, Royzen M. Recent development of prodrugs of gemcitabine. *Genes*. 2022; 13: 466.
397. Katharotiya K, Shinde G, Katharotiya D, Shelke S, Patel R, Kulkarni D, et al.

- Development, evaluation and biodistribution of stealth liposomes of 5-fluorouracil for effective treatment of breast cancer. *J Liposome Res.* 2022; 32: 146–58.
398. Shepherd JH, Ballman K, Polley M-YC, Campbell JD, Fan C, Selitsky S, et al. CALGB 40603 (alliance): long-term outcomes and genomic correlates of response and survival after neoadjuvant chemotherapy with or without carboplatin and bevacizumab in triple-negative breast cancer. *J Clin Oncol Off J Am Soc Clin Oncol.* 2022; 40: 1323–34.
  399. Shiao SL, Gouin KH, Ing N, Ho A, Basho R, Shah A, et al. Single-cell and spatial profiling identify three response trajectories to pembrolizumab and radiation therapy in triple negative breast cancer. *Cancer Cell.* 2024; 42: 70-84.e8.
  400. Meric-Bernstam F, Makker V, Oaknin A, Oh D-Y, Banerjee S, González-Martín A, et al. Efficacy and safety of trastuzumab deruxtecan in patients with HER2-expressing solid tumors: primary results from the DESTINY-PanTumor02 phase II trial. *J Clin Oncol Off J Am Soc Clin Oncol.* 2024; 42: 47–58.
  401. Chen Y-F, Xu Y-Y, Shao Z-M, Yu K-D. Resistance to antibody-drug conjugates in breast cancer: mechanisms and solutions. *Cancer Commun Lond Engl.* 2023; 43: 297–337.
  402. Wawruszak A, Borkiewicz L, Okon E, Kukula-Koch W, Afshan S, Halasa M. Vorinostat (SAHA) and breast cancer: an overview. *Cancers.* 2021; 13: 4700.
  403. Liang X, Fan J, Zhao Y, Jin R. Synthesis of NaYF<sub>4</sub>:Yb,Er upconversion nanoparticle-based optomagnetic multifunctional composite for drug delivery system. *J Rare Earths.* 2021; 39: 579–86.